PERLE

Powerful Energy Recovery Linac for Experiments

Conceptual Design Report
NOT FOR DISTRIBUTION

CELIA Bordeaux, MIT Boston, CERN, Cockcroft and Astec
Daresbury, TU Darmstadt, U Liverpool, Jefferson Lab
Newport News, BINP Novosibirsk, IPNO and LAL Orsay

March 14th, 2017

List of Authors

G. Arduini[1], B. Auchmann[1], J. Bernauer[10], A. Bogacz[4], S. Bousson[9], C. Bracco[1], O. Brüning[1], R. Calaga[1], K. Cassou[2], V. Chetvertkova[1], E. Cormier[6], E. Daly[4], D. Douglas[4], K. Dupraz[2], B. Goddard[1], J. Henry[4], A. Hutton[4], E. Jensen[1], W. Kaabi[2], M. Klein[5], P. Kostka[5], F. Marhauser[4], A. Martens,[2], A. Milanese[1], B. Militsyn[3], Y. Peinaud[2], D. Pellegrini[1], N. Pietralla[8], Y.A. Pupkov[7], R. A. Rimmer[4], K. Schirm[1], D. Schulte[1], A. Stocchi[2], A. Valloni[1], C. Welsch[5], G. Willering[1], D. Wollmann[1], F. Zimmermann[1], F. Zomer[2]

[1] *CERN, Geneva, Switzerland*

[2] *LAL, CNRS-IN2P3, Université Paris-Sud, Centre Scientifique d'Orsay, France*

[3] *ASTeC, STFC, Daresbury, UK*

[4] *Jefferson Lab, Newport News, VA, USA*

[5] *University of Liverpool, UK*

[6] *CELIA, University of Bordeaux 1, CNRS UMR 5107, Talence, France*

[7] *BINP, Novosibirsk*

[8] *Institut für Kernphysik Technische Universität Darmstadt*

[9] *Institute de Physique Nucleaire Orsay, France*

[10] *Massachusetts Institute of Technology, Cambridge, MA, USA*

Abstract

A conceptual design is presented of a novel ERL facility for the development and application of the energy recovery technique to linear electron accelerators in the multi-turn, large current and large energy regime. The main characteristics of the powerful energy recovery linac experiment facility (PERLE) are derived from the design of the Large Hadron electron Collider, an electron beam upgrade under study for the LHC, for which it would be the key demonstrator. PERLE is thus projected as a facility to investigate efficient, high current (> 10 mA) ERL operation with three re-circulation passages through newly designed SCRF cavities, at 801.58 MHz frequency, and following deceleration over another three re-circulations. In its fully equipped configuration, PERLE provides an electron beam of approximately 1 GeV energy. A physics programme possibly associated with PERLE is sketched, consisting of high precision elastic electron-proton scattering experiments, as well as photo-nuclear reactions of unprecedented intensities with up to 30 MeV photon beam energy as may be obtained using Fabry-Perot cavities. The facility has further applications as a general technology test bed that can investigate and validate novel superconducting magnets (beam induced quench tests) and superconducting RF structures (structure tests with high current beams, beam loading and transients). Besides a chapter on operation aspects, the report contains detailed considerations on the choices for the SCRF structure, optics and lattice design, solutions for arc magnets, source and injector and on further essential components. A suitable configuration derived from the here presented design concept may next be moved forward to a technical design and possibly be built by an international collaboration which is being established.

Contents

CHAPTER 1

Introduction

The development of the Large Hadron Electron Collider (LHeC) [1] opens the horizon for turning the LHC facility, with accurate $pp \rightarrow HX$ and $ep \rightarrow \nu HX$ measurements, into a precision Higgs (H) physics factory. It also represented the world's cleanest, high resolution microscope for exploring the substructure of hadronic matter and parton dynamics at smallest dimensions which also complements the LHC proton-proton (pp) and heavy-ion (AA and pA) physics. The genuine deep inelastic electron-hadron scattering programme of the LHeC [2] is of unprecedented richness. It may lead to beyond the Standard Model through discoveries in ep interactions in the new energy regime and as well through the clarification of proton structure effects in the region of very high mass, corresponding to large Bjorken x, in pp interactions.

As demonstrated in the conceptual design report [1], the LHeC may be realised by the addition of an intense electron beam to the LHC proton (and ion) beams. This novel ep and eA collider may become operational by the end of the next decade, following the now commencing upgrade of the LHC for increased luminosity. It uses two electron linear accelerators arranged in a racetrack configuration, tangential to the LHC tunnel. In three-turn operation mode one is able to generate an electron beam of 60 (50) GeV energy for a circumference of U(LHeC)=U(LHC)/n of approximately 9 (4) km length, for $n = 3$ (5). This configuration would be of immediate use and immense value if the LHC proton energy was doubled, and it has also been considered as the default option for a future electron-hadron operation of the FCC.

The value of the Higgs production cross section at the LHeC of O(100) fb sets a luminos-

26 ity goal of O(10^{34}) cm^{-2}s^{-1} which in the linac-ring configuration of the LHeC, at a total

27 power limit of 100 MW, can only be achieved [3, 4] by application of the energy-recovery

28 technique recently reviewed in [5, 6]. This enables to collect a luminosity of the order

29 of 1 ab^{-1} in synchronous, concurrent *ep* and *pp* operation, thereby exceeding the HERA

30 integrated luminosity by a factor of 10^3. This luminosity is larger than the initial design

31 value by a factor of 10, and the here described LHeC demonstrator PERLE represents the

32 key base for updating the LHeC physics programme and technical design in the not distant

33 future.

34 The demonstration and optimisation of the LHeC principles and parameters require

35 building a high current, multi-turn ERL facility. Its main parameters shall correspond

36 to the LHeC design, and experience with PERLE's operation would be transferable to the

37 LHeC. The LHeC frequency was chosen to be 801.58 MHz, which is compliant with the

38 LHC, keeps beam-beam interactions low and further corresponds well to general optimisa-

39 tion considerations including power, surface resistance and cost. That frequency is also a

40 base frequency for the FCC development such that there is a multiple use envisaged of the

41 here described SCRF developments. The electron beam current should be in the range of

42 $10 - 20$ mA, leading to a 6-fold load in the cavity operation. Three passages through two

43 oppositely positioned linear SCRF accelerator structures of 1 km length each are required

44 for reaching a 60 GeV beam energy for the LHeC as well as for FCC-eh. PERLE will en-

45 able developing main accelerator components, such as the SCRF cavity-cryomodule which

46 comprises four 5-cell cavities with a $15 - 20$ MV/m gradient and operated in CW mode.

47 The facility offers a range of unique technical and physics applications through pow-

48 erful energy recovery linac experiments from which its name, PERLE, is derived. The

49 input electron current of about 15 mA leads to high power tests of the SCRF with currents

50 as large as 100 mA following from three-turn acceleration and deceleration in the energy

51 recovery mode. The choice of electron beam energy depends on its main goals. An LHeC

52 demonstrator, with the here mentioned parameters, may be laid out as a machine with one

53 (or two) cryomodule and deliver a beam of about 220 (440) MeV energy. Physics applica-

54 tions, as are discussed below, may suggest to choose a higher energy. In the here presented

55 design a maximum size racetrack configuration is considered using two opposite linacs,

56 each comprising two cryomodules. This leads to a nearly 1 GeV energy electron beam

57 suitable for *ep* scattering physics, possibly using polarised electrons in weak interaction

58 measurements. Backscattering may generate a photon beam of 30 MeV energy which is

59 of interest to reach beyond the so-called giant dipole resonance. Physics, site, cost and

time schedule considerations make a step-wise development of such a facility attractive and likely.

The design parameters of the facility, its purpose and range of applications distinguish it from a number of further new ERL developments, such as MESA at Mainz [7], BERLinPRO [8], Cβ [9, 10] at Cornell, and the recent ER@CEBAF [11] proposal for a new experiment at the Thomas Jefferson Laboratory. The frequencies of MESA, BERLinPRO and Cβ are 1.3 GHz, while CEBAF operates at 1.5 GHz. MESA is directed primarily to weak interaction measurements. BERLinPRO and Cβ push for very high current developments. The ER@CEBAF intention is for a test at small currents but high energies, of about 6 GeV, in order to study synchrotron radiation effects on the ERL performance [12].

The present paper describes a conceptual design of an LHeC demonstrator and some of its possible applications. PERLE would be of use for the beam based development of SCRF technology, regarding for example the determination of current load limits and the control of higher order modes. It would provide the necessary infrastructure for testing the 3-turn behaviour, stability and reproducibility of the ERL, beam quality measurements in (de)acceleration etc. As is described, the facility would be of use for testing equipment, such as SC magnets and their quench behaviour, under beam conditions. It may also provide a low energy electron test beam for developments of detector technology such as thin Silicon trackers. Various selected and particularly attractive physics applications of PERLE are sketched, comprising, with electron beams, searches for dark photons, weak interaction or proton radius measurements, and, with photon beams, the physics of photo-nuclear reactions, nuclear structure, particle physics metrology and astrophysics, at photon intensities hugely exceeding that of the ELI facility [13] currently under construction in Southern Europe.

This paper is organised as follows: Section 2 describes the multiple purpose of PERLE, including a possible later application as an injector to the LHeC. Section 3 presents the conceptual design of the facility, its system architecture, optics layout etc. Section 4 characterises the main components, the electron source, injector, SC cavity, cryomodule, magnets, transfers, beam dumps and also the generation of a photon beam through backscattered laser light. Section 5 describes aspects of monitoring and operating such a facility, largely based on experience from CEBAF at the Thomas Jefferson Laboratory. Section 6 provides initial considerations of site requirements, followed by a brief summary in Section 7.

Purpose

2.1 SCRF and ERL Tests with PERLE

PERLE is designed to be a multi-purpose and flexible machine that will be able to provide unique test beams in either ERL mode or as a multi-pass re-circulated linac (like CEBAF). It can also be constructed in a phased approach enabling early operation and logical, minimally invasive upgrades. The high intensity, low emittance beams will be invaluable for many hardware and instrumentation test programs as well as offering the potential for low energy physics experiments, dark matter searches, unique light sources etc. Besides these many advantages, PERLE is also a ground breaking accelerator and SRF demonstration and development facility. The principles of multi-pass acceleration and energy recovery using SRF recirculating linacs have already been demonstrated, however this has usually been with SRF cavities and cryomodules developed for, or adapted from, other purposes such as CEBAF or TESLA. Even dedicated ERL demo machines such as the KEK compact ERL and the Cornell ERL injector/ ERL demo project derive their frequency and much of their DNA from the TESLA collaboration technology. JLab's ERL based FEL was also based closely on the CEBAF technology, although a new high current upgrade design was proposed but never funded. PERLE has the opportunity to be a clean-sheet globally optimised design for a new generation of high average power efficient ERL based machines. It will be an ideal facility for testing advanced concepts in cavity design, surface treatments,

10

HOM damping, couplers, tuners, microphonics, etc., as well as emittance preserving optics, multi-pass and high dynamic range diagnostics, instability suppression and feedback, advanced LLRF techniques, etc.

2.1.1 High quality SCRF cavity - status and tests

There has been much progress in SRF cavity design and processing in recent years, stimulated by projects like ILC, XFELs, factory-type colliders, light sources and ADS. This has triggered a diversification of designs, materials, techniques, and applications and no longer does any project have to depend on a set frequency or cell design just because of history or convenience. There now exist in many places around the world the knowledge, experience and tool sets to design, build, test and integrate fully customized and optimized SRF designs for new and exacting requirements. Recent examples include crab cavities for short pulse X-ray sources and colliders, HOM-damped cavities for e^+e^- colliders, high power proton linacs for ADS, etc. The cavity shape optimisation for ERLs is somewhat different than for high-gradient pulsed linacs. The CW operation and potential for high circulating currents require careful attention to heat load (both from RF losses and field emission) and beam break up. In this regard a balance needs to be found between peak electric and peak magnetic fields while maintaining good efficiency and, very importantly, keeping HOMs well away from strong harmonics of the beam current. Because the ERL beam current spectrum depends strongly on the filling pattern and recirculation time, some assumptions must be made about machine operation when examining the HOM spectrum. This is discussed further in section 3.3.2. An important parameter in maintaining good HOM damping is to have strong cell-to-cell coupling. This allows HOMs to propagate easily to the end cells, where the dampers are typically located, and makes the cavity less sensitive to tuning and fabrication errors. In particular it minimises the possibility for HOMs to become trapped in the cavity center or tilted away from HOM couplers. Stronger cell-to-cell coupling implies a larger iris between cells, whereas efficiency is favoured by a smaller iris, so a compromise must be reached. Dangerous HOMs can be detuned if necessary by altering the profile of the cell. The gradient and impact energy of the cell multipacting barrier can be calculated and it is prudent to avoid operating close to this gradient. The impact energy can be minimised by flattening the cell profile in the equator region to make the barrier softer and easier to transition or process away.

2.1.2 Cavity module - principle and tests

The cryostat is the less glamorous cousin of the cavity and is often something of an afterthought, despite being the major share of the cost of the cryomodule. Previous SRF ERLs have used or adapted cryostats from other projects, in some cases converting them from pulsed to CW operation. Some important considerations are pressure code compliance, static heat load, maintainability and operability and cost. The number of magnetic and thermal shields and intercepts, the mechanical support and alignment scheme and whether the linac is continuous (like ILC) or segmented (like CEBAF and SNS) are all variables. For a large machine like LHeC it is worth performing a careful evaluation or even a new, clean sheet design optimised for this purpose, however, for a test machine like PERLE it is advantageous to use an existing well proven design. For this study we have used the SNS style cryostat as it can easily accommodate the 805 MHz 5-cell beta=1 cavities with very minimal modifications, has plenty of heat load capacity, is a segmented design allowing phased construction of the facility and ease of maintenance, and has existing tooling and operational experience. More details are presented in section 3.3

2.1.3 Goals of the ERL design and operation

The purposes of the PERLE ERL demonstrator are to provide flexible test beams for component development, low energy physics experiments, and also to demonstrate and gain operational experience with low-frequency high-current SRF cavities and cryomodules of a type suitable for scale up to a high-energy machine. Since the cavity design, HOM couplers, FPC's etc. will be all new or at least heavily modified, PERLE will serve as a technology test bed that will explore all the parameters needed for a larger machine. There is no other high current ERL test bed in the world that can do this. PERLE will also feature emittance preserving recirculation optics and this will also be an important demonstration that these can be constructed and operated in a flexible user-facility environment. The machine must run with high reliability to provide test beams for experimenters or ultimately provide Compton or FEL radiation to light source users. This demonstration of stability and high reliability will be essential for any future large facility.

2.2 Technical Applications

An intense beam facility will offer new opportunities for auxiliary applications. In view of a possible placement of PERLE in the vicinity of or even at CERN various test options have been studied and results are described subsequently of simulations dedicated to the possibility for beam based investigations of quench levels of superconducting magnets and cables. As is also sketched below, PERLE may offer versatile possibilities for tests of cavities with different frequencies with a suitably chosen injector frequency. With, for example, a 12.146 MHz injector, one may test cavities for frequencies including values of 352, 401, 704, 802 and 1300 MHz, which are of direct interest for CERN's Linac4 and ESS, FCC, ESS, LHeC and FCC, and the ILC, respectively.

2.2.1 Magnets, cables, quench tests

Understanding the quench levels of superconducting cables and magnets is important for an efficient design and the safe and optimal operation of an accelerator using superconducting magnets. Quench levels are used as an input to define requirements for controlling beam losses, therefore influencing e.g. beam cleaning and collimation, beam loss monitor positions and thresholds, interlock delays etc..

The quench level defines the maximum amount of energy that can be deposited locally in a superconducting magnet or cable to cause the phase change from superconducting to normal-conducting state. The quench level is a function of the energy deposition distribution and the duration of the impact, the local temperature before the impact, the cooling capacity, and the local magnetic field.

State of the art electro-thermal solvers, which are used to predict the quench levels of superconducting cables and magnets, are mainly based on lab experiments without beam. To verify their predictions in case of beam impact, quench levels have been extensively studied with beam in the LHC at the end of Run 1 in February 2013. The results for short duration ($< 50 \mu s$) and steady state ($> 5s$) energy deposition are in good agreement with predictions based on electro-thermal simulation codes like QP3 [14] and THEA [15]. For intermediate duration energy depositions the electro-thermal models predict a factor 4 lower quench levels than found during the experiment [16], which still needs to be understood.

Currently the LHC is the only accelerator at CERN, where quench tests with beam can be performed for all relevant time scales. Nevertheless, the LHC is not an adequate test

Figure 2.1: Maximum values of energy deposition (left) and projection of energy deposition (right) for 150 MeV electrons impacting in a solid copper block as calculated by FLUKA [17, 18]. An emittance of $50\,\mu$m and a beta-function at extraction of 5 m was used. The bin size was 1 mm^3.

bed to perform quench tests as: i) only magnets installed in the LHC can be tested, ii) non-trivial beam dynamic studies are required to interpret experimental results and iii) the LHC is a sophisticated accelerator which is ultimately optimized to deliver luminosity to the particle physics experiments. The other facilities at CERN either lack the availability of cryogenics (PS, HiRadMat) or the particle beams (SM18). Furthermore, using the fast extraction from the SPS the HiRadMat facility could only cover the regime of short duration energy deposition. Therefore, a dedicated facility equipped with cryogenics to perform quench tests is required.

Energy deposition studies

Figures 2.1, 2.2 show the energy deposition per primary electron in a solid copper target for 150 MeV and 1 GeV electrons, respectively. For the simulations an emittance of 50 μm and a beta-function at extraction of 5 m was considered. The bin size was 1 mm^3. Combining the peak energy deposition with the quench levels for the LHC main dipoles, as calculated by QP3, the number of primary particles required to reach quench levels for different durations of the energy deposition can be derived. Figure 2.3 summarises the required number of primary particles in case of different particle energies and pulse length durations.

Comparing these numbers to the baseline beam parameters shows that PERLE can pro-
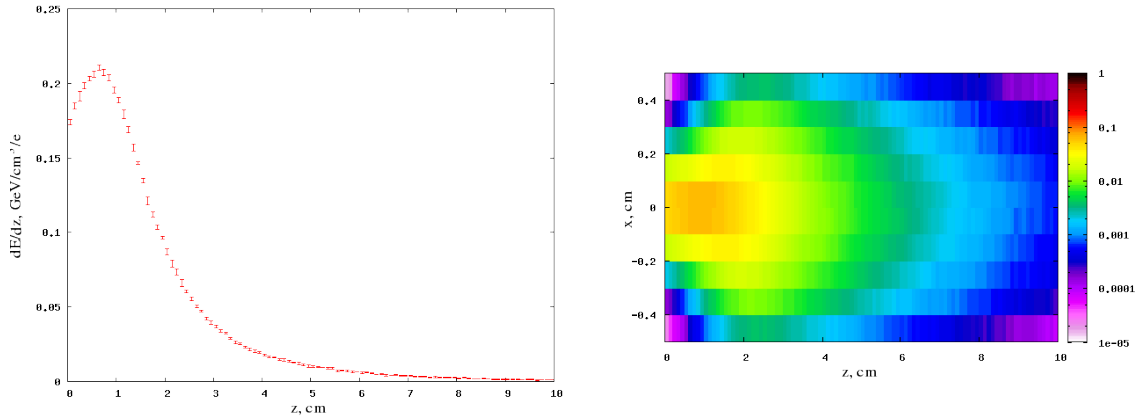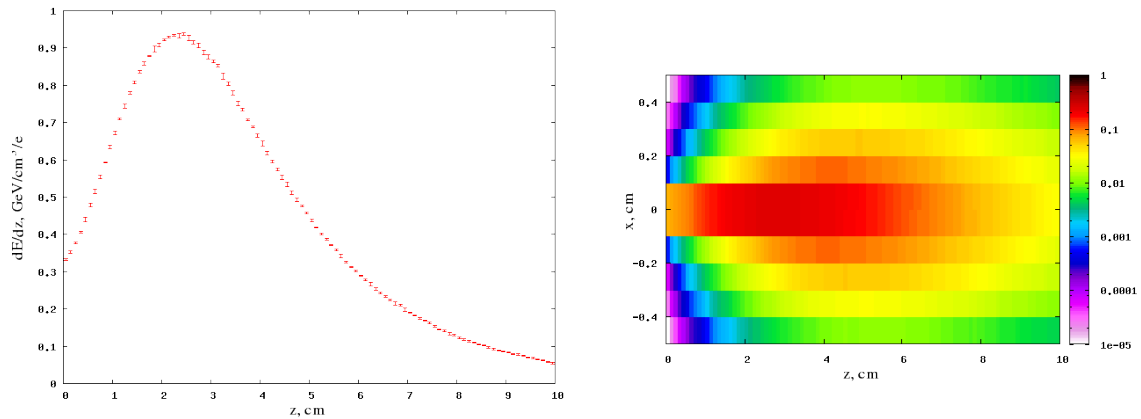
Figure 2.2: Maximum values of energy deposition (left) and projection of energy deposi-
tion (right) for 1 GeV electrons impacting in a solid copper block as calculated
by FLUKA [17, 18]. An emittance of $50\,\mu$m and a beta-function at extraction
of 5 m was used. The bin size was 1 mm^3.
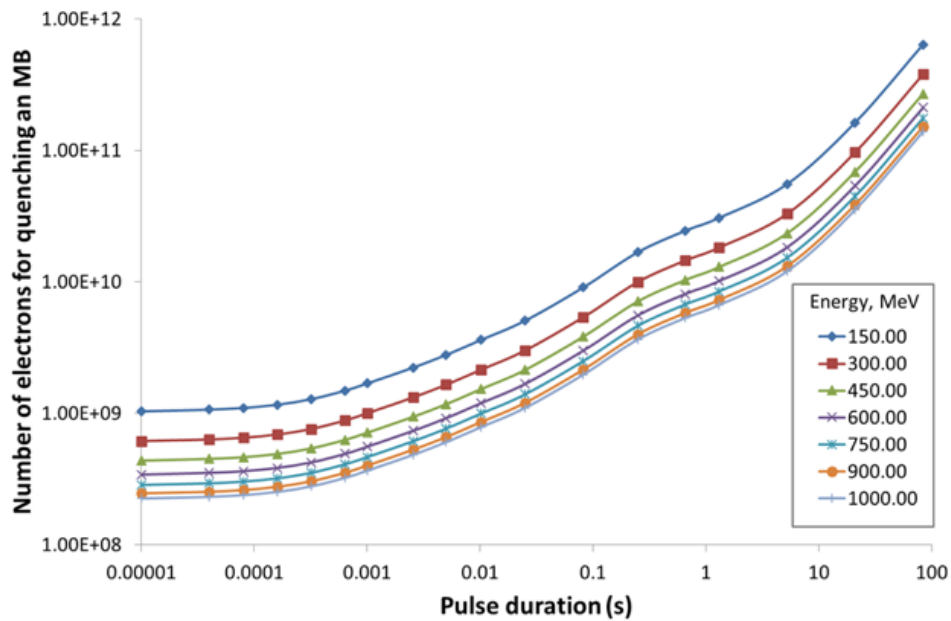
Figure 2.3: Amount of impacting particles versus pulse length to reach the quench level of
a LHC main dipole. The energy density distribution is taken from the FLUKA
simulations shown in Fig. 2.1 and 2.2.

²²⁴ vide sufficient beam to perform quench tests during all stages of its construction. It is
²²⁵ important to assure in a subsequent detailed design process that the facility can provide
²²⁶ fast and slow extracted beams to the quench test experiments, to allow for experiments in
²²⁷ all energy deposition duration regimes.

²²⁸ **Quench test facility**

²²⁹ Besides a high energy electron beam, the quench experiments require a dedicated facility.
²³⁰ The detailed design and space requirements of such a facility change strongly depending
²³¹ whether it should allow for testing full size magnets like the LHC dipoles or if testing of
²³² cable and short magnet samples would be sufficient. In both cases such a facility requires
²³³ power converters, which deliver currents up to ~ 25 kA to power the samples and possible
²³⁴ solenoid magnets providing external magnetic fields. Furthermore instrumentation racks
²³⁵ for quench protection, measurement of voltages, temperatures and other parameters are re-
²³⁶ quired. Most importantly it requires a dedicated cryogenic installation, to avoid impacting
²³⁷ the operation of PERLE.

²³⁸ One may start with a facility for testing cable samples and short sample coils, which, at
²³⁹ a later stage, can be extended with a test bench to perform quench tests with full size mag-
²⁴⁰ nets, as it is e.g. done at CERN in the SM18 test area. The space and power requirements
²⁴¹ of the final facility have to be taken into account from the beginning.

²⁴² ## 2.2.2 Cavity tests at different frequencies

²⁴³ PERLE is described below in a default configuration including cavities at 801.58 MHz in
²⁴⁴ up to 4 cryomodules and a bunch spacing of 25 ns. To gain flexibility and widen its po-
²⁴⁵ tential as a development facility for testing cavities and cryomodules with beam, PERLE
²⁴⁶ may, however, also be configured to a number of different frequencies, especially those
²⁴⁷ which are commonly used in accelerator facilities world-wide, i.e. 352 MHz (Linac4,
²⁴⁸ ESS), 401 MHz (LHC, FCC), 704 MHz (ESS), the PERLE default 802 MHz (LHC, FCC
²⁴⁹ and LHeC) and 1300 MHz (ILC, XFEL, ...). To make this possible, the injector must be
²⁵⁰ based on a photocathode with a laser pulser that can be operated at $f_0 = 12.146$ MHz with
²⁵¹ a buncher/booster system adjusted to a harmonic of f_0. The frequency of 12.146 MHz is
²⁵² chosen as a joint sub-harmonic of these commonly used frequencies. The exact harmonic
²⁵³ frequencies accessible as PERLE's main RFs are given in Table 2.1, assuming the pos-
²⁵⁴ sibility to tune the subharmonic f_0 by moderate variations of $\pm$ 4 kHz. This assumption

h	29	33	58	66	107
h ·(f_0 -4 kHz)	352.118	400.686	704.236	801.372	1299.19
h ·(f_0 +4 kHz)	352.350	400.950	704.700	801.900	1300.05

Table 2.1: Main RF ranges for selected harmonics, in MHz, accessible to PERLE with an injector pulsed at $f_0 = 12.146$ MHz, a configuration suitable for beam based RF developments at most commonly used frequencies with this facility.

translates to certain tuning range, for example at 801.58 MHz of ± 0.26 MHz, which would have to be implemented in the buncher/booster.

Referring to the description of source and injector in Sect. 4.1 below, it is clear that a bunch repetition frequency of 40.1 MHz (25 ns) is not compatible with most of the above frequencies and should be adapted to either 12.146 MHz, where it could be used with all mentioned frequencies, with the caveat that a larger bunch charge would have to be generated for a similar average current (challenging 1 nC for 12 mA). For tests at 401 MHz and 802 MHz, however, a bunch repetition frequency of 36.438 MHz can be chosen, which would be close enough to the LHeC parameters to be relevant. It would produce 12 mA of beam current with 329 pC bunch charge. The filling scheme and bunch recombination pattern, see Sect. 3.4 (Figs. 3.8, 3.9) would have to be adapted *mutatis mutandis* (the harmonic 20 becoming harmonic 22) with individual bunch spacings 7λ - 8λ - 7λ. The buncher/booster system described in Sect. 4.1 remained unchanged. It is noteworthy that for a bunch repetition frequency of 12.146 MHz, captured and accelerated in this booster at 801 MHz, the frequency of the cavities in the ERL might still be 704 MHz and 1300 MHz, and even the simultaneous operation at different frequencies in the same linac would not be impossible.

2.3 Injector for the LHeC

In the course of the PERLE development, it had been studied whether a suitably modified PERLE facility could serve as an injector to the LHeC eventually. From the beam dynamics point of view, many parameters are shared between the PERLE and the LHeC designs (emittance, bunch spacing, beam current...). When operated as an injector, PERLE would need to deliver beam without energy recovery, as the highly disrupted beam from the LHeC cannot accept a further deceleration. In the Higgs factory configuration, the LHeC requires

bunches up to 640 pC at an energy of 500 MeV which results in an average beam power at injection of about 10 MW. Assuming that the cavity design can handle such power flow, this would nevertheless drive the requirements for the klystrons and power converters, requiring new sets of them.

Concerning the layout, PERLE could, for example, be reconfigured keeping only two passages and lowering the accelerating field to 125 MV/linac in order to balance the power between the two of them. Further considerations have to be made:

- The LHeC requires continuous beam injection, therefore other applications of PERLE would be relegated to the LHeC downtime, thus disrupting its user program;

- If PERLE would be located at ground level on the CERN site, a some-hundred-metres tunnel, with a reasonable slope, has to be dug from the location of PERLE to the LHeC tunnel. A kilometre-scale transfer line will probably be needed to transport the beam to the LHeC injection chicane.

It should be noted that with the PERLE accelerating gradient of 15 MV/m, an active length of just 33 m is required to reach the LHeC injection energy even without recirculation. A dedicated linac, placed in a ∼100 m tunnel close to the LHeC injection chicane could be a preferable option. The possibility to reuse PERLE components for this machine could be taken into account. It so seems less preferable, though possible, to consider the genuine PERLE facility when located at CERN as an injector to the LHeC.

2.4 Physics with Electron Beam

Elastic ep scattering has been of fundamental importance since, now 60 years ago, it lead to the discovery of a finite radius of the proton of about 1 fm by Hofstadter [19]. This process has a major revival as recent determinations of the proton radius with electrons and muons strongly disagree, see below. With its outstanding luminosity and large energy range, hugely interesting opportunities open up with PERLE measurements of unprecedented precision. These, as sketched below, concern measurements of the scale dependence of the electroweak mixing angle, $\sin^2\theta$, of the electric and magnetic formfactors, G_E and G_M, of hyperon physics and searches for physics complementing the Standard Model. New physics may appear in loop corrections or in direct manifestations of new particles, for which dark photons, leading to the reaction $e^-A \to e^+e^-e^-A$, are currently a prime example [20, 21].

310   Following a brief recollection of the elastic scattering characteristics and the luminosity
311 prospects of PERLE, three interesting physics applications are illustrated subsequently
312 i) the potential for weak interaction measurements using polarised $e^- p$ scattering; ii) a
313 discussion of the status and possibilities for new precision measurements of the proton
314 form factors, pion production and iii) the search for light dark matter and new physics.

315 2.4.1 Elastic ep scattering and luminosity

316 For a given electron beam of energy, E, scattered off a fixed proton target, the elastic ep
317 cross section depends only on the polar angle θ of the scattered electron. This determines
318 both the negative four-momentum transfer squared, Q^2, and the energy E' of the scattered
319 electron through the relations

$$Q^2 = \frac{2ME^2(1 - \cos\theta)}{M + E(1 - \cos\theta)} \qquad E' = \frac{E}{1 + \frac{E}{M}(1 - \cos\theta)}, \qquad (2.1)$$

320 where M is the proton mass. The cross section, in its Born approximation, is given as
321 the product of four factors, the Rutherford formula, the Mott electron spin modification, a
322 correction, equal to E'/E, for the proton recoil and finally a function $f(G_E, G_M, \theta)$, which
323 characterises the spin and the spatial extension of the proton

$$\frac{d\sigma}{d\Omega} = \frac{\alpha^2}{[E(1 - \cos\theta)]^2} \cdot \cos^2\frac{\theta}{2} \cdot \frac{1}{1 + \frac{E}{M}(1 - \cos\theta)} \cdot f(G_E, G_M, \theta), \qquad (2.2)$$

324 with α the fine-structure constant. With the convention $\tau = Q^2/4M^2$ the form factor term
325 is given by

$$f(G_E, G_M, \theta) = \frac{G_E^2 + \tau G_M^2}{1 + \tau} + 2\tau G_M^2 \tan^2\frac{\theta}{2}. \qquad (2.3)$$

326 To some first approximation, one has $G_M = \mu_p G_E$ and $G_E = 1/(1 + Q^2/0.71 GeV^2)^2$, with
327 the anomalous magnetic moment μ_p of the proton. The two form factors G_E and G_M
328 can be separated through a variation of the energy following Rosenbluth. This should
329 be an advantage of PERLE as with its variable energy it may cover a large range from
330 a few hundreds of MeV to almost 1 GeV. The formulae above are sufficient for practical
331 estimates of counting rates, but neglect all the physics which is contained in corrections to
332 Eq.2.2 as arise from electroweak, BSM and higher order QED effects.

333   The luminosity of a facility like PERLE is obtained as $L = \rho l N_A N_e$. For a hydrogen
334 target of density $\rho = 0.07\,\mathrm{g\,cm^{-3}}$ and length $l = 10\,\mathrm{cm}$ one gets $L = 4.3 \cdot 10^{23}\,\mathrm{cm^{-2}}\,N_e$.
335 For a source delivering 320 pC of charge and a 25 ns bunch spacing one obtains a current

336 of 12.8 mA corresponding to about $8 \cdot 10^{16} \mathrm{e\,s}^{-1}$, or a number of electrons per bunch of

337 $N_e = 2 \cdot 10^9$. As a consequence the luminosity for elastic *ep* scattering can be expected to

338 be as high as $3 \cdot 10^{40}\,\mathrm{cm}^{-2}\mathrm{s}^{-1}$ with a 10 cm proton target.

339 2.4.2 Parity violation and the Weinberg angle

340 The unification of the electromagnetic and weak interactions within the $SU(2)_L\mathrm{x}U(1)$ the-

341 ory is expressed by the Weinberg angle $\sin^2\theta_W$, which has a strong characteristic depen-

342 dence on the momentum scale ($\sqrt{Q^2}$ in ep scattering) due to loop corrections [22] to the

343 tree-level expressions, see Fig. 2.4.
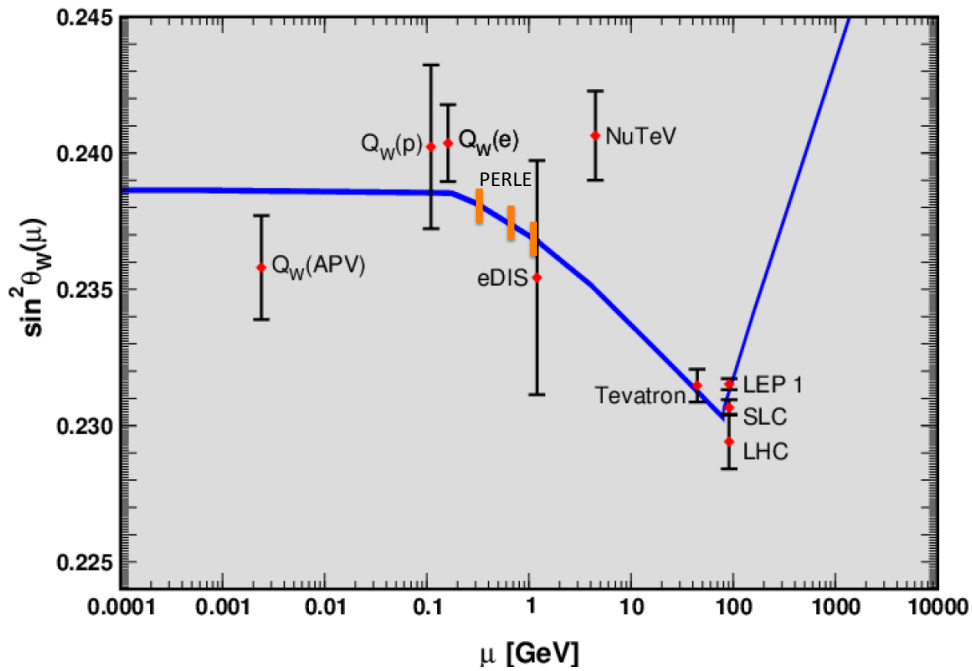
Figure 2.4: Prospect for the measurement of the weak mixing angle with PERLE (illustra-
tion of half a percent accuracy measurement) based on the polarisation asym-
metry A^-, as compared to the current status of $\sin^2\theta_W$ measurements, from
PDG2014.

344 The most precise $\sin^2\theta_W$ measurements so far were performed at the *Z* pole at LEP and

345 SLC, leading to an unresolved discrepancy of about three standard deviations. Various

346 measurements of so far limited precision were performed at low scales, with a departure

from theory observed by the NuTeV Collaboration in νN scattering which caused a multitude of subsequent considerations as on the amount of strange quarks in the nucleus and the behaviour of nuclear corrections. Measurements of the mixing angle are very complex challenges and lead to new insight often beyond the genuine intention to determine $\sin^2 \theta_W$. Measurements with the LHeC (FCC-he), as presented in the LHeC CDR [1], will be based on very large electroweak asymmetry effects and determine the electroweak mixing angle precisely for a range below the Z mass up to high scales of 1 (3) TeV.

With PERLE one can access effects from Z-boson exchange with polarised electron scattering, as well as with charge asymmetry measurements, for $\sqrt{Q^2}$ between about 0.1 and 1 GeV. The intensity of a polarised electron source is probably an order of magnitude higher than that of a positron source. This makes the measurement of a polarised electron scattering asymmetry, A^- more likely than that of a charged or combined charge and polarisation asymmetry, B. Both have been discussed in [23]. The polarisation asymmetry can be expressed as

$$A^-(P,P') = \frac{\sigma(P) - \sigma(P')}{\sigma(P) + \sigma(P')} = -\kappa \frac{P - P'}{2} \cdot (v_e A - a_e V) \tag{2.4}$$

where $\kappa = Q^2 G / \sqrt{2} 2\pi\alpha$ determines the size of the asymmetry to be $O(10^{-4} Q^2/\text{GeV}^2)$. Here v_e and a_e are the weak neutral current (NC) couplings of the electron and V and A are new combinations of the form factors G_E and G_M which also depend on the quark NC couplings as well as the charged current axial vector form factor. Evidently, the asymmetry A^- is different from zero through parity violation. With PERLE, it allows to measure the mixing angle in a particularly interesting range of scale, as is illustrated in Fig. 2.4. Besides providing a measurement of $\sin^2 \theta_W$, with ep scattering asymmetries, one accesses also new combinations of quark couplings. Following [23] one sees, for example, that the hadronic axial vector factor A determines a combination of $a_d + 3.55 a_u$ which can be compared with ep scattering at HERA and the LHeC where $A = a_d - 2a_u$.

The measurement accuracy depends on the beam energy and scattering kinematics. This is illustrated in Fig. 2.5. Since the asymmetries vanish at small angles while the cross section decreases towards larger angles, an optimum is observed, with striking variations. One finds for a beam energy $E \sim 1$ GeV that asymmetry measurements at $\theta \sim 30 - 90°$ can be expected to be especially precise.
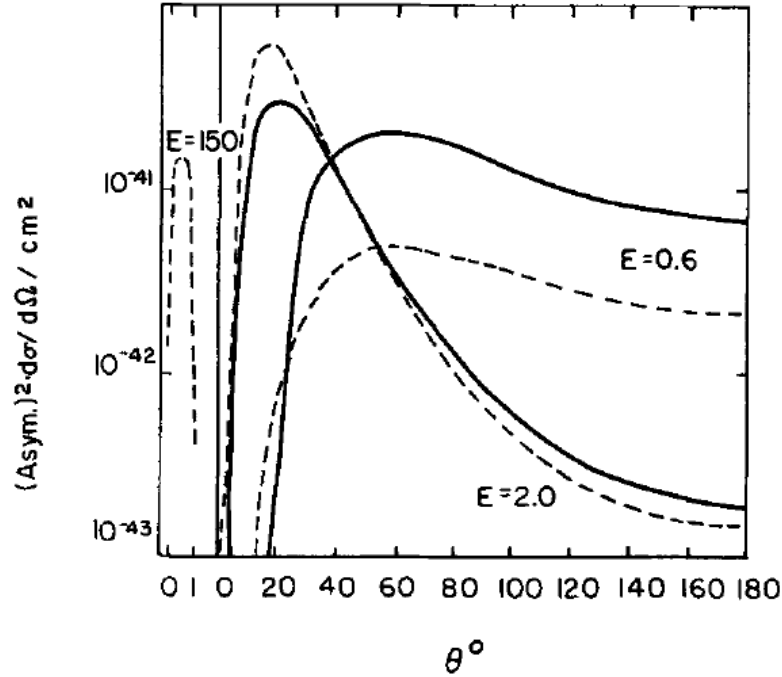
Figure 2.5: Variation of the statistical accuracy represented as asymmetry squared times cross section in cm^2 for two kinds of asymmetry, solid: beam charge conjugation and dashed: polarisation, from [23].

The measurement of the weak mixing angle at small scales is an area of vigorous activity, because of the new level of precision anticipated in a coming generation of tests of its predicted scale dependence, as at Mainz and Jefferson Lab, and because of the relation these measurements have to new physics such as rare Higgs decays and dark Z bosons, see [24] and references therein. The salient potential of the here presented ERL facility consists in its potential large energy coverage and particularly high luminosity which make further studies of the possibility to measure that process with PERLE interesting indeed.

2.4.3 Proton form factors

The proton electromagnetic form factors, G_E and G_M, which have been studied for many decades, have become the focus of recent research mainly due to the proton radius puzzle, recognised even in the popular press [25]. It is the more than 7σ discrepancy between the determination of the proton radius with electrons ($r_E = 0.8775(51)$ fm [26]) and using muon spectroscopy ($r_M = 0.84087(39)$ fm). Since its observation in 2010, the discrepancy
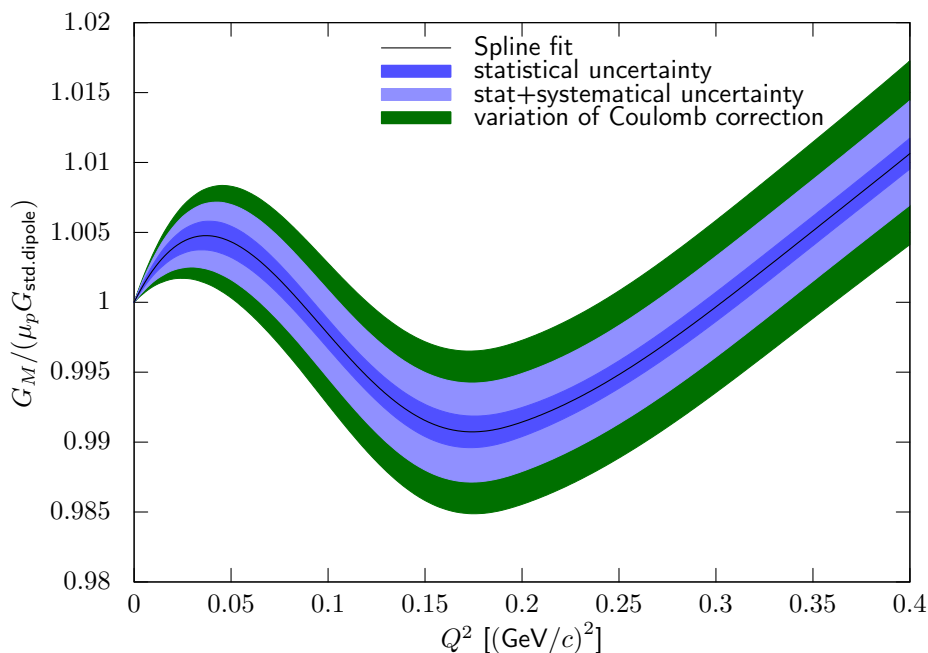
Figure 2.6: The fits in [29] for the magnetic form factor G_M, divided by the standard dipole, exhibit a maximum-minimum structure at low Q^2. While the local minimum around 0.2 $(\text{GeV}/c)^2$ is seen in earlier fits, the local maximum around 0.03 $(\text{GeV}/c)^2$ has not been observed before.

has sparked large work efforts on both the experimental and theoretical side, but no widely accepted explanation has yet been found.

On the electron side, both spectroscopy and scattering experiments agree. In the latter, the radius is extracted from the slope of the form factors at $Q^2 = 0$. Since data can only be taken at finite Q^2, the form factors have to be extrapolated to 0. Currently, the most precise data set from scattering experiments [27, 28, 29] has been measured by the A1 collaboration in Mainz at the MAMI accelerator. It contains more than 1400 measured cross sections and reaches closest to the static limit with $Q^2_{min.} \approx 0.003$ $(\text{GeV}/c)^2$. While there are no structures/changes of curvature expected below this point, it is not possible to rule them out. Such structures would invalidate the extrapolation and may resolve part of the puzzle.

This data set also found an interesting structure in G_M at low Q^2, shown in Fig. 2.6. The magnetic form factor, divided by the standard dipole, exhibits two local extrema. While the minimum is found in earlier extractions, the maximum has not been seen and is in fact below the resolution of previous data. This leads to a significantly different magnetic
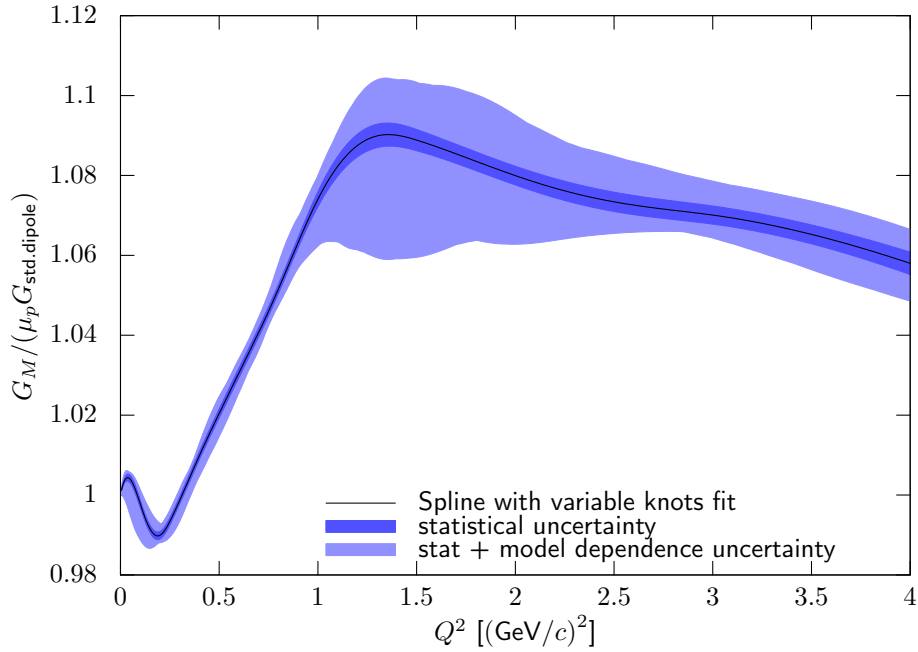
Figure 2.7: Fits to the world data (here from [29]) for the magnetic form factor G_M, divided by the standard dipole, show a cusp or strong bend between 1 and 1.5 $(\text{GeV}/c)^2$. The exact shape strongly depends on the form factor model used to fit the data.

radius compared to earlier findings. The strength of the maximum is strongly affected by radiative corrections and could be a statistical aberration. An external validation is important as the existence of structures like this points to corresponding length scales in the physics inside the proton.

Fits to the world data set exhibit a cusp around $Q^2 = 1.5$ $(\text{GeV}/c)^2$ in G_M, shown in Fig. 2.7, again pointing to underlying length scales in the internal structure of the proton. However, the cusp is only visible in the combination of multiple data sets and could be an artefact.

PERLE could provide crucial new high-precision data to study these three phenomena using different experimental approaches:

- Possible structures below Q^2_{min} and their influence on the proton radius could be studied with a single, low beam energy and forward scattering experiment, similar to the PRad experiment [30]. At lower energies and higher beam currents than planned for PRad, an ERL beam with a point-like target (e.g. a gas jet) could provide higher

rates and smaller systematic uncertainties. An alternative approach is to exploit initial state radiation, measuring deep into the radiative tail to probe Q^2-values that are orders of magnitude smaller than directly accessible. This approach is described in more detail e.g. in [31].

- The low-Q^2 structure in G_M could be studied in an experimental setup similar to [27]. The interesting region in Q^2 would be covered by performing an angular scan of the cross section and multiple energies up to 300 MeV. Such an experiment would benefit substantially from a point-like target without target walls, which are the main background of [27]. It would produce an electric radius with similar uncertainties, and a magnetic radius with substantially improved precision compared to current results. Additionally, with a polarised beam and target, an asymmetry measurement, sensitive to the ratio G_E/G_M, could be performed. Such a measurement would help to disentangle G_E and G_M from the cross-section measurement and would make it possible to study whether the structure is related to imperfect radiative corrections.

- The high-Q^2 structure could be studied with high precision using beam energies of 1 GeV and up, possibly with just one angular scan of the cross section at a fixed energy around 1.3 GeV. Without a good connection to lower beam energies, the precision of the absolute normalisation is not likely to better than a few percent, however the cusp structure is large enough that a good relative normalisation of the data points, e.g. using a detector at forward angles as a luminosity monitor, is enough to extract a meaningful result.

2.4.4 Pion electroproduction

Using virtual photon tagging, it is possible to study confinement-scale QCD. In photo-production, the photon tagger sets the rate limit and only a small fraction of the tagged photons interact with the target, leading to low data-taking efficiency. At forward angles, the virtual photons are almost real, so that a forward scattering electron tagger can be used as a highly efficient substitute. Because of the high efficiency and high beam currents, it is possible to use pure, thin targets and detect low energy recoil particles which would not escape traditional, thick targets. It is thus possible to measure the reactions $\gamma p \to \pi^0 p, \pi^+ n$, $\gamma n \to \pi^0 n, \pi^- p$ and $\gamma D \to \pi^0 D$. Coherent π^0 production in D and ^3He measure relative signs of the $\gamma p \to \pi^0 p, \gamma n \to \pi^0 n$ amplitudes.

Such an experiment requires beam energies of 300 MeV or more. Depending on the target, beam current and polarization capabilities, different experiments are possible:

- With about 1 mA unpolarized beam, a measurement with a thin, windowless, unpolarized gas target, detecting either the π^+ or the recoiling proton, could be performed. This would allow a test of $a_{nn} = a_{pp}$ and few-body calculations via $\gamma D \rightarrow nn\pi^+$, and also check a_{np} with $\gamma D \rightarrow np\pi^0$. It would further be possible to test isospin conservation by testing

$$A(\gamma p \rightarrow \pi^+ n) + A(\gamma n \rightarrow \pi^- p) = \sqrt{2}[A(\gamma n \rightarrow \pi^0 n) - A(\gamma p \rightarrow \pi^0 p)].$$

- At about 100 mA unpolarized beam with a windowless transverse polarized gas target, one could test isospin breaking through a measurement of $\gamma N \rightarrow \pi^0 N$ near threshold.

For more information, see e.g. [32].

2.4.5 Light dark matter

The search for new physics beyond the Standard Model is a major focus of the nuclear and particle physics community. A simple extension of the SM Lagrangian [33, 34] leads to new "dark" Abelian forces with a new dark gauge field A'. Among many others, a possible production mechanism is $e^- p \rightarrow e^- p A'(\rightarrow e^- p e^+ e^-)$, i.e. the elastic scattering with a radiated "dark" photon, and the possible subsequent decay of the radiated A' into a lepton pair ("visible decay") The DarkLight experiment [35], planned to be run at the Jefferson Lab ERL, aims to search for these visible decays in the region preferred by the muon g-2 results, detecting all four outgoing particles. A variant also looking for invisible decays is planned [36]. The PERLE facility could be an option for a version 2 of the experiment, with increased luminosity.

Alternatively, with high-precision, high-rate detectors measuring just the recoiling proton and electron, it should be possible to mount a competitive search sensible to both visible and invisible decays. More work is needed to study this further.

2.4.6 Speculative ideas

At Q^2 above $1\,\text{GeV}^2$, determinations of the form factor ratio from unpolarized and polarized measurement do not agree. This has been attributed to two-photon exchange, whose

size is directly tested in current experiments [37, 38, 39]. At lower Q^2, this effect is believed to be small, but could explain part of the proton ratio discrepancy. A positron source would make it possible to measure the effect directly at small Q^2, validating theoretical calculations.

The experiments described so far require a fixed target. Colliding beams open additional interesting possibilities. Head-on collisions with a high-momentum proton beam can probably not help with the physics described, however, if it could be arranged that the beam collide almost colinearly, i.e. essentially with the same, not opposite, direction, one would access the fixed-target equivalent of backward scattering at very low Q^2, accessing the magnetic form factor at unprecedentedly small four-momentum transfer. Similar, a collision of a muon and electron beam in this way would test lepton universality, a further possible explanation for the radius puzzle.

2.5 Physics with Photon Beam

This section is meant to briefly sketch the potential for fundamental research with γ-ray beams that the PERLE facility will be capable of producing by laser-Compton back-scattering off the intense cw electron beam. The production mechanism and expected γ-ray beam parameters will be described below. Since the scope of this Conceptual Design Report does not allow a comprehensive compilation of all possible research venues, this section includes only a limited selection of research opportunities.

Photonuclear science is currently witnessing a transformation of the field which has started [40] with the advent of intense, energy-tunable, completely polarized, quasi monochromatic γ-ray beams from laser-Compton back-scattering at the High Intensity γ-ray Source (HIγS) [41] at the Duke Free Electron Laser Laboratory (DFELL) at Duke University, Durham, NC, U.S.A., and will continue with the European Extreme Light Infrastructure - Nuclear Physics (ELI-NP) which is currently under construction in Magurele, Romania [13]. ELI-NP is expected to deliver first γ-ray beams in the energy range from 0.5 - 19.5 MeV with a band width of 0.5% and a peak-spectral density of 10^4 γs/(eV s cm^2) starting in 2017. Photonuclear science at ELI-NP is enjoying a strong international user community of 100 - 200 scientists who potentially could later be attracted to the PERLE γ-beam due to its expected superior performance, in particular with respect to intensity, band-width, and the CW time structure.

Photonuclear reactions impact on a variety of research topics in nuclear structure physics,
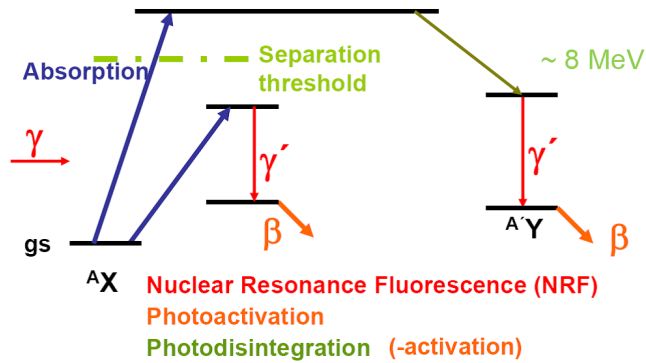
Figure 2.8: Photonuclear reaction modes that can be induced by photons with energies in the range of PERLE.

particle physics metrology, and nuclear astrophysics. From each of these fields, a selection of one or two examples is sketched below, in order to give a flavor of the research potential for an advanced γ-ray beam to be established at the PERLE facility, apart from additional commercial or medical applications.

2.5.1 Photonuclear reactions

Gamma-rays with energies up to 30 MeV can induce a variety of photonuclear reactions. Photoinduced nuclear excitations below the nuclear separation energy will decay by subsequent re-emission of γ-radiation. When this reaction proceeds via a nuclear resonance it is addressed as nuclear resonance fluorescence (NRF). The NRF process may populate an excited low-lying nuclear isomer which may decay by β-decay processes addressed as internal photoactivation.

Photodisintegration reactions become possible when a nucleus is photo-excited above the separation threshold. Then either neutrons or charged nuclear constituents such as protons or even α-particles can be emitted. Photodisintegration reactions that result in a daughter nucleus which is radioactive are called external photoactivation. An extreme mode of photodisintegration is photofission where a nuclear fission process occurs once the nucleus has been activated by the absorption of the γ-ray. The various photonuclear reactions are sketched in Fig. 2.8.

2.5.2 Nuclear structure physics

The field of nuclear structure physics addresses the investigation of the nuclear many-body problem and its understanding in terms of effective nucleon-nucleon interactions that emerge from QCD as the effective interaction between hadrons. Since the electromagnetic interaction is understood quantitatively, photonuclear reactions enable the separation of the photonuclear reaction mechanisms from the nuclear properties and thus nuclearmodel-independent measurements. Due to the clean reaction mechanism of γ-rays with the nucleus, its iso-vector and one-step character, the field of nuclear structure physics has tremendously profited from photonuclear research since the seminal works of Bothe and Gentner in 1937 [42].

2.5.2.1 Nuclear single-particle structure

The recent understanding of nuclear shell-evolution as a function of nucleon number and the contribution of effective three-body forces [43] to it make the precise measurement of effective single-particle energies in nuclei a research topic of high current interest. Photonuclear reactions offer a unique tool to study $E1$ and $M1$ single-particle excitations from the ground state. Of particular interest is the study of the nuclear spin-orbit splitting between a nuclear level with total spin quantum number $j_> = l + 1/2$ and its spin-orbit partner with spin quantum number $j_< = l - 1/2$. These single-particle orbitals are connected by a strong $M1$ matrix element of the order of 1 nuclear magneton (μ_N) that can be measured precisely by photonuclear reactions, e.g., by the measurement of ground state excitation widths Γ_0 in NRF measurements.

Also the relative assignment of various Nilsson orbitals in deformed nuclei can be clarified with photonuclear reactions. Once sufficiently intense and narrow band-width γ-ray beams will be available at the PERLE facility, it will become possible to study the electromagnetic excitation cross sections of the rotational band-head states of deformed, odd-mass isotopes in the rare-earth mass region [44].

2.5.2.2 Collective nuclear structures

Of particular interest is the study of collective nuclear excitation modes with photons. Prime examples are the Isovector Giant Dipole Resonance (IV-GDR) for a collective $E1$ excitation or the Scissors Mode of deformed nuclei for a collective $M1$ excitation mode. Both are fundamental modes of the nuclear many-body system and have intensely been

studied by photonuclear reactions [45]. Due to the limited spectral density and abundant low-energy background at previous bremsstrahlung sources, important questions are still not resolved. What is the quadrupole deformation of the scissors mode? How does the IV-GDR emerge as a function of excitation energy and what is its fine-structure? How does the decay of the components of the IV-GDR depend on their K-quantum number? What is the nature of the Pygmy Dipole Resonance (PDR) that rides on the low-energy tail of the IV-GDR and dominates the nuclear $E1$ response near the particle separation threshold? PERLE could contribute to answering these questions. Measurement of the intrinsic $E2$ matrix element between the scissors mode and the nuclear ground state requires the determination of the absolute monopolar $E2$ decay width between a state of the scissor mode band and the ground state band, e.g., the $J^\pi = 1^+$ band head of the scissors mode band and the 2_1^+ state of the ground state rotational band in a deformed even-even nucleus. The measurement of the monopolar partial decay width of interest, $\Gamma_{1^+ \rightarrow 2_1^+, E2} = \delta^2/(1+\delta^2)\Gamma_{1^+ \rightarrow 2_1^+}$, requires the measurement of partial decay width $\Gamma_{1^+ \rightarrow 2_1^+}$, which is routinely done in NRF experiments on the Scissors Mode, and the $E2/M1$ multipole mixing ratio, δ, of this γ-decay transition. This has not been done so far. Such a measurement will be achievable at the Compton-backscattered γ-beam of the PERLE facility by measuring the azimuthal NRF intensity distribution about the polarization plane of the γ-beam. The measurement will determine the quadrupole collectivity of the scissors mode and will open up a research program on how this collectivity is related to the nuclear shape (prolate, oblate or triaxial,...) and its underlying single-particle structure. The polarization and high intensity of the new γ-beam will open up another research field on the electric dipole response of nuclei below and above the nuclear separation threshold. Along the lines of research that have been started at the HIγS facility at DFELL, the strength, energy distribution and decay properties of the PDR can be studied with PERLE at much higher sensitivity than before. In particular it will become possible to excite the nucleus at a preselected excitation energy region in the PDR or in the IV-GDR and then to measure the decay γ-ray transitions either to the ground state or to low-energy excited states of interest. It will become possible to search for the PDR of deformed nuclei and to thereby answer the question if the PDR in deformed nuclei exhibits a splitting according to its K-quantum number components, $K = 0$ or 1. Until now, neither has the PDR been observed in deformed nuclei, nor has it been clarified if the γ-decay of the IV-GDR in deformed nuclei differs between its $K = 0$ or $K = 1$ components. A detailed understanding of these phenomena as a function of deformation, neutron excess, or excitation energy above

particle separation threshold will become possible.

2.5.2.3 Nuclear photofission

Nuclear fission represents an extreme case of collective nuclear behavior. It can be triggered by incident γ-rays in photofission processes. The cross section for photofission reactions is tremendously enhanced when the energy of the initially absorbed photon coincides with the excitation energy of a quasi-bound resonance in the hyperdeformed well of the nuclear fission barrier. Information on these photofission resonances provides valuable insight in the structure of heavy fissile isotopes that is very difficult to obtain otherwise. The geometrical type of the various fission resonances dictates the subsequent fission modes and thereby the distribution of resulting fission fragments. A technological, and even a commercial, impact of photofission resonances with respect to the handling of radioactive waist is conceivable.

An intense, narrow bandwidth γ-ray beam at the PERLE facility opens up an entire new route of research on photofission processes of long-lived actinides. Its high photon flux will make photonuclear experiments on small samples in the milligram range possible. Its narrow bandwidth allows for a high energy resolution in experimental searches for new photofission resonances by energy-scans through the relevant excitation energy region. A better understanding of the fission processes, in particular of long-lived trans-uranium actinides is of very high interest of the society.

2.5.3 Particle physics metrology

Due to our understanding of the unified electroweak interaction, the electromagnetic reaction processes of photons with nuclei are closely related to nuclear reactions involving the weak interaction [46]. Consequently, photonuclear studies can, at least partly, shed light on weak interactions in materials that are employed in detectors for weak-interaction processes such as detectors for searching for neutrinoless double-beta decay or for neutrino signals from supernovae.

2.5.3.1 Nuclear matrix elements for $0\nu\beta\beta$-decay

It has recently been demonstrated [47] how photonuclear investigations on the $M1$ strength distribution of initial and final nuclei in $0\nu\beta\beta$-decay reactions can help to improve the theory for $0\nu\beta\beta$-decay matrix elements. Knowledge of these matrix elements will be

mandatory for the determination of the neutrino mass once the $0\nu\beta\beta$-decay rate would have been measured. The $M1$ decay branching ratio was recently found to be linked to the $0\nu\beta\beta$-decay branching ratio to the low-energy 0^+ states of the final nucleus.

2.5.3.2 Detector response to stellar neutrinos

Supernovae are bright sources for neutrinos. Detectors for the measurement of neutrinos from supernovae are operational or under construction. Due to neutrino oscillations, not all of the neutrinos reaching the detector will be electron-neutrinos ν_e but may have oscillated to other possible neutrino-flavors. Non-ν_e neutrinos with typical energies of a few MeV may react on the detector material by neutral-current scattering processes, that may be inelastic and are expected to be dominated by Gamow-Teller type matrix elements from the ground state. These are closely related to the matrix elements for $M1$ excitations. In order to be able to quantitatively interpret the signals from neutral-current neutrino scattering on detector material it is important to precisely know and understand the $M1$ excitation strength distributions of nuclei present in the detectors searching for stellar neutrinos.

2.5.4 Nuclear astrophyics

Energetic γ-rays belong to the thermal environment in stars. Understanding of nuclei in the variety of stellar conditions requires a detailed knowledge of photonuclear reactions. Research opportunities for photonuclear reactions in nuclear astrophysics are numerous. We will mention only two examples.

2.5.4.1 Stellar capture reactions

Stellar capture reactions, such as (p, γ), (n, γ), or (α, γ) determine the vital "energy production" in stars. For stars slightly heavier than our sun the CNO-cycle dominates, by which 4 protons are converted into an α-particle and released binding energy in a sequence of capture and decay reactions on carbon, nitrogen, and oxygen isotopes. Break-out of the CNO-cycle can occur, when the stable ground state of ^{16}O will be populated. Of particular interest is the cross section for the ^{12}C$(\alpha, \gamma)^{16}$O reaction at energies corresponding to stellar temperatures. This cross section is very small, therefore difficult to measure, and despite of its importance, not known. By the principle of detailed balance in time-reversal invariant reactions valuable constraints could be obtained from the inverse reaction ^{16}O$(\gamma, \alpha)^{12}$C which could be studied with an intense quasi-monochromatic γ-ray beam. A

corresponding research program has started at HIγS but suffers from too low intensity (10^3 γ/(eV s)) and too large energy-spread (1 - 3%). The superior properties of PERLEs γ-ray beam will facilitate these measurements.

2.5.4.2 Nuclear synthesis

One of the most outstanding physics questions is that to origin of the chemical elements in nature. Heavy nuclei beyond iron are produced in the various capture processes in stars, while latest research results indicate that supernova explosions are not capable of producing a sufficient amount of elements heavier than silver [48]. Very heavy elements, such as Thorium or Uranium, undoubtedly require a rapid-neutron capture process (*r*-process) in a dense and hot environment with a high neutron flux. In order to understand the survival rate of just synthesized heavy nuclei one needs to understand their reactions on the thermal radiation. Thermal γ-rays are capable of inducing photoactivation reactions on seed-nuclei and transforming them in other species. Stellar photonuclear reactions on stable nuclei will become possible to be studied at the PERLE γ-ray beam with unprecedented sensitivity.

2.6 Detector Test Beam Use

PERLE will accelerate electrons up to about 1GeV of energy. Complementary to other user test beam options world-wide (see [49], [50]) such beams would allow dedicated studies of single particles effects at lower energy for

- new tracking detectors such as
  - micro-pattern gas detectors SiPM
  - new (thin) pixel/strip sensor technologies
  - new detectors for luminosity monitoring
  - heavy fibers, new scintillating crystals;
- detailed effects of electromagnetic calorimeter measurements (very high resolution sampling at normal and low temperature);
- novel detector systems concepts, etc.

Detailed tests of detector samples and components for the upcoming High Luminosity LHC, nuclear physics experiments or other colliders to follow could be performed at a

PERLE testbeam. The beam energy would be low. A special application then may be to calibrate detectors one would build for the physics with PERLE.

For a test-beam extension of the PERLE scope, the following aspects are important:

- the extraction and shaping section has to be foreseen in the design ensuring the space and elements necessary are available;

- a beam line enclosure with instrumentation;

- suitable shielding, transportation and escape routes have to be taken into account when space requirements for the experimental setup are being discussed;

- Interlock system;

- Magnet control for momentum selection;

- Patch panels with pre-installed cables;

- Gas warning systems;

- Fast internet connection;

- light weight (state of the art) trigger setup; fast and precise.

A strong community for an electron/photon user facility exists. A test beam use of PERLE would provide the host laboratory with an extra attraction which one may compare with DESY's electron test beams.

An important consideration for building a facility such as PERLE is the education and training of young scientists in the complexity of experimental particle and nuclear physics. For young physicists it is often difficult getting involved in all phases of HEP experiment, its development and running, especially when engaged in the large LHC experiments. The preparatory phases for detectors are getting longer and usually only a few aspects can be studied by one person in detail. The data taking periods of current experiments are longer and generations of students never get to work on the/a real detector.

Test beam studies allow education in many respects as in the experimental preparation, trigger setup and evaluation, data acquisition, data taking (shifts, on-call), or software on track reconstruction or alignment. A test beam configuration at PERLE appears attractive to consider indeed.

CHAPTER 3

Design and Parameters

The PERLE facility aims at a maximum of $1\,\mathrm{GeV}$ energy recovery demonstration of a recirculating SC linear accelerator. The test facility should serve as a test bed to gain quantitative and qualitative understanding of the electron beam recovery process. The accelerator development purposes of this test facility, as introduced above, are first, confirming the feasibility of the LHeC ERL design by demonstrating stable intense electron beams with the intended parameters (current, bunch spacing, bunch length); secondly, testing novel accelerator components such as a (polarized) DC electron gun, SC RF cavities, cryomodule design and feedback diagnostics; finally, experimental studies of the lattice dependence of stability criteria. The realisation of this facility will allow addressing several physics challenges such as maintaining high beam brightness through preservation of the six dimensional emittance, managing the phase space during acceleration and energy recovery, stable acceleration and deceleration of high current beams in CW mode operation. The facility design must also allow addressing other performance aspects such as longitudinal phase space manipulations, effects of coherent synchrotron radiation (CSR) and longitudinal space charge, halo and beam loss and microbunching instability. These issues could have sizeable impacts on machine performance in the region of the design parameter space. Thus a design emerges of a system that, in principle, needs to be flexible in supporting multiple operating points and indeed, provides a reasonable validation of the LHeC accelerator baseline.
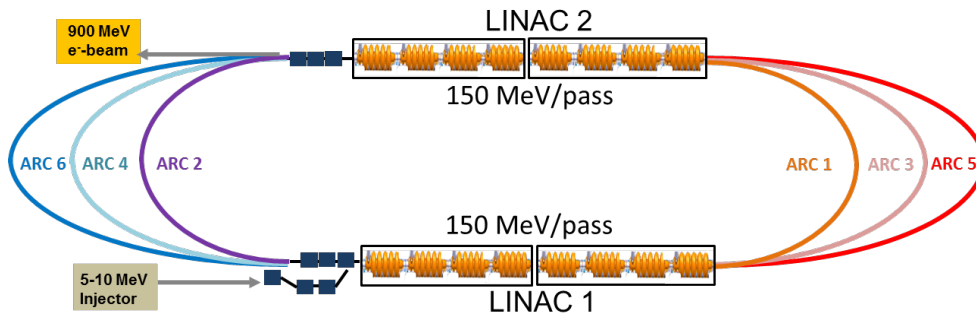
Figure 3.1: PERLE configuration of two parallel linacs comprising two 4-cavity cryomod-
ules each to achieve 150 MeV acceleration per linac and 300 MeV per pass.
There are up to three passes. There will be a pre-acceleration unit following
the source to enter the ERL with relativistic electrons (>5 MeV).

PERLE may be constructed in stages from initially 150 MeV to nearly 900 MeV in
3 steps. The final baseline design of the ERL configuration (Fig. 3.1) would consist of
the following elements:

1. a 5 MeV to 10 MeV energy injector;

2. two 150 MeV linacs each consisting of eight 5-cell SC structures;

3. optics transport lines including spreader regions at the exit of each linac to separate
   and direct the beams via vertical bending, and recombiner sections to merge the
   beams and to match them for acceleration through the next linac;

4. beam dump at $5 - 10$ MeV.

Each beam recirculates up to three times through both linacs to boost the energy to
900 MeV. To enable operation in the energy recovery mode, after acceleration the beam is
phase shifted by $180\,^\circ$ and then sent back through the recirculating linac at a decelerating
RF phase. During deceleration the energy stored in the beam is reconverted to RF energy
and the final beam, at its original energy, is directed to a beam dump. The set of main
parameters incorporated into the ERL prototype injector is shown in Table 3.1.

TARGET PARAMETER	VALUE
Injection energy [MeV]	5-10
Maximum energy [GeV]	1
Normalised emittance $\gamma\varepsilon_{x,y}$ [mm mrad]	6
Average beam current [mA]	15
Bunch spacing [ns]	25
Bunch length (rms) [mm]	3
RF frequency [MHz]	801.58
Duty factor	CW

Table 3.1: Basic Parameters of PERLE

3.1 System Architecture

PERLE may be constructed in stages. A first phase would only use two 4-cavity cryomodules, minimally one. With a single pass it could reach 150 MeV and be used for injector studies and SC RF tests (Fig. 3.2). A subsequent upgrade could be the installation of two additional arcs on each side to raise the beam energy up to 450 MeV (Fig. 3.3). This configuration accommodates for available space for implementation of feed-back, phase-space manipulations, and beam diagnostic instrumentation, giving the possibility of a full validation testing with energy recovery. In phase 3, as shown above (Fig. 3.1), four additional cavities in each linac will be added to permit energy recovery recirculation tests at full energy. The facility, in this final configuration, could represent, in principle, a smaller clone of the final LHeC project and could serve as a model for a pre-accelerator/injector to the final 60 GeV machine, see 2.3.

3.2 Transport Optics

Appropriate recirculation optics are of fundamental concern in a multi-pass machine to preserve beam quality. The design comprises three different regions, the linac optics, the recirculation optics and the merger optics.

A concise representation of multi-pass ERL linac optics for all six passes, with constraints imposed on Twiss functions by sharing the same return arcs by the accelerating

Figure 3.2: The facility is designed in a modular way. This picture shows a Step 1 layout of two parallel cryomodules to achieve $\sim 75\,\text{MeV}$ acceleration per linac and a final beam energy of 155 MeV (or half of it with just one initial cryomodule).

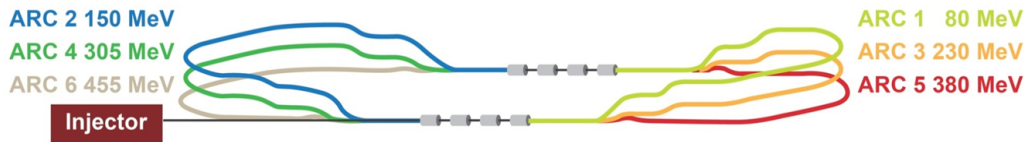
Figure 3.3: A second phase with recirculation could feature three-pass operation to reach 455 MeV.

and decelerating passes, is presented in Fig. 3.4.

Due to the demand of providing a reasonable validation of the LHeC concept, the system is oriented towards employing a Flexible Momentum Compaction (FMC) cell based lattice. Specifications require isochronicity, path length controllability, large energy acceptance, small higher-order aberrations and tunability. An example layout which fulfils these conditions is shown in Fig. 3.5, describing the lowest energy arc optics as an example. It includes a two-step achromat spreader and a mirror symmetric combiner to direct the beam into the arc. The vertical dispersion introduced by the first step bend is suppressed by the quadrupoles located appropriately between the two stages. The switchyards separate all 3 arcs into a 90 cm high vertical stack, the highest energy arc is not elevated and remains at the linac-level. A horizontal dogleg, used for path length adjustment and made of 3–13 cm long dipoles, is placed downstream of each spreader providing a tunability of ± 1 cm ($10\,^\circ$ of RF).

The recirculating arc at 155 MeV is composed of 4–70 cm long dipoles to bend the beam by $180\,^\circ$ and of a series of quadrupoles (two triplets and one singlet). A complete first-order layout for switchyards, arcs and linac-to-arc matching sections has been accomplished for
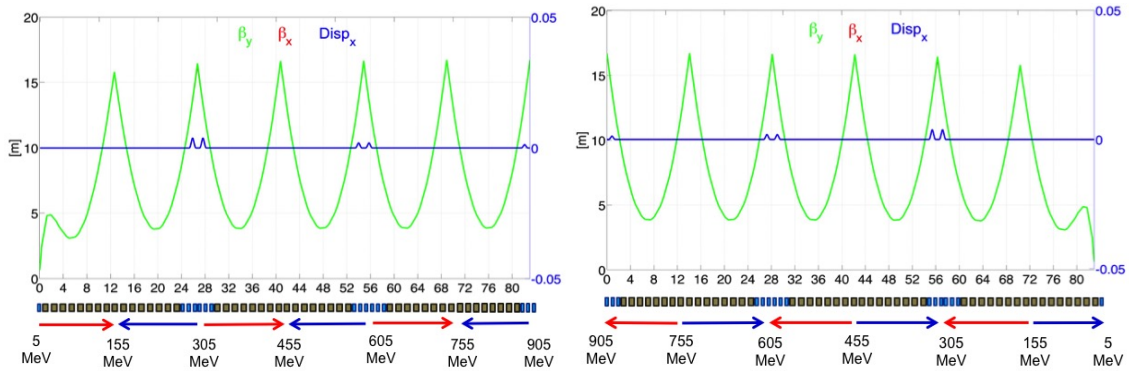
Figure 3.4: ERL multi-pass linac optics. The requirement of energy recovery puts a constraint on the exit/entrance Twiss functions for the two linacs. Green and blue curves show, respectively, the evolution of the beta functions amplitude and the horizontal dispersion for Linac 1 (left) and Linac 2 (right). Red and blue arrows indicate the passages of acceleration and deceleration.
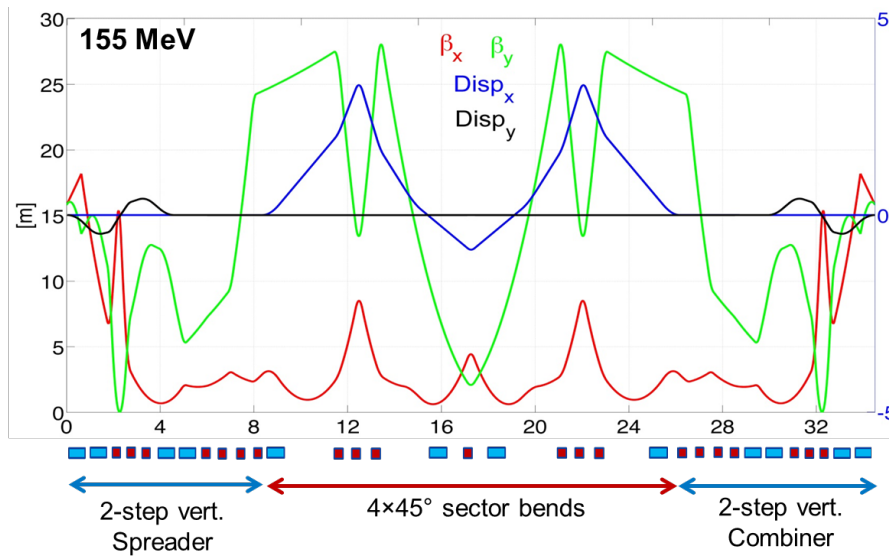
Figure 3.5: Optics based on an FMC cell of the lowest energy return arc. Horizontal (red curve) and vertical (green curve) beta-functions amplitude are illustrated. Blue and black curves show, respectively, the evolution of the horizontal and vertical dispersion.
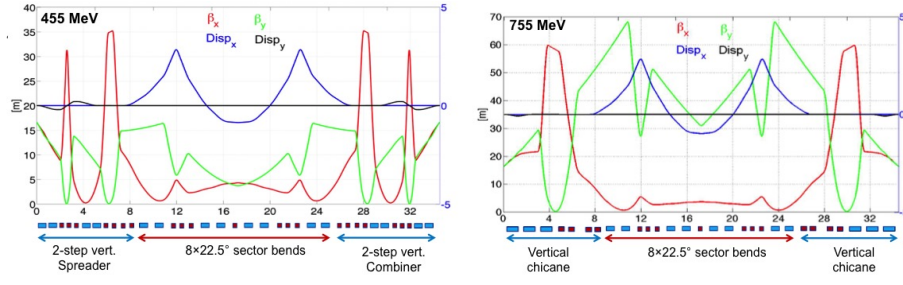
Figure 3.6: Optics layout of the arcs at 455 MeV and 755 MeV. The arc at 755 MeV is not elevated and remains at the linac-level, the spreader/combiner consists of a vertical chicane with 60 cm long dipoles. Horizontal (red curve) and vertical (green curve) beta-functions amplitude are illustrated. Blue and black curves show, respectively, the evolution of the horizontal and vertical dispersion.
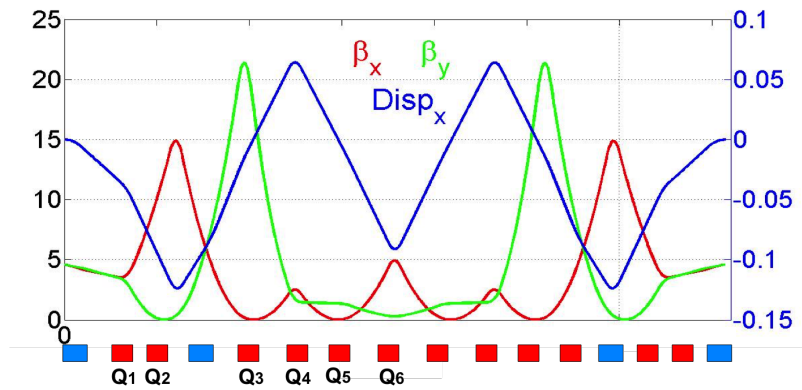
Figure 3.7: Injection chicane optics at 5 MeV.

all the arcs on both sides. Arc 3 and Arc 5 are presented in Fig. 3.6.

Injection into the racetrack at 5 MeV is accomplished through a rectangular chicane, which bypasses the arcs. The injection chicane is configured with four identical rectangular bends and 11 quadrupoles distributed in a mirror symmetric fashion, leaving six independent quadrupole gradients to control: betas and alphas at the beginning of the linac (4 parameters), momentum compaction (1 parameter) and the horizontal dispersion (1 parameter). The resulting chicane layout and optics are illustrated in Fig. 3.7. The chicane optics features a horizontal achromat, by design, with tunable momentum compaction to facilitate bunch-length control and finally with Twiss functions matched to the specific values required by the linac (Fig. 3.7).

Segment	Length [m]
ARC 1	35.98
ARC 2	35.74
ARC 3	35.61
ARC 4	35.74
ARC 5	35.98
ARC 6	34.43
PASS 1	99.86
PASS 2	99.48
PASS 3	98.55
Total	297.9

Table 3.2: Beam path for a full 3 pass accelerating ERL.

3.3 Layout and Magnet Inventory

The path of each pass is chosen to be precisely an integer number of RF wavelengths, except for the highest energy pass whose length is shifted by half an RF wavelength to recover the energy through deceleration. The total beam path for a full 3 pass accelerating cycle is around 300 m. This leads to an approximate footprint of 43 m × 16 m of the ERL itself. Accurate values are presented in Table 3.2.

Diverse plausible optics layouts have been studied. A possible option would consist of arcs with identical configurations in order to have compact magnets stacked on top of each other.

A preliminary inventory of the magnets of the LHeC Test Facility lists:

- 40 bending magnets (vertical field);

- 36 bending magnets (horizontal field) in the spreaders / combiners;

- 114 quadrupole magnets;

- 6 magnets in the injection / extraction parts;

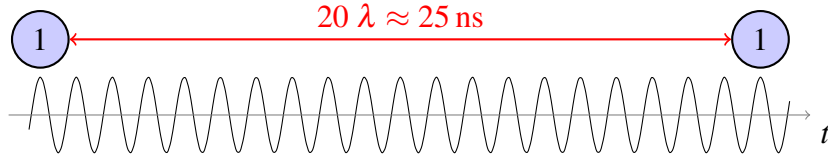- a few magnets for path length adjustment.

Figure 3.8: Basic RF structure, without recirculation. Bunches are injected every 25 ns. The waves indicate the RF electromagnetic oscillations.

Turn number	Total pathlength
1	$n \times 20\lambda + 7\lambda$
2	$n \times 20\lambda + 6\lambda$
3	$n \times 20\lambda + 3.5\lambda$

Table 3.3: Summary of the total path lengths of each turn of the ERLF design.

3.4 Bunch Recombination Pattern

The bunch spacing at the injector, dump and delivered is 25 ns, as shown in Fig. 3.8. However, due to continuous injection and the recirculation, more bunches at different energies are interleaved in the linacs, appearing in periodic sequences. The spreader and combiner design, employing fixed-field dipoles, do not pose timing constraints. For this reason the recombination pattern can be adjusted by simply tuning the length of the return arcs to the required integer number of λ.

In order to minimise collective effects, the arc lengths have been tuned avoiding to combine different bunches in the same bucket, like it would happen if the full turn length was an integer number of 20λ. On the contrary, the lattice is adjusted to achieve a nearly constant bunch spacing.

Special care has been taken to select a pattern that maximises the distance between the lowest energy bunches inside the RF structure: the ones at the first and the last turn, as shown in Fig. 3.9 and summarised in Table 3.3. This comes from the fact that, with a nearly constant β function, the kicks from HOMs are more disruptive at lower rigidities, thus, if two low energy bunches follow each other, the BBU threshold current can be reduced.
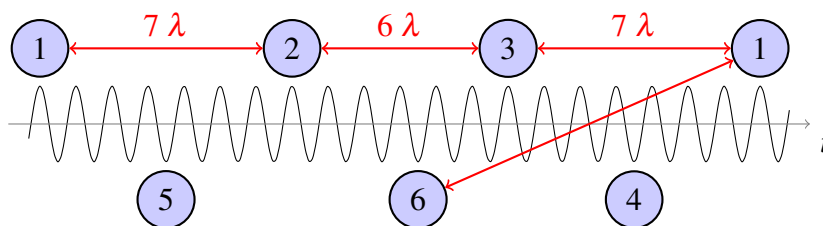
Figure 3.9: When the recirculation is in place, the linacs are populated with bunches at different turns (the turn number is indicated). The recombination pattern shown maximises separation inside the RF structure between the low energy bunches (at the first and sixth turn).

3.5 End-to-end Beam Dynamics Simulations

Tracking simulations have been performed initially with the tracking code elegant [51], to investigate single-bunch effects as the coherent synchrotron radiation (CSR) and the impact of multipolar field components, and later with PLACET2 [52], to verify the recombination pattern and asses the BBU threshold current.

3.5.1 Single-bunch end-to-end

PLACET2 is a tool that allows to describe the whole machine without unrolling the lattice and computes the element phases according to the beam time of flight. The β functions and the energy profile shown in Fig. 3.10 are obtained following a test bunch into the lattice from the injector to the dump. The energy profile shows that the lengths of the arcs are properly tuned to obtain the maximum acceleration and deceleration. The regularity and the symmetry of the β functions, validate the matching of all the arcs in the presence of strong RF-focussing from the linacs.

Figure 3.11 shows the transverse phase space at 900 MeV: the plots show the emittance preservation, and in particular the absence of non linearities. Collective effects such as coherent synchrotron radiation and short-range wake fields are not included, however analytical computations predict a small impact.

Comparing the longitudinal phase space at injector and at dump (see Fig. 3.12) one can note that the bunch length is well preserved, proving the isochronicity of the whole lattice. A small energy chirp is present at the dump, which shall be removed with a fine tuning of
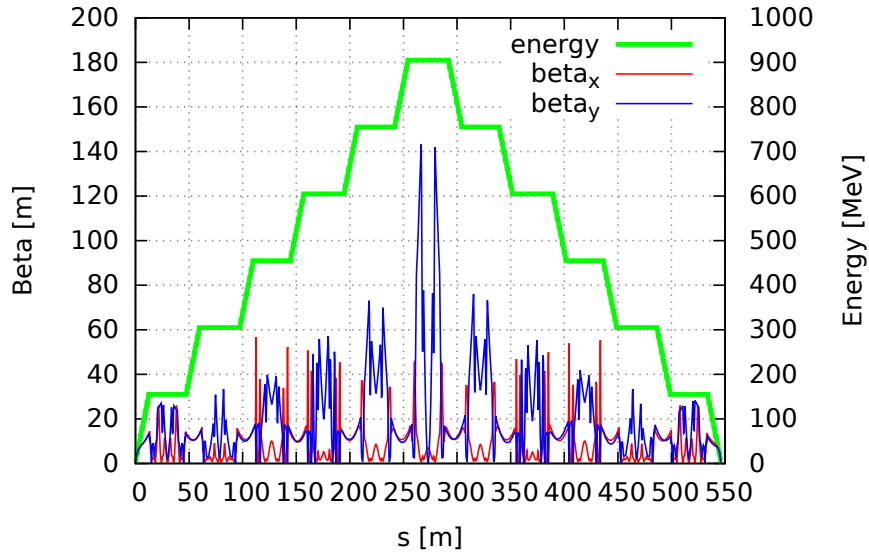
Figure 3.10: Energy and twiss parameter tracked with PLACET2
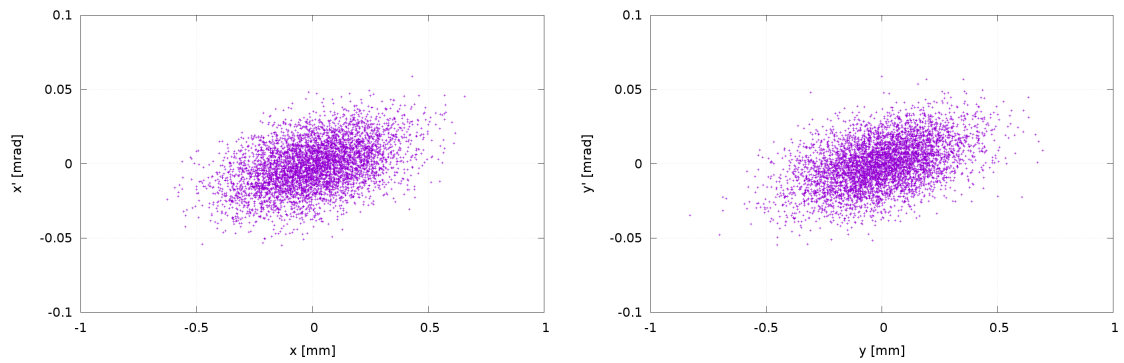
Figure 3.11: Horizontal and vertical phase space at 900 MeV.
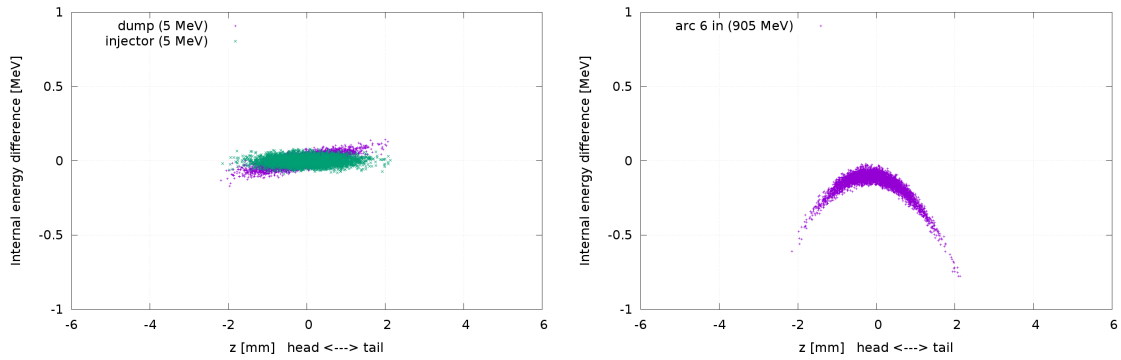
Figure 3.12: Longitudinal phase space at injector/dump (left) and at 900 MeV (right).
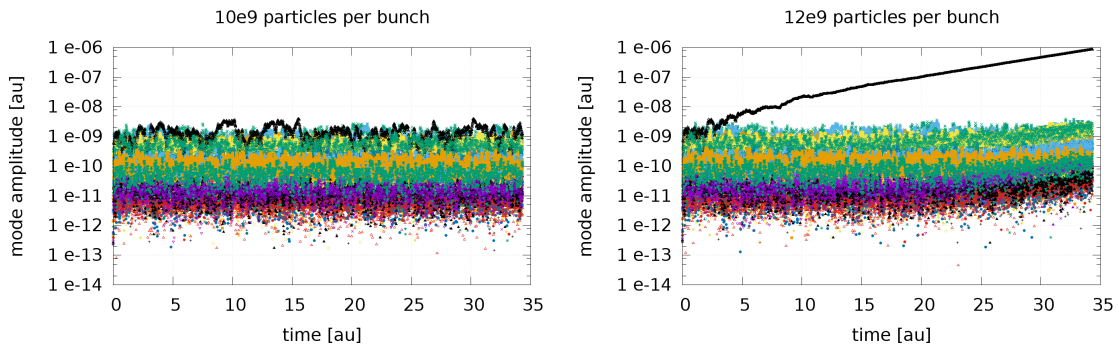
Figure 3.13: Evolution of the amplitudes of the dipole modes for two different charges per bunch.

the arc lengths. Figure 3.12 (right) shows the longitudinal phase space at 900 MeV. While the curvature induced by the RF can be seen, the total energy spread remains extremely contained (below 0.01 %).

3.5.2 Multi-bunch tracking and BBU

PLACET2 is capable of tracking many bunches simultaneously in the lattice preserving their time sequence everywhere in the machine. This allowed to verify the bunch recombination pattern and assess multi-bunch effects in a realistic operational scenario.

Estimations of the BBU threshold current have been performed using the major 26 dipole modes of the SPL cavity design, scaled to 802 MHz. A 6D distribution of 100 macro-particles per bunch has been used and tens of thousand of bunches have been

tracked, simulating the continuous operation. The statistical fluctuations of the positions of the bunch centroids are enough to excite the HOMs without the need of further perturbations.

A Gaussian spread has been introduced in the frequencies of the cavity HOMs assuming a detuning factor of 1×10^{-4}. It has been verified that for the final design stage, including a total of 16 cavities, different detuning seeds lead to similar results.

The plots in Fig. 3.13 show the amplitudes of the HOMs in one of the cavities as many bunches pass by. One can see that when the bunch charge is increased from 1.6 nC to 1.9 nC a mode starts to build up in the vertical plane leading to an instability. Note that this bunch charge is more than 5 times the one foreseen for operation.

Components

4.1 Source and Injector

The injector of PERLE needs to deliver beams with an average current of O(10) mA (with the possibility of future upgrades to deliver polarised electrons) and an energy of about 5 MeV. Bunches with a charge of 320 pC or higher follow with a repetition rate of 40.1 MHz (20th subharmonic of the ERL RF frequency 801.6 MHz). The parameters of the required beam are summarised in Table 3.1.

In principle, there are several possibilities to meet these specifications. As the requirement to normalised emittance is rather modest, it can be delivered with a grid modulated thermionic gun followed by a multi stage bunching-accelerating structure, similar to the one realised at ELBE [53]. This choice, however, will rule out any future upgrade to deliver polarised electrons. Photocathode guns, where electrons are emitted from the photocathode illuminated with laser light, are more flexible in terms of the beam charge and temporal structure and allow operation with both polarised and unpolarised photocathodes. Photocathode guns utilise different accelerating technologies ranging from DC to superconducting RF, but presently only DC technology may be considered as mature and applicable to PERLE. DC guns successfully operate at different ERL facilities [54, 55, 56]. The injector experiment at Cornell University demonstrated an average current of 52 mA with a GaAs photocathode and of 65 mA with a Cs2KSb photocathode [57].
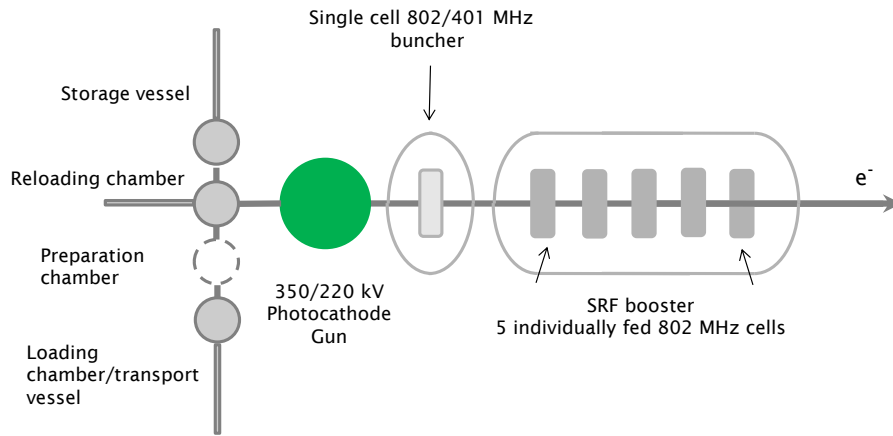
Figure 4.1: General layout of the photoinjector for PERLE (see text).

DC photocathode guns are widely used for production of polarised electrons because of their possibility to reach extra high vacuum conditions with a pressure of less than 10^{-11} mbar. That is required for providing long lifetime of polarised photocathodes with typical oxygen dark lifetime $2 \cdot 10^{-8}$ mbar·s. This vacuum is also sufficient for operation with antimonite based photocathodes with dark lifetime of 10^{-5} mbar·s which are considered as a source of unpolarised electrons. In addition, modern GaAs based photocathodes have reasonable quantum efficiency of $\sim 1\%$ and are able to produce electron beams with polarisation of higher than 85% [58, 59]. For PERLE a photoinjector schematic is considered as shown in Fig. 4.1. It comprises a DC photocathode gun surrounded by a well-developed photocathode delivery/production infrastructure, a single cell buncher cavity which compresses the beam at the exit of the gun, and a booster which accelerates the beam to $\sim$5 MeV.

4.1.1 Photocathode - sources of electrons

Physical parameters of the beam, delivered by the photocathode, are essentially defined by the gun. It also dictates the parameters of the drive laser. Photocathodes are typically characterised by their quantum efficiencies (Q.E.), defined as the ratio of extracted electrons to

incident photons, its dependence on the energy of incident photons and characteristics of photocathode material. The last parameter defines the laser wavelength which should be used to extract the beam. Difference between energy of incident photons and work function defines initial energy of emitted electrons. In combination with the angular distribution of emitted electrons it determines the initial beam emittance [60].

Originally, in DC guns for ERL application, GaAS photocathodes were used illuminated with laser light with a wavelength of 532 nm [61, 62]. These photocathodes are usually activated to the surface state close to Negative Electron Affinity (NEA) in the gun with Caesium dispensers. This procedure was difficult to properly control and thus does not allow reaching high quantum efficiency, typically few percent. Another problem of GaAs photocathodes is the requirement to ensure high vacuum conditions in the gun and poor lifetime due to back ion bombardment which does not allow reaching high average current for reasonable long time. More recent designs at Cornell University, Daresbury Laboratory [63] and JAEA-KEK [64] proposed activation of the photocathodes in a dedicated preparation facility directly connected to the gun and to replace photocathode in the gun as operating photocathode degrades. GaAs photocathodes prepared separately following this approach reached maximum Q.E. of 20% at operational wavelength, but did not solve the problem of lifetime.

More robust photocathodes based on Sb are less sensitive to vacuum conditions and to back ion bombardment. Pioneering experiments at Boeing [65], and the University of Twente [66], at Brookhaven Laboratory [67], TJNAF [68], and Cornell University [57] demonstrated the possibility to obtain a reasonable Q.E. for Sb-based photocathodes at a level of 5-10% and, most importantly, their ability to deliver a high current for a substantial period of time.

For delivery of polarised electrons, GaAs based photocathodes still remain the only choice. So far, maximum demonstrated current of polarised electrons is at the level of 5 mA [69] while the possibility to reach level of 20 mA needs to be investigated. Main parameters of photocathode families principally applicable for PERLE are shown in Table 4.1. It can be seen that if the requirements to the laser for unpolarised beam are modest, the production of polarised electrons demands a yet high laser power. However, this higher laser power leads to thermal desorption resulting in a deterioration of vacuum and reduction of the photocathode lifetime. Cooling down of the photocathode during operation should be taken into account at the gun design.

Material	Typical oper.λ	Work function	Observed Q.E.	Laser power for 20 mA	Observed max current	Obs. lifetime
Sb-based unpolarised	532 nm	1.5-1.9 eV	4-5%	4.7 W at Q.E.=1%	65 mA [Cornell]	Days rep.
GaAs-based polarised	780 nm	1.2 eV at NEA state	0.1-1.0%	31.8 W at Q.E.=0.1%	5-6 mA [JLAB]	Hours

Table 4.1: Characteristics of photocathode materials available for PERLE

4.1.2 Photocathode gun

The main decisive parameter of a DC photocathode gun is its operational voltage. It defines the energy of electrons at the exit of the gun and the 'rigidity of the beam'. This operational voltage also dictates the electric field on the photocathode which defines maximum emission density and, as a result, the beam emittance which may be estimated as

$$\varepsilon_n = \sqrt{\frac{qkT}{2\pi\varepsilon_0 E_c mc^2}}. \tag{4.1}$$

The traditional approach to design guns for ERLs for driving FELs demands that the gun operation voltage should be as high as possible to a reach minimal beam emittance. Maximum operational voltage of 500 kV with a field of 10 MV/m has been demonstrated at the gun developed at JAE for the cERL project at KEK [70]. However, a very high cathode field leads to the risk of field emission, especially from photocathode materials with low work function like GaAs activated to negative electron affinity (NEA) state. As to polarisation, it is worth noting that the field emitted electron 'dissolve' photo-emitted electrons and effectively decrease the polarisation of the beam. A lower voltage is also more convenient for spin manipulation. The optimal values of gun voltage and cathode field should therefore be properly selected at the design stage. A dual operation mode of the gun, at high voltage for unpolarised photocathodes and at low voltage for polarised photocathodes, may not be excluded. Considering these aspects as well as a demonstrated stable operation at other facilities [67, 63, 56], a choice of the maximum operation voltage of 350 kV seems reasonable.

In order to get preliminary estimates required on the drive laser system to deliver beam with parameters required for PERLE, the performance is calculated of a 350 kV gun with
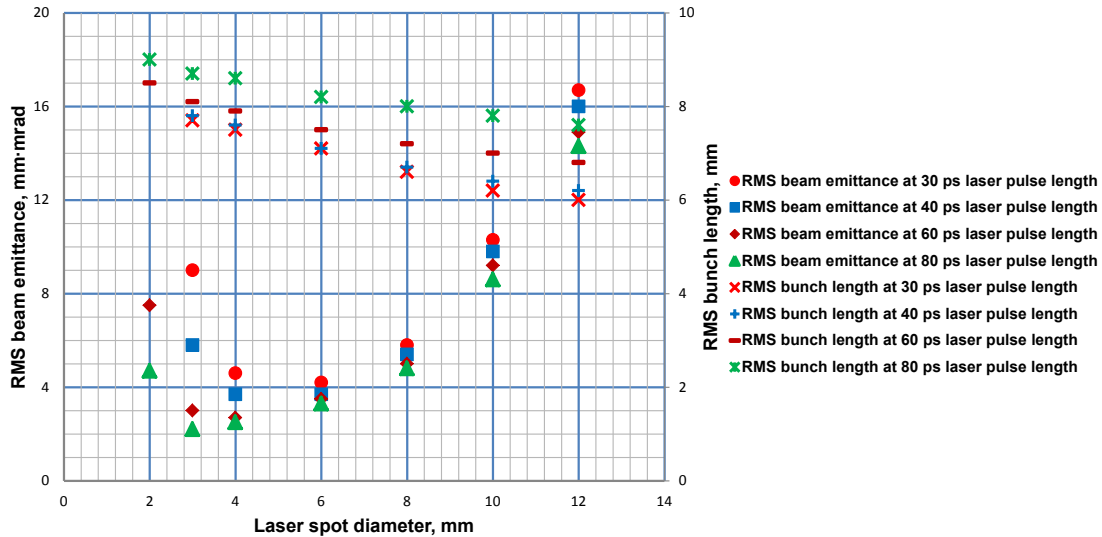
Figure 4.2: Dependence of the calculated normalised RMS emittance and RMS length of 300 pC bunches at the exit of a modified 350 kV JLAB-DL type gun with Cs_3Sb photocathode on laser spot diameter at different laser pulse length.

a JLAB-DL electrode system operating with Cs3Sb photocathode (Fig. 4.2). Simulations have shown that an optimal beam emittance of 2 πmm-mrad can be obtained with illumination of the photocathode with a laser pulse with hat top spatial distribution with a diameter of 3 mm and a flat top laser pulse with a length of 80 ps. The RMS bunch length at 1 m from the photocathode is 8.5 mm (36 ps) which only slightly depends on the laser pulse length.

4.1.3 Buncher and booster

Once emerged from the gun, the electron beam begins to elongate due to the space charge repulsion. To longitudinally compress the bunch to the required 3 mm a compensation energy chirp should be introduced which is typically done with an RF buncher. In order to provide linear energy modulation the frequency of the buncher should be selected to have

bunch flight time at the buncher shorter than $10°$ of its RF phase. For the bunch charge of 320 pC which has an RMS buncher flight time of 36 ps the required frequency should be less than 775 MHz. Further increase of the bunch charge leads to an increase of the bunch flight time and may require even lower buncher frequency. Practically attractive is 400.8 MHz - the first sub-harmonic of the PERLE default frequency. Further gradual beam compression and acceleration can be provided with a booster consisting of a series of single cell 801.6 MHz cavities with individual coupling and control of amplitude and RF phase. As the energy transferred to the beam in the injector booster to reach 5 MeV is 60 kW and is not recovered, the precise number of cavities is defined by the maximum power which may be loaded into a single cavity with the coupler. Assuming that maximum coupler power is 20 kW the booster should consist of at least four cavities. Taking into account that the first two cavities are operated essentially off-crest and at low field as well as a required contingency in case of increasing injector energy, the number of the cavities should be increased to five.

4.1.4 Summary on source and injector

An analysis of the current scientific and technological level of the high average current electron sources for ERLs allows us to conclude that an unpolarised electron source with beam parameters required for PERLE may be built in a relatively short time. This would best be based on a 350 kV DC photocathode gun operated with Sb-based photocathodes followed by a buncher and superconducting booster consisting of five independently fed and controlled RF cavities. A design of a high current polarised electron source requires more investigation but is considered to be a second step for PERLE. A baseline scheme, delivering an average current $2 - 4$ times less than in the unpolarised regime may be realised on the basis of an unpolarised source operating with a family of GaAs photocathodes and reduced DC gun at an operational voltage to 200 kV.

4.2 Cavity Design

PERLE will be a low to medium energy facility in several stages from 150-450-900 MeV for both technology validation and a versatile test bench for high average current applications. This section will outline some key aspects of the linac cavity design and its optimization. Table 4.3 lists the cavity configurations for the three phases of the ERL facility.

4.2.1 Choice of operating frequency

The choice of frequency and gradient is important for any project and depends on a range of factors. It is definitely not a one-size-fits all situation. For large projects, the total cost is dominated by a few competing items such as RF power, cryogenics, structure costs (e.g. modules) and conventional facilities (tunnel, surface buildings, penetrations, etc.). Each of these has a frequency and gradient dependence and depends on the choice of underlying technology assumed. In general the overall cost optimum is a balance between linear costs (such as structure and tunnel) which increase as the gradient is lowered and the machine gets longer, and quadratic terms such as RF power and cryogenic capacity, which increase as the gradient is increased but result in a shorter machine. The result is a rather broad cost minimum allowing some flexibility in the choice of frequency and gradient to accommodate other factors. There are various cost models in use or under development but in general the optimum frequency for this type of machine is somewhere between a few hundred MHz and one GHz. Below this range the structures become very expensive and above this range RF power costs increase. As has been extensively studied in the conceptual design of the LHeC the frequency needs to be significantly below a GHz also for avoiding adverse effects due to beam breakup instability [1]. For compatibility with the LHC, a harmonic of 200 MHz is highly desirable. A frequency of 801.58 MHz is a convenient harmonic[1] that is close to the estimated cost optimum and also compatible with other systems currently in use or under development at CERN [71, 72, 73]. The optimum gradient range is also quite wide, ranging from around 10 to 20 MV/m depending on assumptions about the temperature and Q_0 that can be reliably expected. In general for a large machine the lowest reasonable gradient should be adopted to maximise reliability and minimise the chances of field emission. However, for a small machine like PERLE, at least in the first phase, the cost optimum may favour a higher gradient.

4.2.2 Design considerations

The maximum accelerating gradient is primarily limited by the CW power dissipated on the cavity walls. Due to the quadratic dependence, a medium accelerating gradient with the lowest surface resistance (high Q_0) at moderate to high gradients is required. The

---

[1]Note that 801.58 MHz is the 20th harmonic of the bunch repetition frequency, and, since 20 is not an integer multiple of 3, the bunches of the three re-circulations cannot be equally spaced; this is discussed in more detail in Section 3.4 above.

Parameter	LHeC	PERLE Φ_1	PERLE Φ_2	PERLE Φ_3
Energy [GeV]	60	0.15	0.45	0.90
Cells/Cavity		5		
Gradient [MV/m]		18		
Cav/Cryomodule	4-8	4	4	4
# of Cryomodules/linac	44-22	1	1	2
# of Turns	3	1	3	3
RF Power/cavity [kW]		5-50		

Table 4.2: Design choices for the cavities and cryomodules for the LHeC and different stages of PERLE. The default frequency is chosen to be 801.58 MHz, see text. All stages of PERLE here considered, as well as the LHeC, are configured with two linacs.

number of cells per cavity is a compromise between a reasonable "real estate gradient" while reducing the probability of trapped modes.

The salient feature of an energy recovery linac, at least in CW operation, is the continuous transfer of stored energy from the cavity to the accelerated beam and simultaneously the transfer of (almost equal) energy from the decelerated beam back into the cavity. To first order, the power fed into the cavity through the fundamental power coupler (FPC) from the power source is equal to the power losses in the cavity walls, which can be extremely small. Another formulation of this feature is that the net beam loading at the fundamental frequency is zero in spite of a large beam current. As a consequence, the excitation of HOMs, notably at frequencies where accelerated and decelerated beam currents are not in anti-phase, will be dominating the design.

4.2.2.1 Initial design choices

The choice of five cells per cavity is retained from technical arguments derived in Ref. [73]. The standard parameterisation for elliptical cavities is used [74]. Fig. 4.3 shows the envelope of the scaled five-cell cavity with a large iris aperture diameter of 150 mm, scaled from an existing 704 MHz design.

Detailed parametric scans were carried out to further optimise the aperture choice from the scaled version [75]. Some key RF parameters such as the ratio of B_p/E_p, R/Q, cell-to-
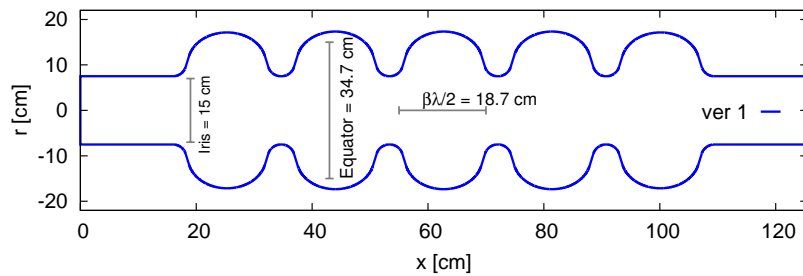
Figure 4.3: Envelope of the first proposal [73] for a five-cell ERL cavity at 802 MHz.

cell coupling for the fundamental and higher order modes, frequency dependence of the fundamental mode and HOMs were studied. A first optimisation aimed at minimising the integrated longitudinal loss factor, which is a measure for the power lost into well-damped HOMs for very short bunches; for a beam current of 40 mA, the 150 mm diameter aperture (version 1) would result in a total HOM power of the order of 35 W.

The geometrical scans performed are used as guidance considering both fundamental mode and HOMs. An increase in aperture to 160 mm from version 1 and adapting the other geometrical parameters leading to an optimum B_p/E_p ratio, is a reasonable choice. This design will be referred to as version 2. An alternative "low-loss" like design was also considered; it is described below in Sect. 4.2.3.

Relevant RF parameters for the mid-cell and five-cell geometries are listed in Table 4.3 and compared to the initial scaled version.

4.2.2.2 Impedance spectra

The longitudinal impedance spectrum calculated in time domain for both versions are shown in Fig. 4.4. This first two to three monopole pass-bands pose the highest impedance and do not easily propagate into the beam pipes requiring targeted HOM couplers to damp

Parameter	Ver 1 (Scaled)	Ver 2
Frequency [MHz]	801.58	801.58
Number of cells	5	5
Active cavity length [mm]	935	935
Voltage [MV]	18.7	18.7
E_p [MV/m]	45.1	48.0
B_p [mT]	95.4	98.3
R/Q [Ω]	430	393
Cell-cell coupling (mid-cell)	4.47%	5.75%
Stored Energy [J]	154	141
Geometry Factor [Ω]	276	283
Field Flatness	97%	96%

Table 4.3: RF parameters of five-cell geometry for version 2 compared to that of the scaled initial version.

them to sufficiently low values. In the transverse plane, see Fig. 4.5, a few passbands of interest with primarily the two first bands (TE_{11} and TM_{11}) being at least an order of magnitude higher than the rest. Similar to the longitudinal plane, transverse impedances at frequencies above 2.8 GHz are significantly smaller in impedance and above the cutoff of the beam tube.

Detailed simulations with loop-like coaxial HOM couplers are underway to determine the level of damping achieved for the lowest order HOMs which pose the highest risk.

4.2.2.3 Loss factors and HOM power

The very small bunch length can excite frequencies well up to 50 GHz or above. This is characterised by the longitudinal loss factor $k_{||}$. Fig. 4.6 shows the frequency dependence of the integrated loss factors for the initial two versions of the cavity.

In addition to HOM damping, the induced HOM power from the short bunches is of the order of 35 W for the nominal bunch charge of 0.32 nC and average beam current of 40 mA, for three passes. This level of power can easily be handled by loop-coupled couplers. However, resonant excitation of a HOM can easily lead to powers in the $1 - 2$ kW range (assuming $R/Q = 50$ Ω and $Q_{ext} = 10^4$). Therefore, the couplers will have to be designed
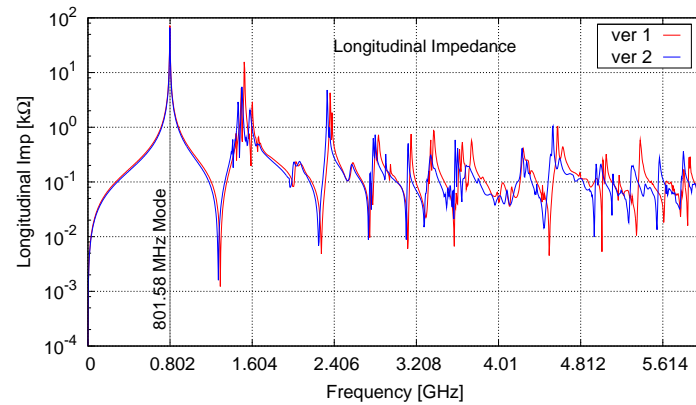
Figure 4.4: The impedance spectra for the longitudinal modes as a function of frequency compared between the initial two versions 1 and 2. The vertical grid shows harmonics of the fundamental mode.
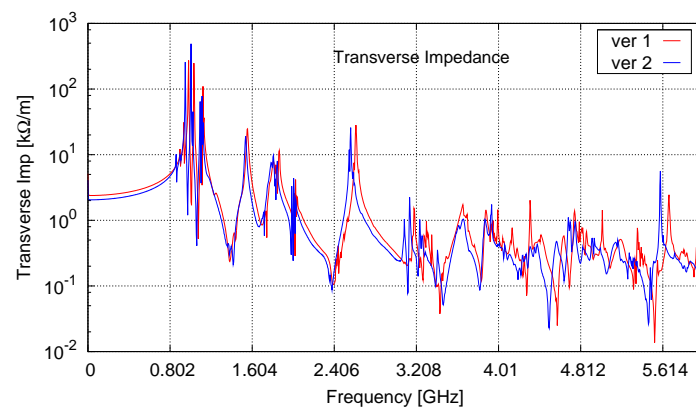

Figure 4.5: Impedance spectra for the transverse modes as a function of frequency compared between the two versions. The vertical grid shows harmonics of the fundamental mode.
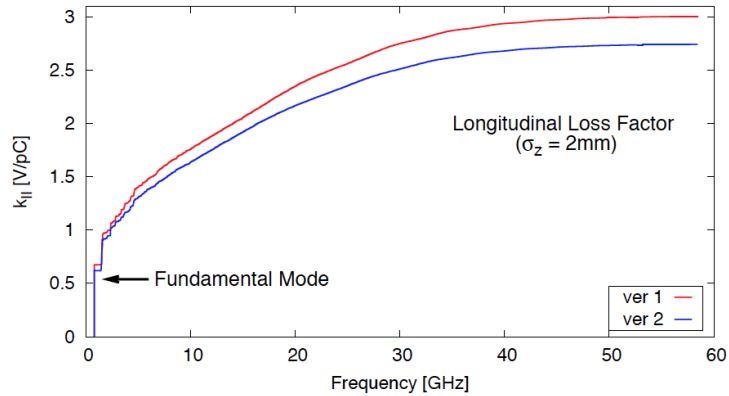
Figure 4.6: Integrated longitudinal loss factor for the two initial versions as a function of frequency, for an assumed bunch length of 2 mm.

to handle this power and impose the condition of HOM impedance to not exceed $500\,\mathrm{k\Omega}$ for the longitudinal modes. For transverse modes, single and multi-bunch simulations have to be carried out to determine the acceptable damping levels. The effect of the transition sections using tapers and bellows is already discussed in Ref. [73].

4.2.2.4 External Q and power requirements

Considering the steady state condition of recirculating beams and energy recovery only, the beam loading can be assumed to be small. Then the input RF power required to maintain the cavity voltage is directly proportional to the peak detuning, see Fig. 4.7.

A realistic $Q_{ext} \sim 10^7$ with a corresponding power of $50\,\mathrm{kW}$ will allow for sufficient margin during transients. At these power levels and frequency range, standard UHF television IOTs become an attractive and robust option.

4.2.3 Cavity optimisation

The cavity cell shape should be carefully optimised to balance accelerating mode efficiency with HOM damping needs (loaded Q's) and HOM power extraction (HOM frequencies relative to the high current lines in the beam spectrum), as well as mechanical and cleaning considerations. Shapes such as the JLab ERL high-current profile [76] and BNL3 ERL [77] cavity are good examples. Starting from these so-called "Low-Loss" shapes, which
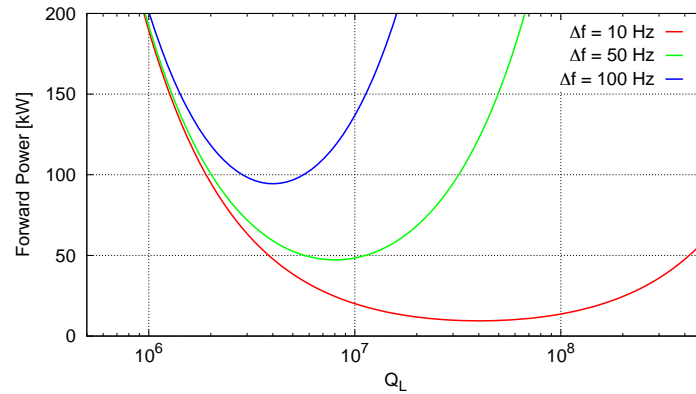
Figure 4.7: Forward power as a function of the loaded Q, for $Q_L \simeq Q_{ext}$, of the cavity for different detunings and zero beam loading.

feature cavity shapes with a steep wall angle down to $0°$, led to the cavity optimisation described here. The low-loss type profile (vertical wall) and contoured irises produce moderate surface magnetic and electric field enhancements normalised to the accelerating gradient; the vertical walls also are the main difference compared to the initial designs with larger inner diameter describe above. This is a one - die design, meaning all the cell cups are produced from the same profile with the end cells simply being trimmed shorter to tune for field flatness.

Extracting HOM power from the cavities to room temperature absorbers must be considered in the cryomodule design (see below). Very effective HOM damping can be achieved by absorbers on the beamline either side of the cavity, providing the beam pipe is sufficiently enlarged to allow the dangerous HOMs to propagate. These, however, consume valuable space and the absorbers must be thermally isolated from the cold beamline components. The JLab waveguide damping scheme [76] avoids this by taking the HOM power out sideways to warm loads but is probably overkill for the LHeC requirements. As already indicated above, loop-coupled HOM dampers, possibly similar to the LHC type mounted on the ends of the cavity close to the end cell, will be sufficient. An example of the implementation of these couplers is described in detail in Sect. 4.3 below. Many other configurations are of course possible. For this type of coupler, the HOM power is removed
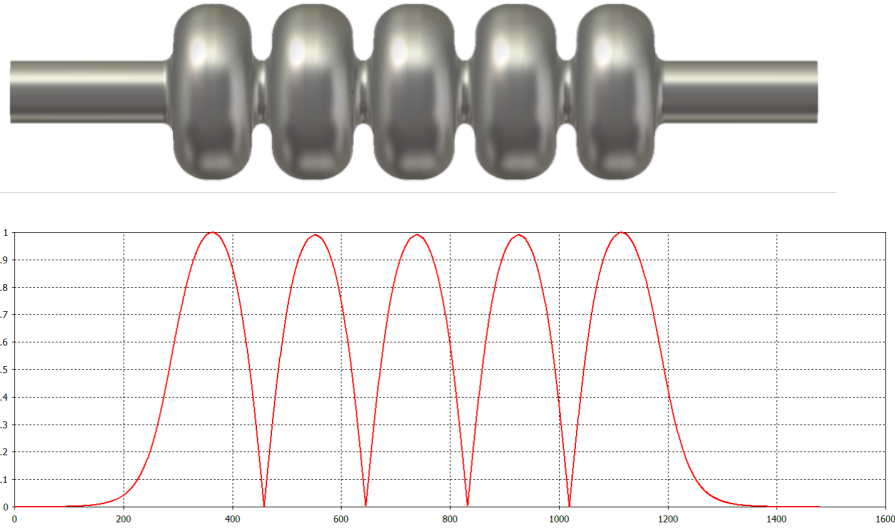
Figure 4.8: Cavity design (single-die, iris ID=tube ID) 801.58 MHz (top); Axial field on axis (bottom).

via a cable to a warm termination. This also allows easy monitoring of the HOM signals for diagnostic purposes.

Fig. 4.8 shows a potential candidate cavity shape optimised for the PERLE and LHeC applications, it uses a median iris diameter (= tube) of 130 mm. The main parameters of the selected shape are listed in Table 4.4, comparing it to a subset of the shapes investigated in this study with iris diameters varying from 115 to 160 mm and limited to solutions with equal iris and tube diameters.

Normalised to λ, the beam tube and iris diameter of the selected solution are slightly larger than the TESLA or CEBAF upgrade (LL) shapes, but smaller than the original CE-BAF (OC) or JLab high-current (HC). This allows good cell-to-cell coupling for HOM damping and reduced sensitivity to fabrication errors, while preserving high shunt impedance for the operating mode for good efficiency. The outer part of the cell profile is tuned to keep harmful HOMs far away from beam harmonics. Figure 4.9 shows the monopole spectrum of the cavity calculated from a long-range wakefield simulation with matched termina-tions on the beam pipes but no other HOM absorbers (similar to Fig. 4.4 above). Note that modes below the beam tube cutoff are unresolved and their final amplitudes and their Q's will depend on the HOM damping configuration, but all modes are well separated from the RF harmonics.

Figure 4.10 shows the dipole spectrum, which is similarly well separated from harm-

Parameter	Unit	Jlab$_1$	Jlab$_2$	CERN$_1$	CERN$_2$
Iris	mm	115	130	150	160
Frequency	MHz	802	802	801.58	801.58
L$_{active}$	mm	922.14	917.911	935	935
$R/Q = V_{eff}^2/(\omega W)$	Ω	583.435	523.956	430	393
Integrated k_{loss}	V/pC	3.198	2.742	2.894	2.626
(R/Q)/cell	Ω	116.687	104.7912	86	78.6
G	Ω	273.2	274.717	276	283
$(R/Q) \cdot G$ /cell	Ω^2	31877	28788	23736	22244
Equator diameter	mm	323.1	328.0	350.2	350.2
Wall angle	degree	0	0	14	12.5
E_{pk}/E_{acc}		2.07	2.26	2.26	2.40
B_{pk}/E_{acc}	$10^{-9}s/m$	4.00	4.20	4.77	4.92
k_{cc}	%	2.14	3.21	4.47	5.75
N^2/k_{cc}		1168	778	559	435
cutoff TE_{11}	GHz	1.53	1.35	1.17	1.10
cutoff TM_{01}	GHz	2.00	1.77	1.53	1.43
E_{acc}	MV/m	20.3	20.4	20.0	20.0
E_{pk}	MV/m	42.0	46.1	45.1	48.0
B_{pk}	mT	81.1	85.5	95.4	98.3

Table 4.4: Parameters of a subset of cavity shapes studied during the cavity optimisation. Each cavity has 5 cells and a nominal effective voltage of 18.7 MV.
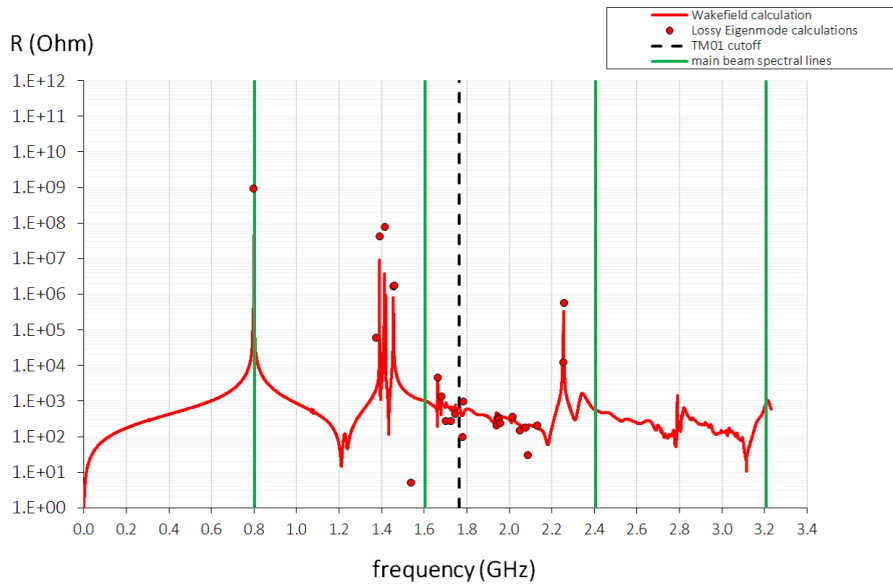
Figure 4.9: Impedance spectrum for the longitudinal modes as a function of frequency of the low-loss cavity design with iris diameter of 130 mm (compare Fig. 4.4).
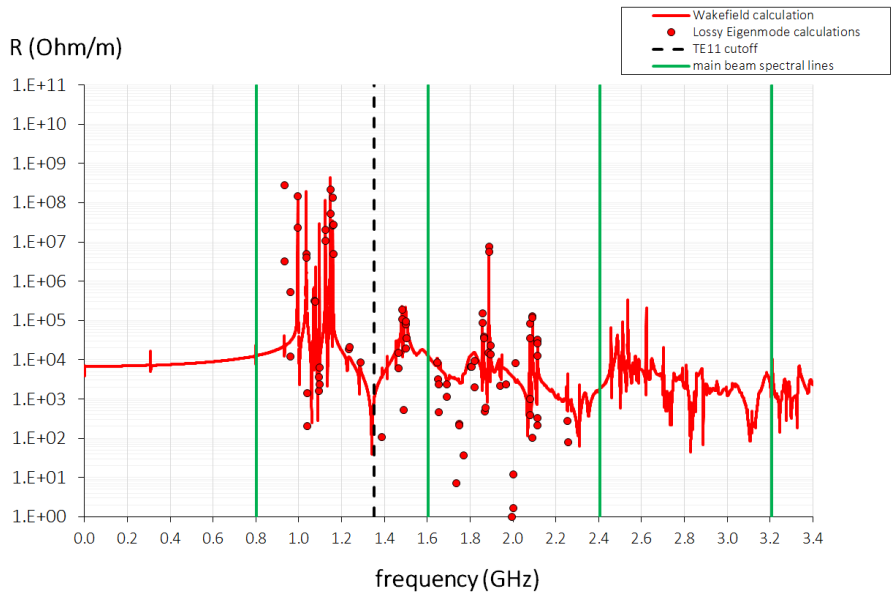

Figure 4.10: The impedance spectrum for the transverse modes as a function of frequency of the low-loss cavity design with iris diameter of 130 mm (compare Fig. 4.5).

ful frequencies. The low-loss type profile (vertical wall) and contoured irises produce moderate surface magnetic and electric field enhancements, normalised to the accelerating gradient. This is a one-die design, meaning all the cell cups are produced from the same profile with the end cells simply being trimmed shorter to tune for field flatness.

4.2.4 Summary on the cavity design

The first scaled version of the 802 MHz ERL cavity was further optimised. Moderate improvement of the HOM performance was obtained with a small increase in aperture with the consequence of about 10% decrease in the fundamental mode R/Q. Given the short bunches and moderately high currents, version 2 (Jlab$_2$ in Tab. 4.4) is considered as a baseline towards realising a first prototype. Detailed studies including the fundamental power coupler and HOM couplers are ongoing to finalise the cavity geometry and the optimum placement of the couplers.

4.3 Cryo Module

PERLE comprises up to four cryo modules each containing four 802 MHz five-cell cavities. A convenient concept for these may be developed by adapting the four-cavity SNS high beta cryo module designed by JLab [78], to accommodate 5-cell β=1 cavities, as is shown in Fig. 4.11. Since the cavities are almost the same length as the original 805 MHz $\beta = 0.81$ 6-cells, no major changes to the module would be required. This design uses a single, large volume helium vessel for each cavity, Fig. 4.12, with the vessels connected by a two-phase pipe to allow gas and liquid to pass freely along the module. No separate gas return or two-phase pipes are needed. At the ends of the module this header is connected to supply and return end cans that contain the bayonet connections, valves, reliefs, etc., Fig. 4.13. The valve boxes are offset from the centerline of the module to accommodate short warm interconnecting sections between the modules for magnets, vacuum pumps, correctors, BPM's etc. Each helium vessel has an end-mounted, Saclay-type tuner [79] and there are bellows between the cavities that minimise mechanical cross talk during tuner operation. On the other end of each cavity, there is a coaxial fundamental power coupler [80] developed from the Tristan design at KEK. The cavities are suspended from a warm space-frame by low conductivity rods. The couplers are at longitudinal fixed points in the support scheme so only have to accommodate radial motion during cool down. This
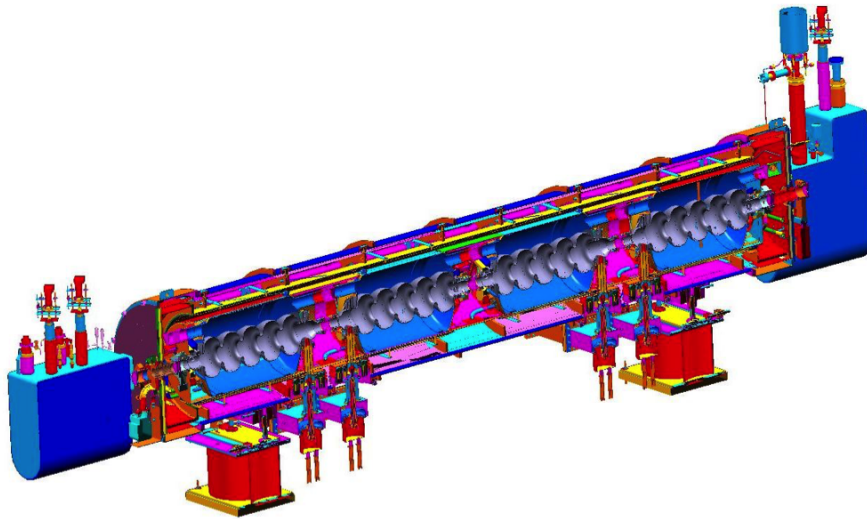
Figure 4.11: SNS high β module adapted to house β =1 5-cell cavities for LHeC.

is achieved with an external warm bellow in the top hat connection. There are no cold bellows or indeed any bellows in the RF section of the coupler. For SNS, the cold part of the outer conductor is trace cooled with counter-flowing helium gas to minimise the heat load to 2 K. This gas flow is controlled by a separate dedicated valve. This active cooling may not be required for LHeC. The module could also be adapted to use an LHC type or other proven coupler.

The helium vessel may be titanium like the SNS modules or stainless steel like the CE-BAF 12 GeV upgrade modules. For Titanium, a NbTi transition piece is used adjacent to the end irises to connect the helium vessel to the cavity and titanium bellows are used. For stainless steel, a Nb to stainless brazed joint can be used and the vessel bellows and piping can all be stainless steel. Care must be taken to avoid introducing permeable or mag-netic material close to the cavity. Fig. 4.12 shows a concept with provision for three such couplers mounted symmetrically on the end group to share the damping duties without in-troducing any dipole perturbation to the cavity mode or any asymmetry between damping of different dipole mode orientations. Many other configurations are of course possible. For this type of coupler the HOM power is removed via a cable to a warm termination, or taken outside the module where it can be monitored for diagnostic purposes.

The measured static loads at 2 K of the SNS type cryo-module were typically less than the 28 W budget, and shield static load was less than the 200 W budget at $\sim$ 50 K (inlet
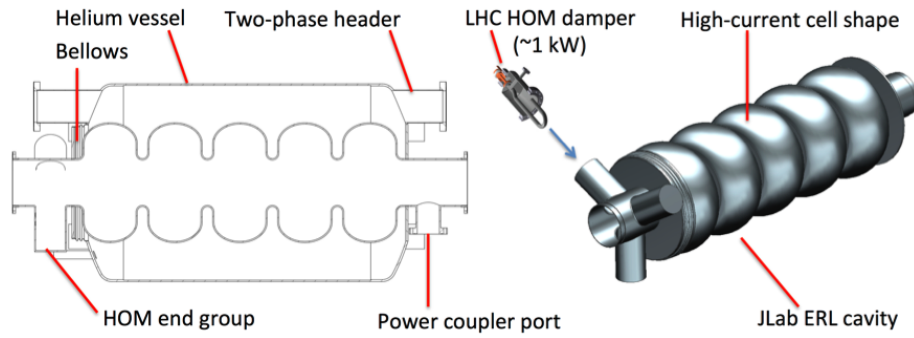
Figure 4.12: Concept for cavity and helium vessel arrangement.
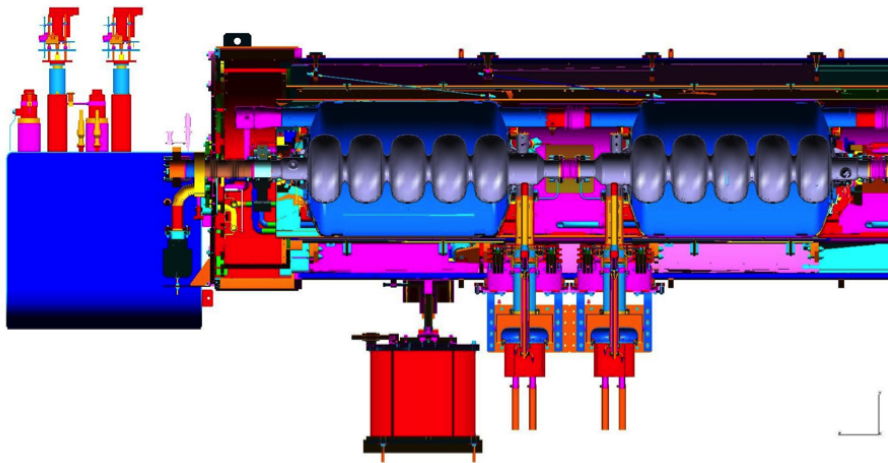
Figure 4.13: Cavity, coupler and end can detail view.
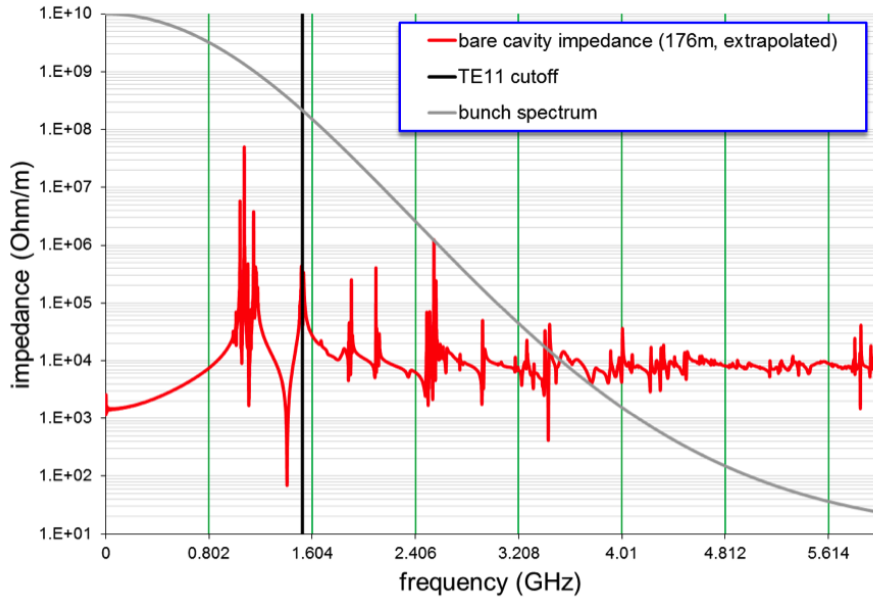
Figure 4.14: Dipole HOM spectrum of the bare cavity. All harmful modes are well separated from RF harmonics. Impedances of modes below cut-off are unresolved and will be determined by the HOM damping configuration.

40 K, outlet up to 80 K). For LHeC the dynamic loads of the CW cavities will be much higher than the pulsed SNS cavities. For standard Nb material at 2 K dynamic heat loads of $30 - 40$ W per cavity at 18.7 MV/m with $Q_0 \sim 2 \cdot 10^{10}$ may be expected. Thus the maximum dynamic load per module may approach 160 W, with total 2 K load less than 190 W. This is well within the capacity of the helium circuit and end cans. Advances in surface treatment such as nitrogen or titanium doping, use of ingot niobium, Nb_3Sn or other improvements may significantly lower this number.

The SNS cryo-module is therefore a convenient model for PERLE and could be adapted with minimal changes to host the new 802 MHz 5-cell $\beta = 1$ cavities. A new concept [81] using many of the design features of this module, as well as attractive features of other JLab designs, is being developed for the JLab Electron Ion Collider [82]. Features of that module might also be considered for an eventual LHeC production cryo-module. A simple cavity design has been developed that is a favourable balance between good HOM properties and good operating efficiency. Further refinement and optimisation of these concepts is expected in the near future.

Figure 4.15: Monopole HOM spectrum of the bare cavity. All harmful modes are well separated from RF harmonics. Impedances of modes below cut-off are unresolved and will be determined by the HOM damping configuration.
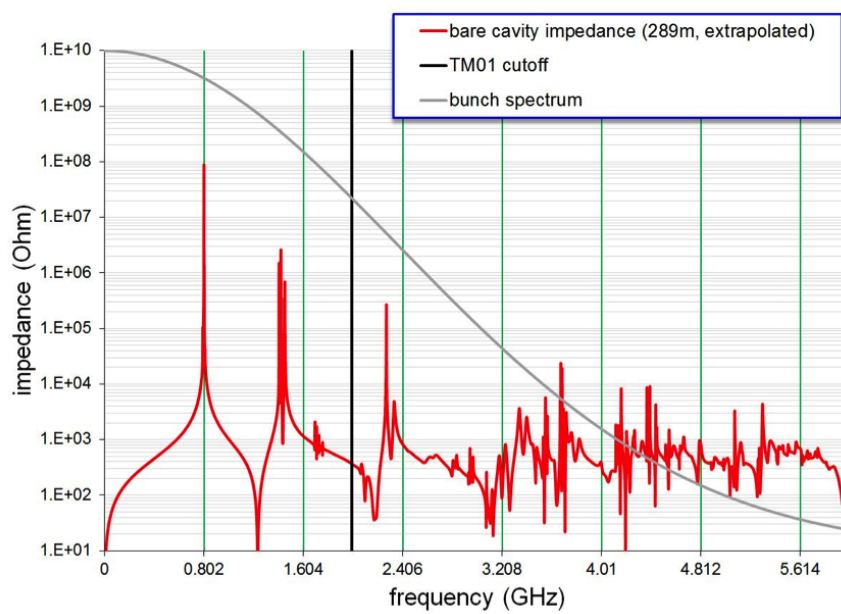
4.4 Arc Magnets

The inventory of the main magnets for PERLE lists:

- 40 bending magnets (vertical field)

- 114 quadrupole magnets

- Bending magnets (horizontal field) in the spreaders and combiners

- Quadrupoles in the spreaders / combiners and in the injection / extraction parts

A sketch of the arcs is given in Figs. 4.18 to 4.23, together with the main characteristics of the bending magnets and quadrupoles. The regions of the spreaders and combiners are not considered here, as these will need a dedicated analysis in view of the limited space available. In all cases, the vertical full gap of the dipoles is taken as 40 mm, and a similar dimension is taken for the horizontal extent of their good field region. Also the quadrupoles feature the same aperture throughout the arcs, which is fixed at 40 mm diameter.

In the lowest energy arcs, i.e. arc 1 and 2, there are four dipoles, with a $45°$ bending angle. The higher energy arcs have on the other hand eight dipoles of $22.5°$ each. Two families of bending magnets are then proposed: one to cover arcs 1 and 2, and another for arcs 3 to 6. The same cross-section could be used for both, though they would differ in terms of length and curvature radius. In both cases a curved construction is assumed, with possibly machined yokes. A tentative cross-section is shown in Fig. 4.16. An H type yoke is proposed, rather narrow in the vertical direction, to minimize the vertical distance between the arcs. The dimensions could be further reduced – in particular horizontally – after an iteration on the required field quality. The coils will need to be designed as part of an overall optimization, including the power converters. The shaded area in Fig. 4.16 refers to 6-7 A/mm^2 of current density at the maximum field of 1.31 T of arc 6.

While the dipole strenghts simply scale across the arcs, this is not the case for the quadrupoles, as each arc has a different optics. Table 4.5 summarizes the maximum and minimum integrated gradients as well as pole tip fields for the quadrupoles. This is based on the two lengths – 200 and 300 mm – currently specified in the lattice, as in Figs. 4.18 to 4.23. This results in a quite wide range of integrated gradients and pole tip fields. More-over, some quadrupoles are rather weak. This prompts an iteration with the optics, which needed to be refined after a full design of the bending magnets including the edge effects. The possibility of making families, grouping by gradient or length or both, would need to

be considered. Two preliminary cross-sections are shown in Fig. 4.17. Since the aperture is the same throughout the arcs, an option could be to keep the same iron design, though to have only 2 instead of 4 coils for the weaker quadrupoles. The impact of this asymmetry on the field uniformity is rather minor, about $2 \cdot 10^{-4}$ at 2/3 radius on the skew octupole in 2D. As for the main bending units, the coils could be water cooled (for compactness) and they will need to be designed as part of the overall optimization, including the power converters, the magnet manufacturing cost and the operational scenarios, considering for example different baseline optics. The shaded area in Fig. 4.17 corresponds to 7-8 A/mm^2 of current density at maximum gradient. More exotic designs – for example a flat quadrupole with an open magnetic circuit – could, if needed, provide a more compact design in the vertical direction, though the stray field would need to be properly addressed.

	$|GL|_{max}$	$|GL|_{min}$	$|B_{pole}|_{max}$	$|B_{pole}|_{min}$
arc 1	0.76	0.12	0.076	0.012
arc 2	1.00	0.01	0.100	0.001
arc 3	1.80	0.23	0.172	0.016
arc 4	2.94	0.61	0.294	0.041
arc 5	2.99	0.71	0.200	0.047
arc 6	3.26	0.47	0.217	0.031

Table 4.5: Summary of integrated gradients and pole tip fields of quadrupoles, in T.

A further analysis will address in detail the magnets in the spreaders and combiners regions. Furthermore, a set of vertical / horizontal dipole correctors will most likely need to be added. According to their strength and field uniformity tolerances, these correctors could be combined with some of the quadrupoles in a hybrid design. Path length adjustments, mainly from seasonal contraction and expansion effects, amounting to an expected $O(1)$ cm correction, may be addressed via dog legs in the arcs. Finally, multiple aperture magnets could be analyzed as part of an overall cost optimization, though much could depend on the staged construction of the facility.
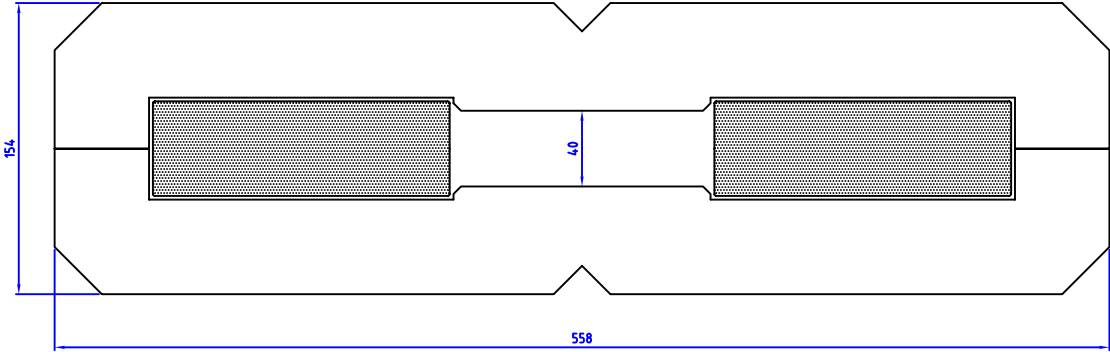
Figure 4.16: Preliminary cross-section of bending magnets.
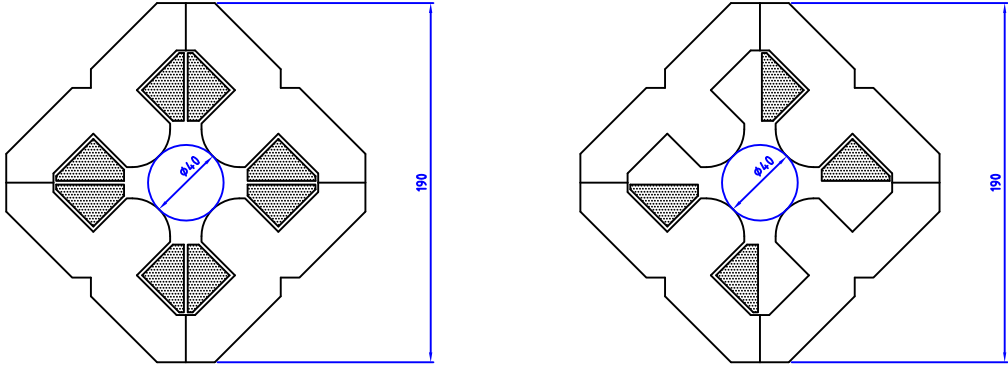
Figure 4.17: Preliminary cross-section of quadrupole magnets.

bending magnets			
type	count	B [T]	L [mm]
bA1	4	0.57	718

quadrupoles			
type	count	G [T/m]	L [mm]
q4S1	2	3.79	200
q5S1	2	−0.61	200
q6S1	2	1.05	200
q7S1	2	−0.93	200
q1A1	2	−0.66	300
q2A1	2	1.85	300
q3A1	2	−1.05	300
q4A1	1	2.09	300
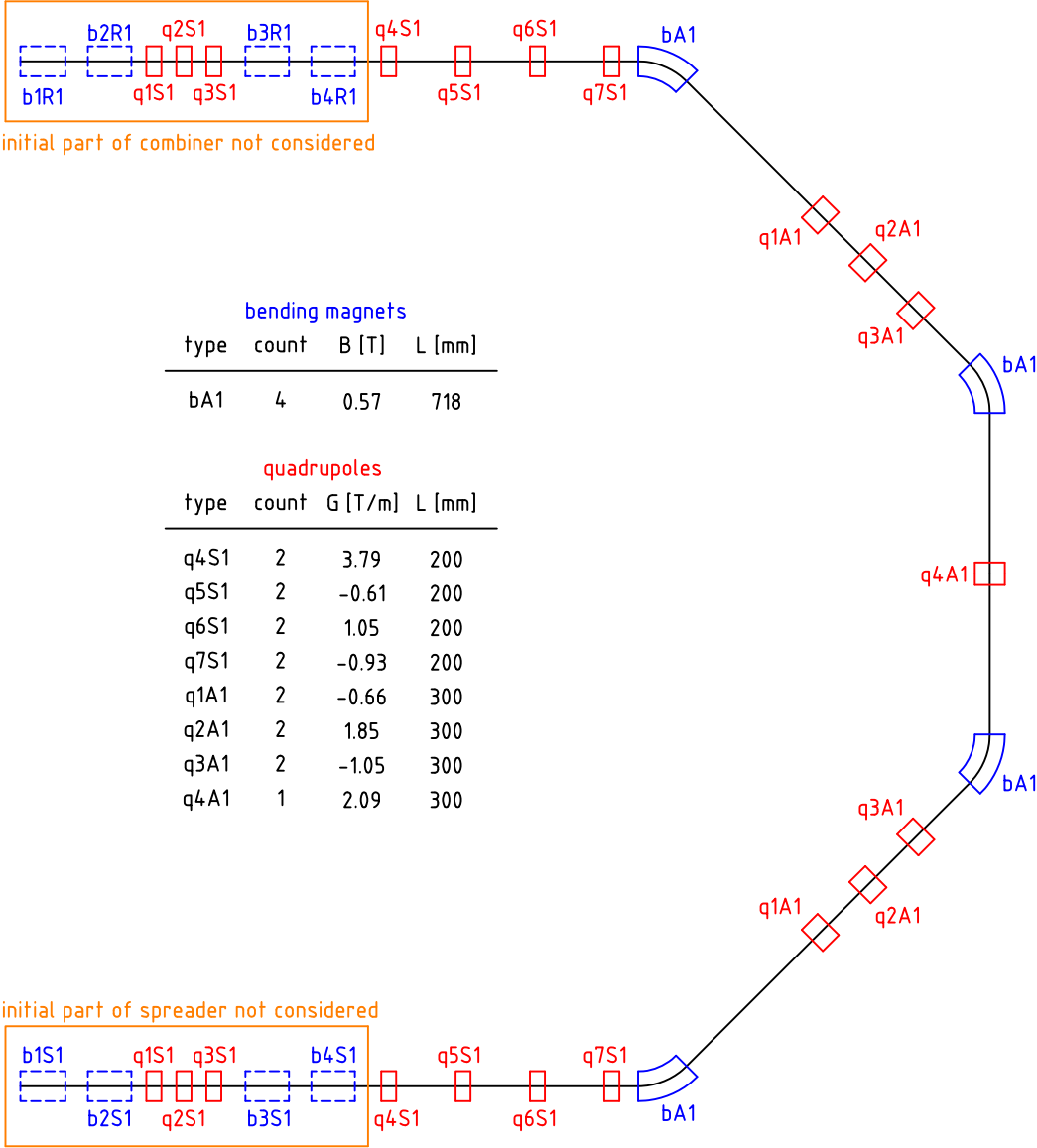
Figure 4.18: Arc 1 and main magnets, where *b* denotes bending and *q* quadrupole magnets.

bending magnets

type	count	B [T]	L [mm]
bA2	4	1.11	718

quadrupoles

type	count	G [T/m]	L [mm]
q4S2	2	4.99	200
q5S2	2	−0.07	200
q6S2	2	−2.51	200
q7S2	2	−0.75	200
q1A2	2	3.27	300
q2A2	2	−3.05	300
q3A2	2	0.21	300
q4A2	1	1.25	300
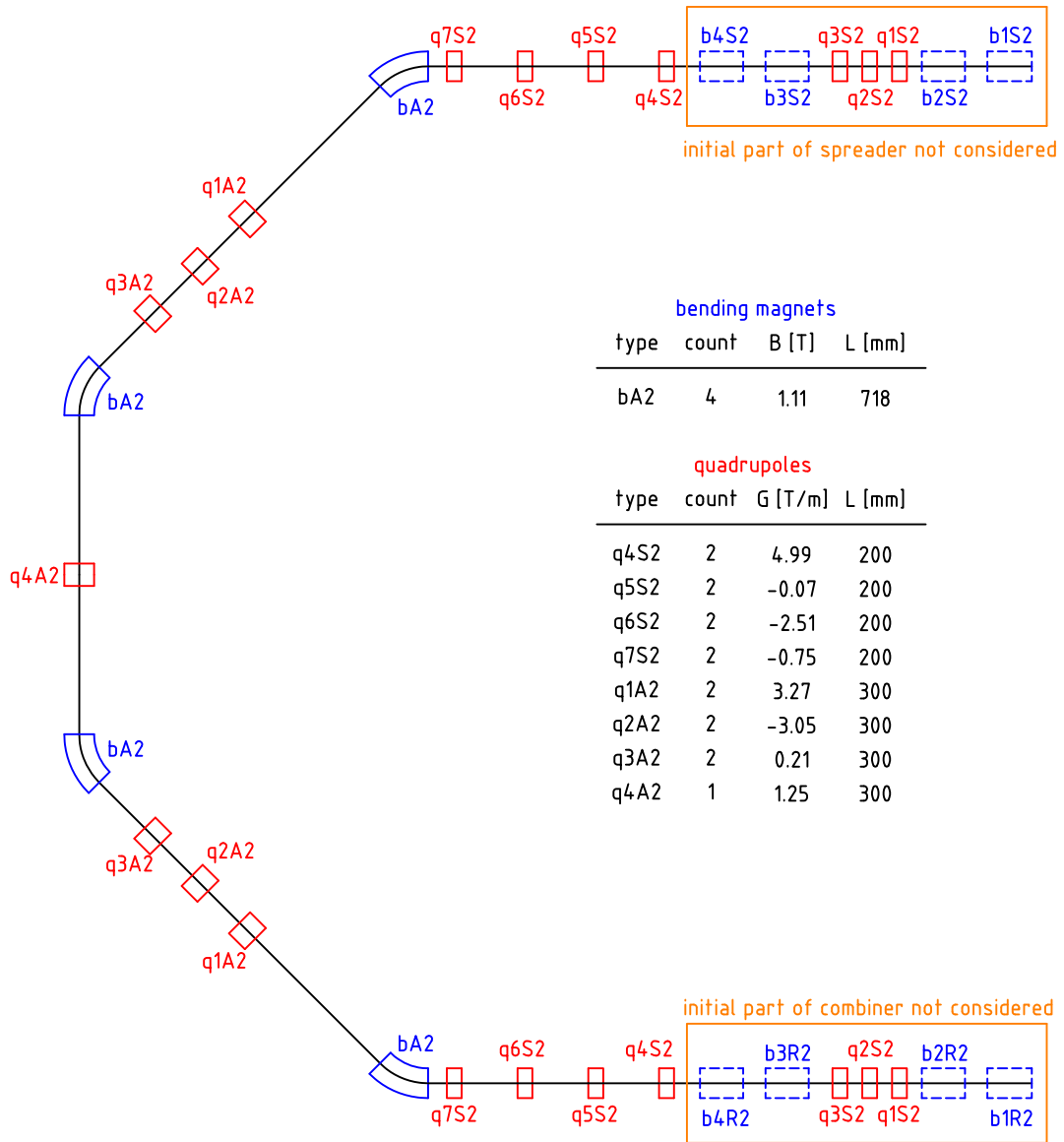
Figure 4.19: Arc 2 and main magnets.

bending magnets

type	count	B [T]	L [mm]
bA3	8	0.66	906

quadrupoles

type	count	G [T/m]	L [mm]
q4S3	2	−5.81	200
q5S3	2	8.61	200
q6S3	2	2.27	200
q7S3	2	−7.86	200
q1A3	2	−3.80	300
q2A3	2	6.01	300
q3A3	2	−3.36	300
q4A3	1	0.78	300
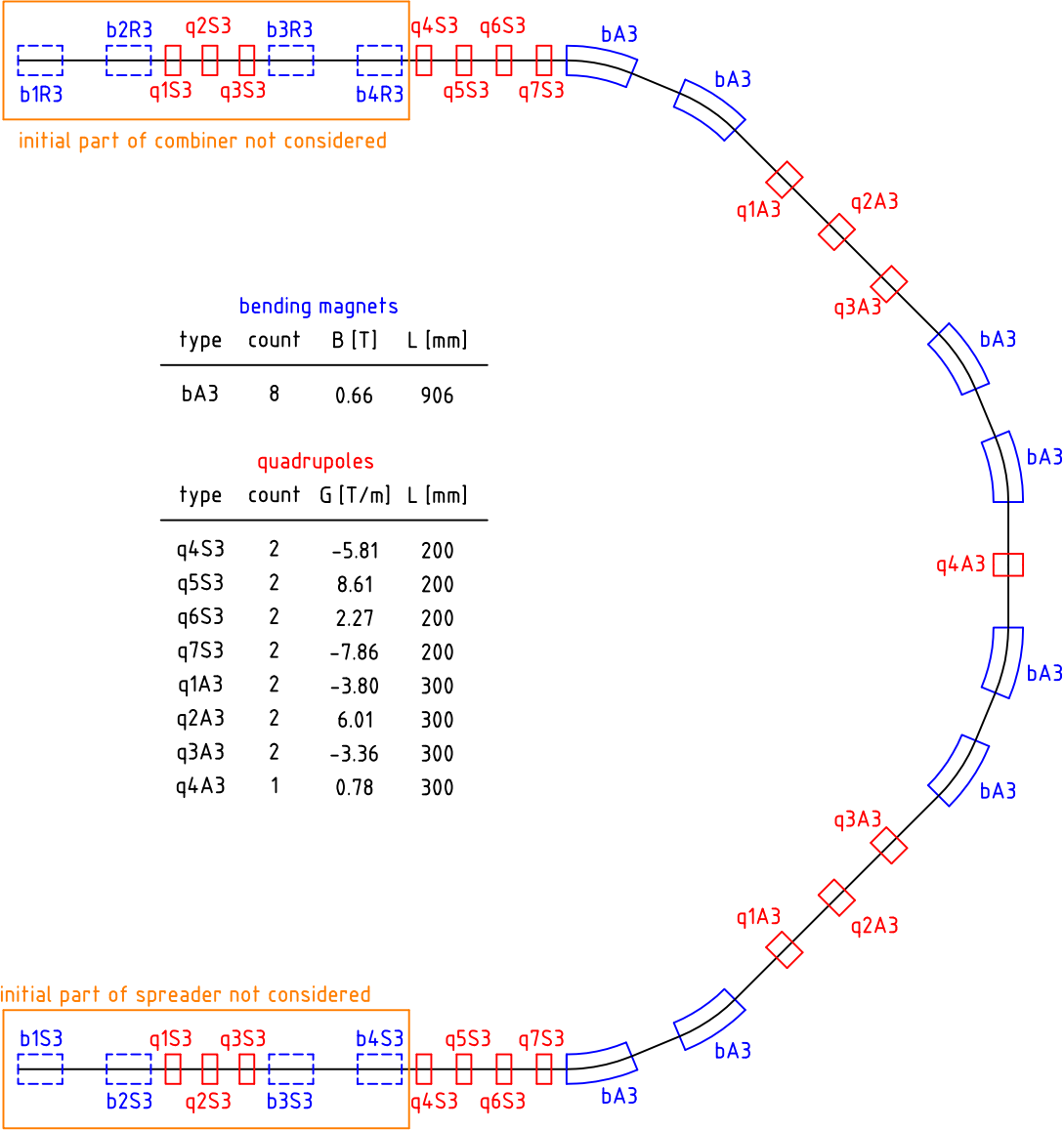
Figure 4.20: Arc 3 and main magnets.

bending magnets

type	count	B [T]	L [mm]
bA4	8	0.88	906

quadrupoles

type	count	G [T/m]	L [mm]
q4S4	2	-10.27	200
q5S4	2	14.68	200
q6S4	2	-6.25	200
q7S4	2	-14.53	200
q1A4	2	-6.14	300
q2A4	2	7.63	300
q3A4	2	-2.04	300
q4A4	1	3.11	300
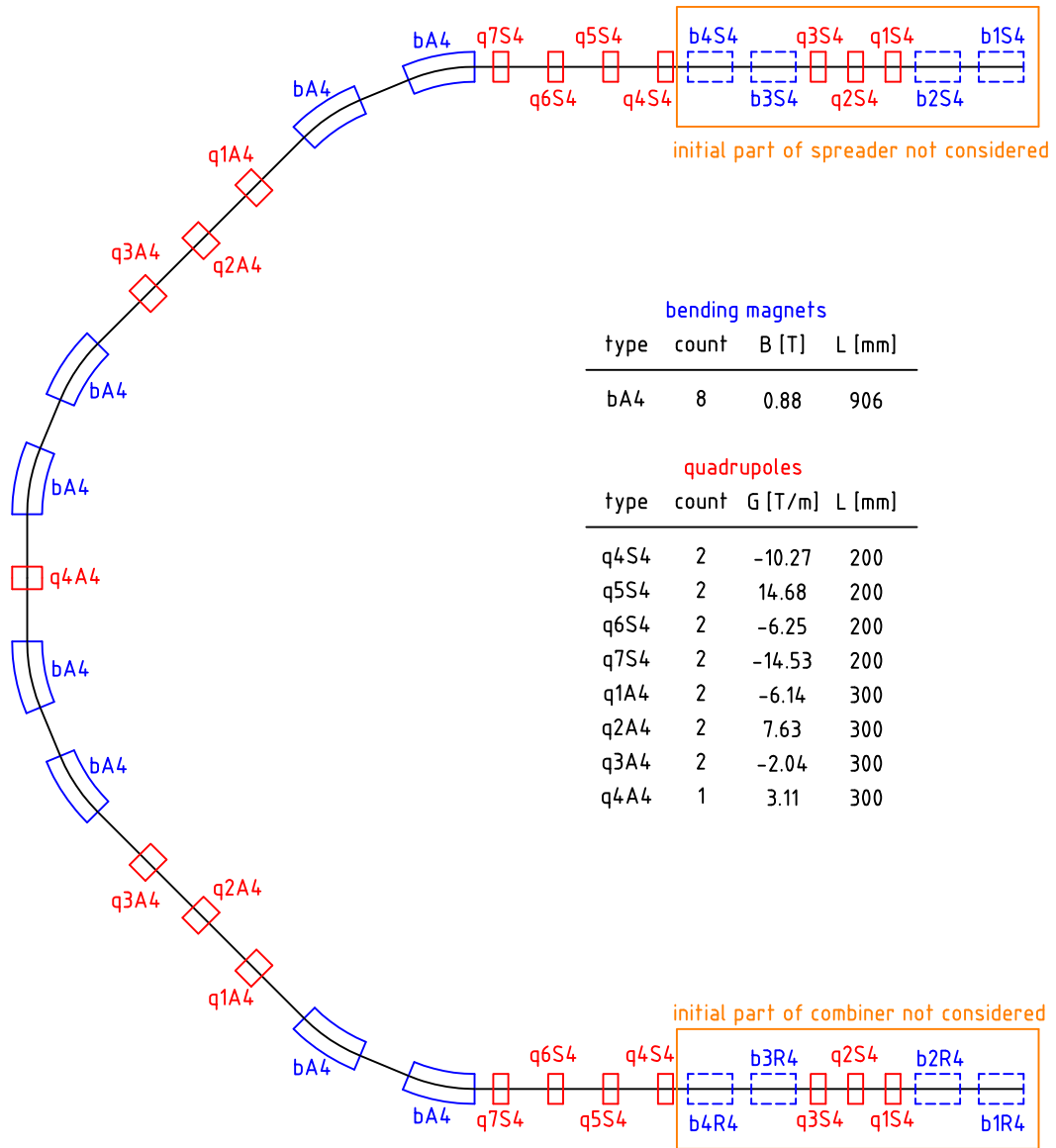
Figure 4.21: Arc 4 and main magnets.

b2R5
b1R5   b3R5
initial part of combiner
not considered

q1S5   q3S5
q2S5   q4S5
bA5
bA5
q1A5   q2A5
q3A5
bA5
bA5
q4A5
bA5
bA5
q3A5
q1A5   q2A5
bA5
bA5

initial part of spreader
not considered
b1S5   b3S5
b2S5   q1S5   q3S5
q2S5   q4S5
bA5
bA5

bending magnets

type	count	B [T]	L [mm]
bA5	8	1.09	906

quadrupoles

type	count	G [T/m]	L [mm]
q1S5	2	−4.46	300
q2S5	2	9.98	300
q3S5	2	−7.13	300
q4S5	2	6.53	300
q1A5	2	−6.58	300
q2A5	2	9.13	300
q3A5	2	−2.36	300
q4A5	1	2.92	300

Figure 4.22: Arc 5 and main magnets.

q1S6   b2S6
q4S6   q3S6   q2S6   b3S6   b1S6

initial part of spreader
not considered

bA6   bA6

q2A6   q1A6

q3A6

bA6

bA6

q4A6

bA6

bA6

q3A6

q2A6   q1A6

bA6

bA6

q4S6   q2S6

q3S6   q1S6   b2R6

initial part of combiner
not considered

b3R6   b1R6

bending magnets			
type	count	B [T]	L [mm]
bA6	8	1.31	906

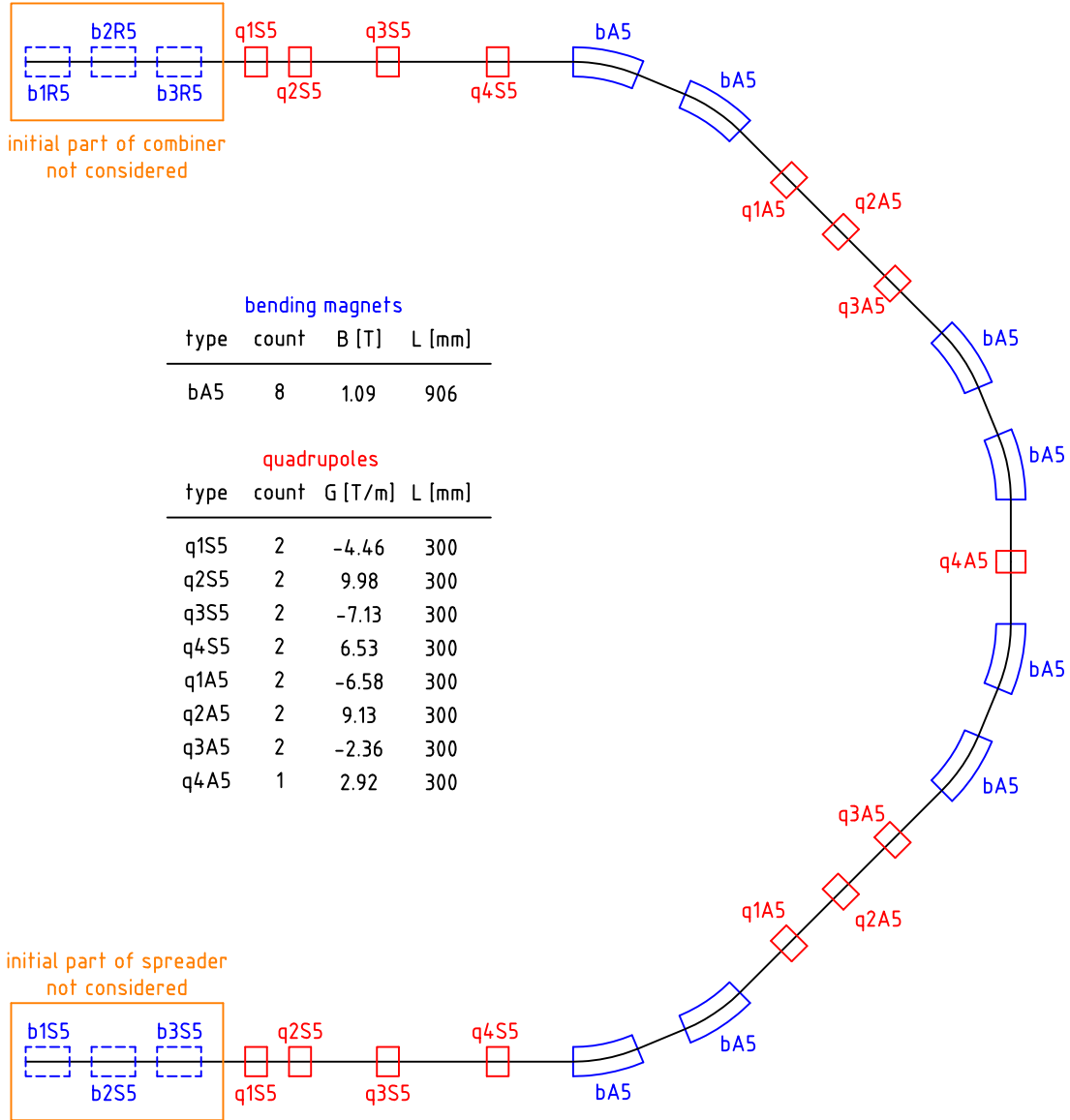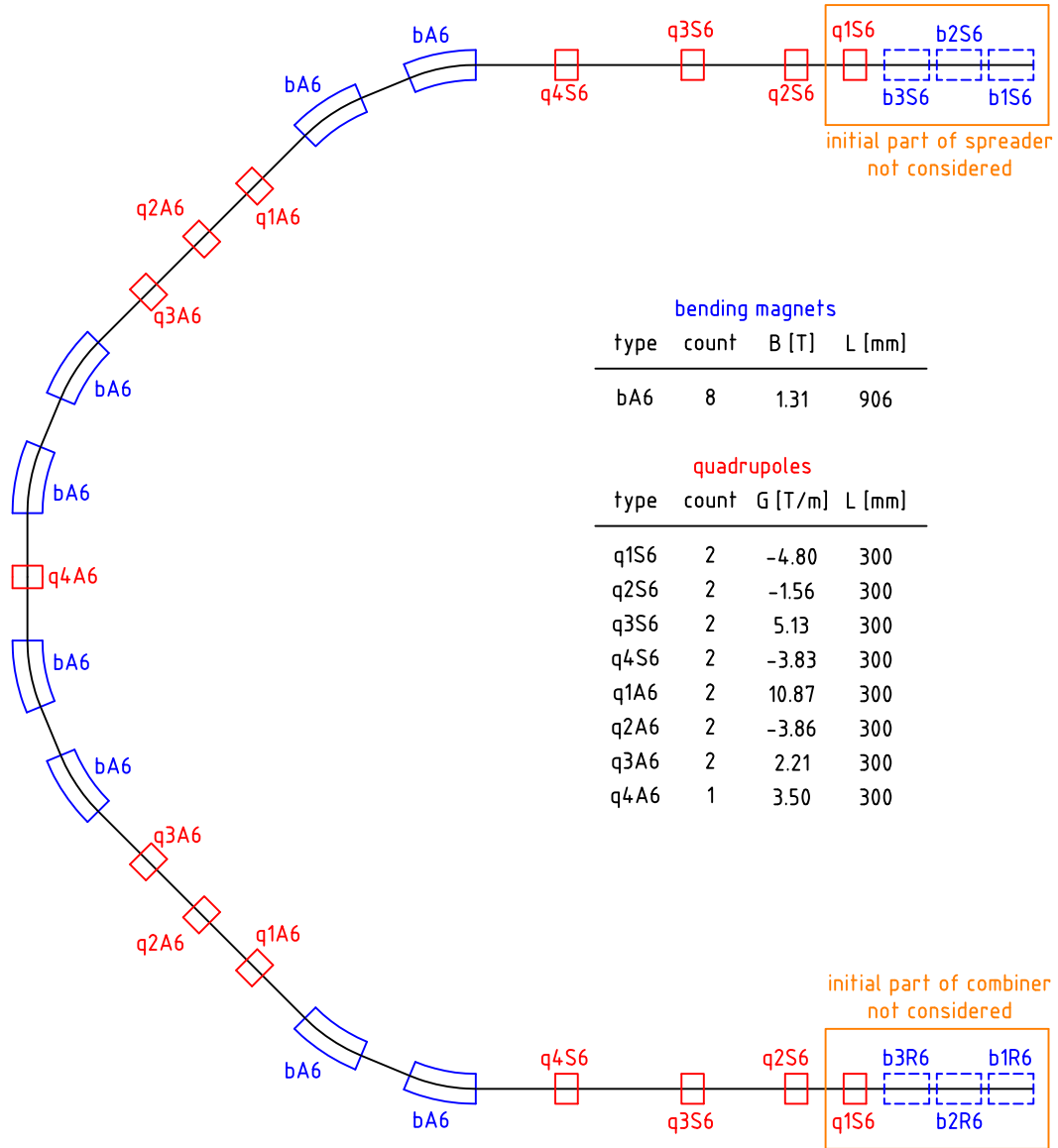| quadrupoles			
type	count	G [T/m]	L [mm]
q1S6	2	−4.80	300
q2S6	2	−1.56	300
q3S6	2	5.13	300
q4S6	2	−3.83	300
q1A6	2	10.87	300
q2A6	2	−3.86	300
q3A6	2	2.21	300
q4A6	1	3.50	300

Figure 4.23: Arc 6 and main magnets.

4.5 Dumps and Transfers

The nominal operation of PERLE foresees to continuously dump the decelerated 5 MeV electron beam; this corresponds, for a current of 12.8 mA, to a constant power deposition of 64 kW on the beam dump. The possibility of dumping the beams at all the different energies during the setup period is considered. In this case a system of Transfer Lines (TL) and a beam dump has to installed at the end of each Linac as shown in Figure 4.24.
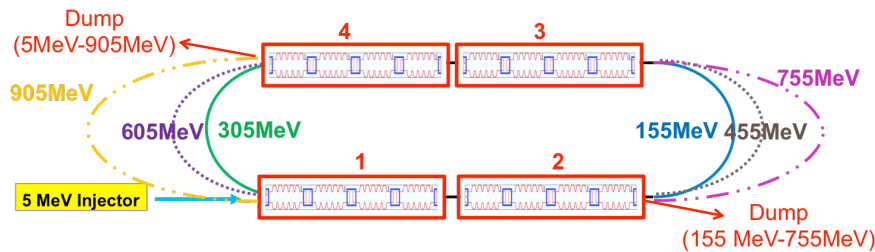

Figure 4.24: Top view of PERLE and the transfer lines-to dump systems for nominal operation and beam setup at the different energies.

4.5.1 Operational dump

Two options are investigated for the operational beam dump. In the first case no additional magnet has to be installed in the main lattice. A 0.66 m long dipole (SBEND) with a 0.906 T magnetic field acts as a spectrometer and separates vertically the different energy beams to direct them towards the respective superimposed arc (Fig. 4.25).

This magnet can be used to deflect the 5 MeV beam towards a vertical beam dump as shown in Fig. 4.26. A C-shaped dipole has to be used to host a T-shaped vacuum chamber. The 5 MeV beam gets a deflection of about $90°$ in 3 cm and is extracted from the magnetic field region. Due to the strong edge effects and the low energy, the beam size increases rapidly and the 3 σ envelope has a radius of 65 mm (for a normalised emittance of 10 mm mrad) at a height of 10 cm from the Linac axis; here the vertical dump has to be installed (Fig. 4.26). Due to the low energy no window can be installed at the entrance of the dump system. The beam continues diverging in vacuum before hitting the dump material. A low Z material, like Carbon, can be used to limit the backscattering and the weight of the dump block which has to have a size of indicatively 0.4 m $\times$ 0.1 m$\times$ 0.1 m (length, width and thickness respectively). For an incident energy of 5 MeV, about 1-1.5% of the
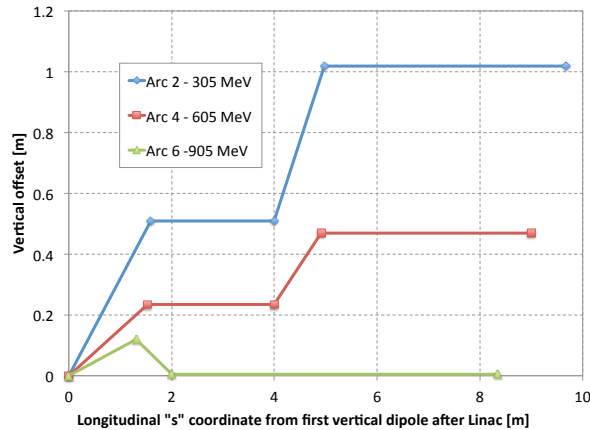
Figure 4.25: Schematic view of the vertical spreader which directs the 305 MeV, 605 MeV and 905 MeV beams towards the respective superimposed arc.

electrons are scattered back from Carbon. The corresponding fraction of energy (or power) which is backscattered is a bit less as the electrons deposit part of their energy before being scattered back. For a 64 kW electron beam one can estimate roughly 0.6 kW backscattered from the Carbon dump. To further reduce the backscattering towards the recirculating beam, a thin layer of a heavier material should be installed at the entrance of the dump, provided that a free hole is left for the passage of the beam. Detailed studies are needed to assess the feasibility of the proposed design (including a cooling system and additional shielding), evaluate potential integration conflicts (especially for the replacement of the underneath dipole) and the real impact of the backscattering on the recirculaitng beam quality. Moreover detailed tracking studies in a real 3D field have to be performed to check the effect of the strong fringe fields on the electron beam.

The second option foresees the installation of three additional small dipoles in the 1.42 m drift between the end of the Linac and the start of the vertical spreader (k1, k2 and k3 in Fig. 4.27). The first dipole has a magnetic length of 0.2 m, a magnetic field of 0.044 T and kicks the 5 MeV beam by $30°$ to extract it horizontally towards the beam dump. After a 5 m drift line the beam is dumped against a cylinder of graphite (20 cm radius and 10 cm long). Also in this case a cooling system and a surrounding shielding have to be foreseen. A clearance of 2 m is obtained between the main lattice and the shielding assuming a shielding transverse size of 1 m. Since k1 is operated in DC mode, all the beams are slightly affected by its magnetic field. The two remaining magnets are thus used to bring the other energy beams back on to the reference trajectory before the vertical spreader
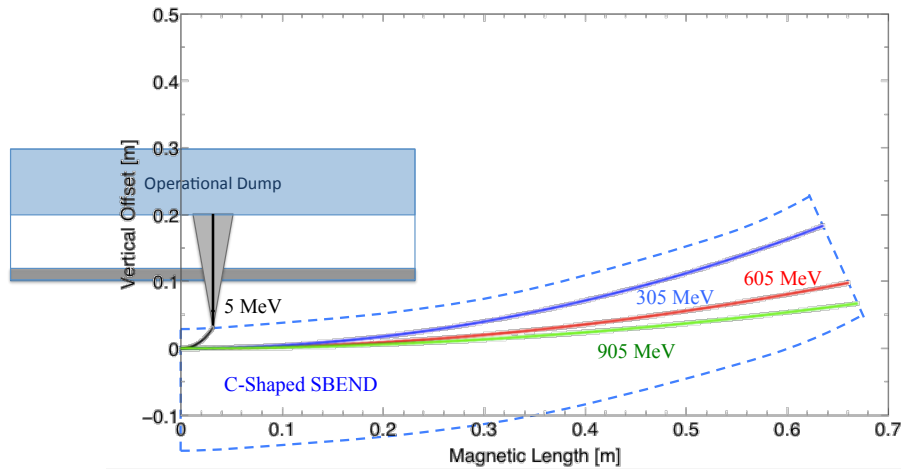
Figure 4.26: The first dipole of the vertical spreader is a C-Shaped SBEND which allows to extract the 5 MeV beam from the magnetic field region (between the dashed blue lines) towards the vertical dump.

(Fig. 4.28). All three magnets have the same magnetic length, and the magnetic field is 0.088 T (with opposite polarity) and 0.044 T for k2 and k3 respectively. Preliminary studies were performed to check the impact of the proposed bump on the optics. The horizontal dispersion can be closed to $1.6 \cdot 10^{-7}$ m while the β functions at the entrance of the first dipole of the vertical spreader differ by 15 % with respect the nominal optics; no further optimisation was attempted.

4.5.2 Setup dumps

During the commissioning period of PERLE, and in general during the beam setup, it is important to be able to dump the beam at the different energies. The easiest solution is to keep switched off the first horizontal dipole of the arc corresponding to the energy of interest and let the beam go straight towards the dump (Fig. 4.27). This dipole has to have a C-shape to allow the installation of a Y chamber for the recirculating and the extracted beam. The minimum bending angle of 22.5° guarantees enough clearance between the next dipole and the vacuum chamber of the extracted beam. If the dipoles of the arc are powered in series they can all be switched off during the setup period. Also in this case the line to the dump, one per each energy, corresponds to a 5 m drift. The β function at the dump is about 50 m corresponding to a minimum beam size for the most energetic beam of 238 μm. In order to limit the energy deposition and the activation of the dump
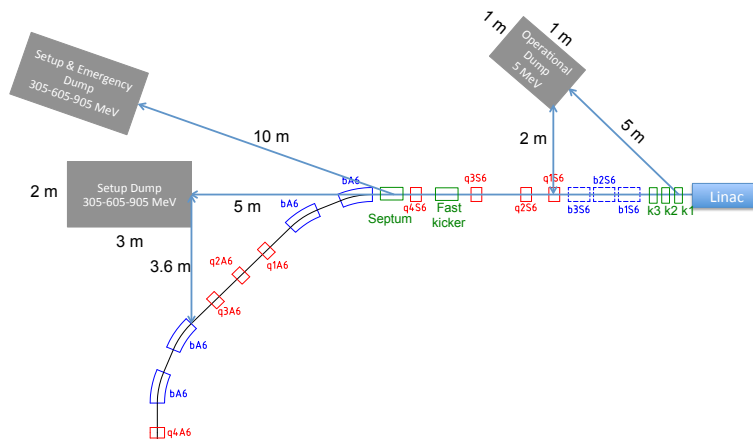
Figure 4.27: The transfer lines to the operational, setup and setup&emergency beam dumps are shown with respect to the 905 MeV beam arc.

materials, the setup should be performed with a reduced intensity. In Table 4.6, the current corresponding to a power deposition of 64 kW at the different energies is shown.

Energy [MeV]	Current [mA]	electrons per bunch/10^7
5	12.8	200
155	0.41	6.5
305	0.21	3.3
455	0.14	2.2
605	0.11	1.7
755	0.08	1.3
905	0.07	1.1

Table 4.6: Current and number of electrons per bunch (25 ns bunch spacing) corresponding to a constant power deposition at the beam dump of 64 kW for the different energies of PERLE and assuming an initial current of 12.8 mA.

The dump system will consist of three superimposed blocks of graphite with a radius of 20 cm and a maximum length of 1.2 m (for the 950 MeV beam) to absorb also the secondary showers. Additional shielding has to be envisaged and a total occupancy of 2 m×3 m has to be considered around the dump blocks.
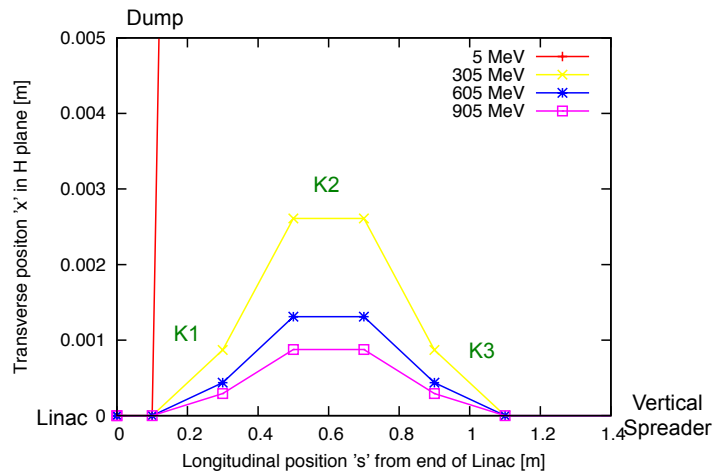
Figure 4.28: Horizontal trajectory of the different energy beams before the vertical spreader. The 5 MeV beam is extracted to the dump while the other beams are brought back to the reference trajectory. The bump and the dump are directed towards the outside of the ERL facility.

4.5.3 Emergency dumps

Up to now only DC magnets have been considered. In the eventuality that the setup dumps have to be also used as emergency dumps, fast kickers have to be included in the lattice. The CW operation mode and the 25 ns bunch spacing require a rise time $t_m = 23$ ns to allow for some jitter. A system impedance Z of 25 Ω is assumed, and a rather conservative system voltage U of 60 kV. Assuming a full horizontal and vertical opening of 40 mm, the magnetic length of the fast kickers has to be 0.46 m and the gap field 0.038 T. One extraction system per each each energy has to be installed after the vertical spreader when the beams are fully separated. Preliminary studies were carried out only for the 905 MeV beam but analogous considerations hold for the other energies. A fast horizontal kicker is installed between the last two quadrupoles before the arc (q3S6 and q4S6 in Fig. 4.27). The beam is deflected outwards by the kicker and goes through the 40 mm diameter of the defocusing quadrupole (q4S6) getting an additional kick. A horizontal Lambertson septum, placed 0.5 m before the first arc dipole (ba6), extracts the beam towards the dump line (Fig. 4.29). A clearance of 6 mm between the recirculating and the extracted beam envelope is obtained at the septum with the proposed configuration. The ba6 dipole has to be C-shaped (the present H-shaped design and the size of the magnet are not compatible with a fast extraction system due to the limited available space in the lattice) and the
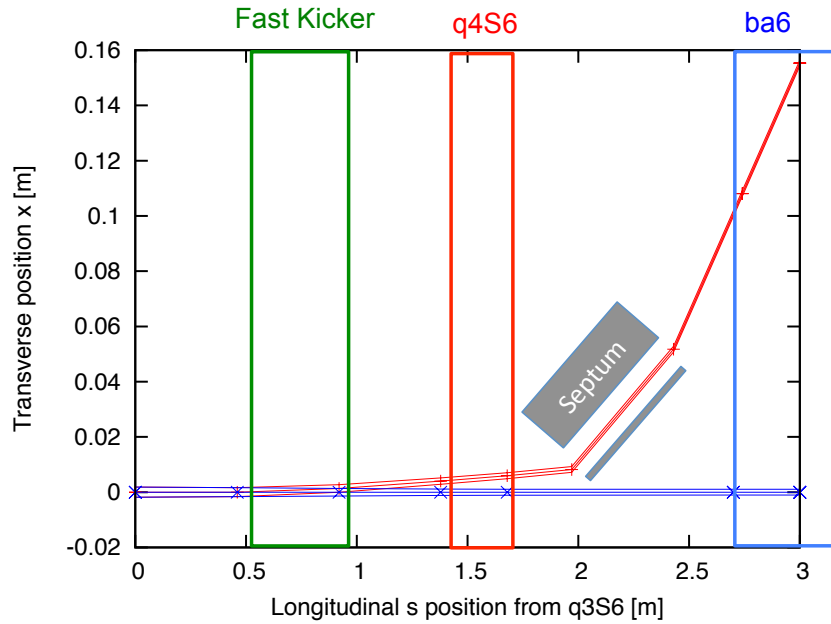
Figure 4.29: Fast extraction system for the emergency dump of the 905 MeV beam

magnetic field free region is assumed to start at 70 mm from the main axis. Additional 30 mm are considered for the beam pipe of the extracted beam. A 0.5 m long septum with a 1.1 T magnetic field provides a kick of 174 mrad and thus an offset of 108 mm at the ba6, in agreement with the specifications.

In order to limit the energy deposition at the emergency dumps, the interlock system has to stop the injector and pulse the kickers of all the different arcs simultaneously. This limits the maximum number of dumped bunches to 7 (bunches contained in one arc and one Linac). A kicker flattop of 166 ns is needed to fit all the bunches in and a fall time of 23 ns is assumed.

The energy and power deposition at the dumps for different energies are summarised in Tab. 4.7. The transfer lines to the dump have to be ~10 m long and a defocusing quadrupole has to be installed at ~4 m in order to increase the beam size at the dump and reduce the energy density (for the 905 MeV beam, a 0.6 mm × 0.4 mm beam size can be achieved using a quadrupole identical to q4S6). A block of superimposed kickers can be envisaged to align vertically the different energy beams at the dumps and reduce the transverse occupancy of the dump/shielding block.

Energy [MeV]	Energy deposition [J]	Power deposition [MW]
155	0.35	2.09
305	0.68	4.12
455	1.02	6.14
605	1.36	8.16
755	1.69	10.2
905	2.03	12.2

Table 4.7: Energy and power deposition when dumping seven bunches of $2 \cdot 10^9$ electrons on the emergency dumps.

4.5.4 Test facility

The possibility of using the PERLE transfer lines to perform quench and damage tests of superconducting magnets and cables is explored. The fast extraction system of the emergency dumps is used to extract only the number of needed bunches in the shadow of the nominal ERL operation. The length of the kicker waveform has to be extended up to 0.1 s (the risk of flashovers has to be carefully evaluated) to fulfil the test requirements.

In this case the lines have to include a triplet to vary the focal point and the beam size at the focal point. The different energy lines are recombined and a system analogous to the one used at the entrance of the Linacs is used. Steering magnets and a matching insertion are included as well. In total the line can be up to 30 m long and additional 10-20 m have to be considered for the test samples and the downstream beam dump. The parameters in Tab. 4.7 are used for the dump design. It is assumed that the beam setup is done with a reduced intensity, the full intensity beams will then be dumped on the samples. For further analysis, more detailed optics studies have to be performed, the dynamic range of the magnets and potential RP issues to be evaluated.

4.6 Photon Beam Production

4.6.1 Optical system

Depending on the electron-beam time-structure, various optical systems capable to produce high gamma-ray fluxes are nowadays available. On the one hand, for bunch trains of low repetition rate, non-linear [83] or passive [84] optical recirculators may be used (e.g.

ELI-NP-GS [85]: trains of 32 bunches separated by 16 ns at a repetition rate of 100 Hz). The related laser system has to provide the maximum pulse intensity allowed by the foreseen spectral density (e.g. ELI-NP-GS: 400 mJ at 100 Hz for green 515 nm light, 14 μm transverse spot size of the intensity profile and 3 ps longitudinal pulse width). On the other hand, for CW electron bunches of repetition rate $\gtrsim$ 10 MHz, Fabry-Perot cavities [86] (*i.e.* optical resonators) may be used [87, 88, 89, 90]. This is the technical solution envisaged for the PERLE photon beam facility.

Fabry-Perot cavities consist of a sequence of high reflectivity mirrors (see Fig. 4.30). When the laser beam frequency satisfies resonance conditions (see [91] for pulsed beams), the power is enhanced at most by a factor $G = F/\pi$ inside the cavity (in practice laser/cavity spatio-temporal mode mismatches can reduce this factor by several dozens of percent). The cavity finesse F depends on mirror losses and reflection coefficients. However, the higher the cavity enhancement factor the narrower the optical resonance $\Delta v/v = \lambda/(LF)$, where $v = c/\lambda$ is the laser frequency and L the cavity optical round-trip length. Dedicated laser cavity feedback is needed to preserve the resonance conditions [92, 91]. Experimentally, a cavity with $F \approx 28000$ ($G \approx 9000$) for picosecond pulses and with $L = 4$ m was demonstrated by some of us in [93].

Table 4.8: Expected laser beam and cavity parameters.

	$\lambda = 1030$ nm	$\lambda = 515$ nm
Laser beam average power (W)	200	100 (200)
Laser beam time FWHM (ps)	1-10	1-10
Cavity beam waist (μm)	60	60
Cavity beam intensity spot size (μm)	30	30
Cavity beam Rayleigh length (mm)	22.0	11.0
Cavity finesse	28000	28000
Cavity stacked average power (kW)	>600	>300 (>600)

The power that can be stored inside the cavity is limited by thermal effects and mirror coating damage threshold. An average power of 670 kW (for 10 ps pulses and 250 MHz repetition rate) was obtained [94] for intra-cavity high-harmonic attosecond pulse experiments [95]. Concerning Compton experiments, 50 kW was recently demonstrated by some of us on the ATF electron ring of KEK [96]. A 35.68 MHz cavity ($L \approx 8.4$ m) designed for storing 10 ps pulses of average power above 600 kW is presently under development at

LAL by some of us for the Compton X-ray machine ThomX [97]. This is a similar optical cavity that is needed for the PERLE photon beam facility. Besides, a CW laser beam of 700 kW will also be stored in the VIRGO interferometer in a near future [98]. There is thus a global effort to achieve stable and routinely operating cavities in high average power regime. One should also mention that developments on long $L \approx 30$ m monolithic and high finesse cavity are also on-going [99].

Mode properties (wave front profile, polarization) of optical cavities solely depend on their geometries. Specific optical designs must then be supplied to fulfill the requirements of Compton experiments [100, 101]. Following the arguments of Ref. [101], one must consider planar four-mirror cavities made of at least two concave reflective surfaces for the ERL SCRF photon beam facility (see Fig. 4.30). The distance between the two planar mirrors (M_1 and M_2) can be adjusted to lock the cavity round-trip frequency to the accelerator radio-frequency while the distance between the two concave mirrors (M_3 and M_4) can be varied to tune the laser beam spot size at the IP. This geometry has been successfully tested at the ATF [90]. Eventually, with a careful design of the high reflectivity mirror coating, the mode polarization of a planar four-mirror cavity can be freely tuned.

The laser source is of prior importance for high finesse cavities. One must start from a low phase noise mode-locked oscillator and then amplify the signal using the chirped pulse amplification technique [102]. The laser amplifier system is also of prior importance because it must not induce additional phase noise (e.g. AM/PM coupling via non linear processes) while providing stable and long term operations. Considering a repetition rate of 40 MHz and picosecond pulses, the most mature and powerful technology is based on Ytterbium-doped diode-pumped fibres. Reasonably low noise laser mode-locked oscillators are commercially available at this wavelength (around 1030 nm) and amplifiers with up to an average power of 830 W [103] (and more recently 2 kW [104]) was demonstrated on a table top experiment. Besides, a fully connectorised and compact *Yb* doped fibre amplifier system providing 50 W has been operated over days at ATF/KEK [90] in gamma ray production experiments. This system has been recently upgraded to 200 W at CELIA for the ThomX project. This is what is needed for the PERLE photon beam facility. Using a LBO crystal, the laser beam frequency can finally be doubled with more than 50% efficiency before entering the optical cavity to provide a high average power beam at a wavelength close to 515 nm. Eventually one can also parallelize two fiber amplifiers to compensate for the second harmonic generation limited efficiency [105, 106, 107].

To reach a stored average power of more than 300 kW, the cavity finesse must be

≈ 30000 leading to $\Delta v / v \approx 2 \cdot 10^{-12}$. A strong feedback between laser and cavity is clearly required to keep the system on resonance. However, it should be mentioned that such a high average power has never been demonstrated for a wavelength of 515 nm. Apart from higher absorption in SiO_2, one of the dielectric dioxide used for high reflective coating, one does not expect tremendous differences for the cavity finesse foreseen here, experimental tests could be done at LAL and CELIA. The laser beam and cavity parameters are summarized in Tab. 4.8.

For other laser beam wavelengths one could also use gain media doped with the other rare earth elements Er (1.5 μm) or Tm (1.9 μm) [108]. Performances would be reduced with regard to Yb but still useful. Using quarter wave stack cavity mirror coatings one could also consider filling a single cavity with λ and $\lambda/3$ (e.g. doubled Yb: 515 nm and Er: 1545 nm) to provide a gamma frequency together with its third harmonic.
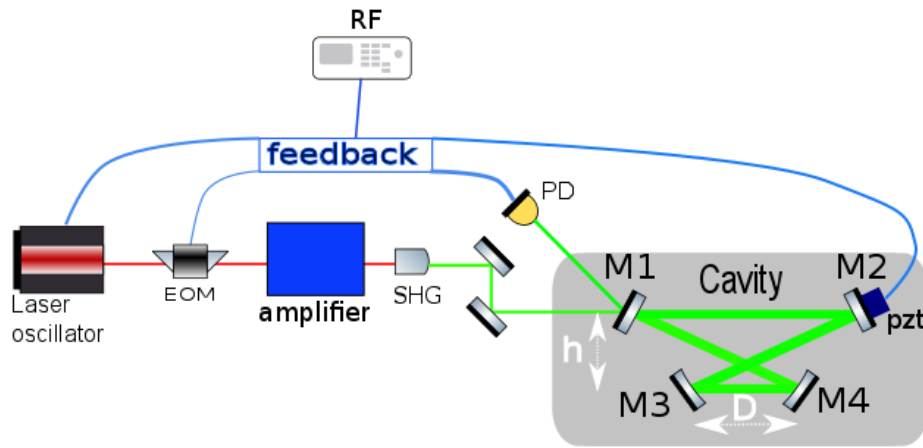

Figure 4.30: Simplified scheme of a four mirror cavity locked to an amplified laser oscillator. Planar (M_1 and M_2) and concave (M_3 and M_4) mirrors are shown along with the electro-optic modulator (EOM) used to build the feedback error signal from the reflected signal (photodiode PD) and a piezo-electric transducer (PZT) fixed on M_2 to synchronize the cavity round trip frequency to the accelerator RF.

4.6.2 Cavity design

There is freedom in choosing the cavity geometry. Here a trade-off is proposed between a small laser-electron crossing angle, small enough laser beam spot size at the IP while

(a)   (b)
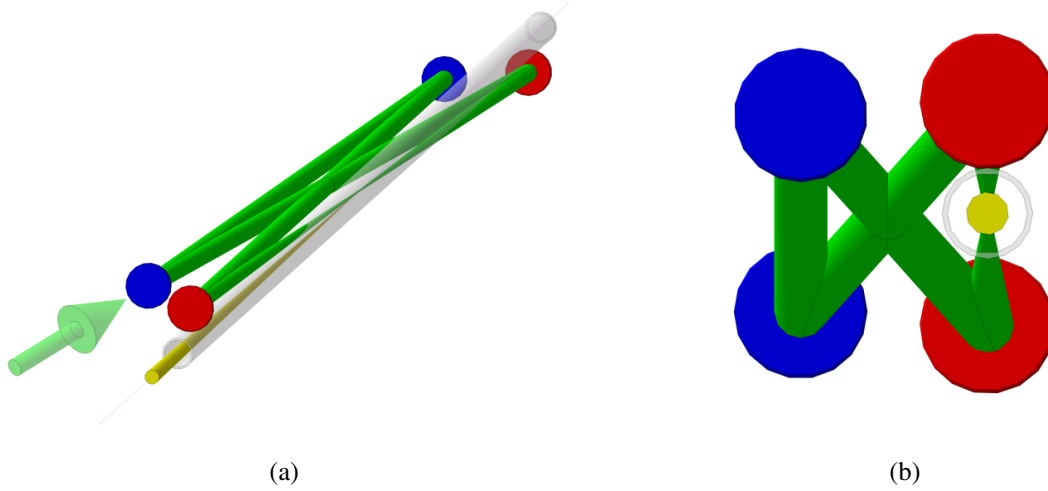
Figure 4.31: Schematic view of a possible four-mirror cavity implementation. (a) Isometric view; (b) face projection view. Red discs: concave mirrors; blue disks: plane mirrors. The cavity mode is represented as a green tubes (radius corresponding to $\approx 6\sigma$ of the intensity Gaussian profile) and cones, the beam pipe as a gray tube and the gamma ray beam as a yellow cone.

ensuring reasonably large spot sizes on the mirror surfaces. To calculate the cavity mode one considers a planar four-mirror cavity (see Fig. 4.30 and Fig. 4.31 for a possible implementation) with $L = 7.5$ m seeded with a 40 MHz pulsed laser beam of wavelength 515 nm. Assuming a quasi symmetric geometry we set the distance between the concave mirrors D close to $D_0 = 2$ m and the distance $h = 35$ mm to avoid beam vignetting effects induced by the 15 mm inner diameter beam pipe (see Fig. 4.31.b). The concave mirror radius of curvature is fixed to D_0 and the mirror diameters to 1 inch. The laser beam waist w_0 is shown as a function of $\Delta D = D - D_0$ in Fig. 4.32.a. Small waist values are thus obtained for the very mechanically stable confocal geometry ($D \gtrsim D_0$) [101] though very close to the modal instability region. We choose $w_0 = 60\ \mu$m (*i.e.* 30 μm Gaussian intensity spot size). As expected [109], the transverse mode profile is elliptical and the main radii are shown as a function of the optical path length in Fig. 4.32.b. From this figure one sees that the mode is collimated between the two plane mirrors with a beam radius of approximately 2.7 mm on the mirror surfaces. Such beam radius leads to negligible diffraction losses induced by the 1 inch mirror edges. We obtain a crossing angle between the laser beam and the electron bunch of 1.2°. With $h/D = 0.017$, the incident angle on the concave mirror is 0.53° leading to a small mode ellipticity of roughly 2.4% and negligible

₁₄₄₇ polarization instabilities [100]. As for the mechanical mirror mounts, motion actuators and
₁₄₄₈ vacuum vessel, we propose to adopt the technical solutions tested successfully over years
₁₄₄₉ at ATF/KEK [90],[97]. It is noticeable that these elements were recommissioned without
₁₄₅₀ any difficulty after the 2011 earthquake, and the design can thus be considered as robust.
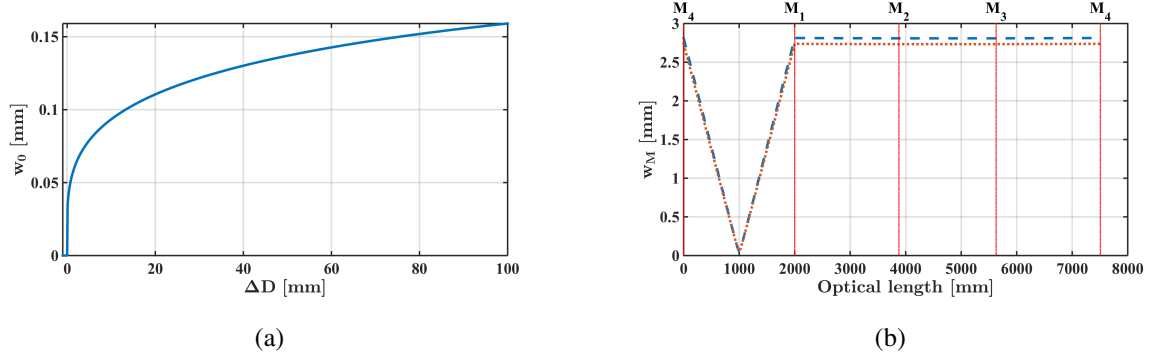

(a)   (b)

Figure 4.32: (a) Minimum mode cavity waist as a function of the distance between the two concave mirrors ($\Delta D = D - D_0$). (b) Main mode radii as a function of the optical path inside the cavity. Dashed curve: maximum beam radius; dotted curve: minimum beam radius. Positions of the four mirrors are also indicated by vertical lines.

CHAPTER 5

Monitoring and Operation

An energy-recovering linac (ERL) - though combining features of both linear and circular accelerators - is a non-equilbrium system that lacks a closed orbit and potentially does not possess global betatron or synchrotron stability. It is thus more closely equivalent to a time-of-flight spectrometer or injector than it is to a conventional accelerator, and so encounters a number of unique operational issues [110, 111]. Firstly, longitudinal motion is of paramount importance: timing and energy control set the system architecture, and thus RF phase and gradient control must be assured, as must the lattice momentum compaction - the dependence of the time of flight on energy. Secondly, as it is a non-equilibrium system (in contrast to, say, an electron storage ring), stability is a significant challenge. Thirdly, halo effects dominate operation, much as they do in injection systems, where losses can be performance limiting. Particular concerns include activation (as in injectors), damage (burn-through), and background for experimental users. Finally, as an inherently multi-pass system, an ERL must control multiple beams with different properties (e.g. energy or emittance) during transport through, and handing in, common beamline channels. Reliable machine operation thus requires a comprehensive strategy for machine commissioning, operations, monitoring machine health, system stabilisation, and machine protection.

5.1 Operational Regimes

ERL operation comprises a series of phases: commissioning, beam operations, and machine tuning/recovery. During each phase, system behaviour falls into various classes that can be differentiated by the time scales on which they are manifest: 'DC' conditions - those associated with the machine set point intended to produce required beam conditions for users, 'drift' effects - slow wandering of the set-point (due, for example, to thermal effects) degrading system output, and 'fast' effects (at acoustical to RF time scales), resulting in beam instability. A fourth class - that of transient effects (for example, RF loading during beam on/off transitions and fast shut-down in the event of sudden beam loss for machine protection purposes) - can occur throughout all operational cycles.

5.2 Machine Commissioning

Machine commissioning has combined goals of validating system design architecture and defining a recoverable system operating point. For an ERL, this requires demonstration of the control of phenomena of concern - such as beam break-up (BBU) and the micro-bunching instability (μBI) - while generating settings for hardware components. Following pre-commissioning 'hot' checkout of accelerator components and commissioning of hardware subsystems, beam operations commence with threading of low power beam so as to establish a beam orbit and correct it to specified tolerances. This requires orbit correction systems based on beam position monitors and steerers (typically every quarter-betatron wavelength); unique to a multipass ERL with common transport of multiple beams in a single beam line is the requirement that the system correct perturbations locally so that the multiple passes respond identically and the orbits not diverge unacceptably from turn to turn. Similarly, a baseline for longitudinal beam control must be established, by synchronising the beam to the RF using recirculator arcs as spectrometers for precision measurements of energy gain. Any path length adjustments needed to set RF phases and insure energy recovery per the design longitudinal match are thus determined. With a 6D phase space reference orbit thus defined, the beam and lattice behaviour is tuned and validated. Lattice performance is measured, tuned, and certified using differential orbit/lattice transfer function measurements; these, too, will require pass-to-pass discrimination amongst beams in common transport. Both transverse and longitudinal measurements (using phase transfer function diagnostics [112]) are necessary for a full analysis of lattice behaviour.

Corrections must be applied to 'rematch the lattice' and bring both transverse (betatron motion/focusing) and longitudinal (timing/momentum compaction) motion into compliance with design (or to establish an alternative working point). Certification of lattice performance allows analysis, tuning, and validation of beam parameters, and matching of the beam to the lattice. This requires measurements of both betatron (emittance, beam envelope functions) and longitudinal (bunch length/energy spread/emittance, phase/energy correlation) properties. Disentangling the properties of multiple beams in common transport may prove challenging and require use of beyond-state-of-the-art techniques. If beam properties differ excessively from specification, 'matching' of the beam to the lattice is performed using appropriate correction algorithms. As with orbit correction, perturbations will likely require local correction so as to avoid excessive pass-to-pass divergence of beam properties. Given a validated working point, beam power scaling is performed, with currents increased from tune-up levels to full power CW. Transient control and beam stabilization (see below) will be initially investigated and demonstrated during commissioning; they remain a persistent activity through the operational lifetime of the machine, and are therefore discussed below.

5.3 Machine Operation: Monitoring and Maintaining Machine Health

Routine machine operations entail numerous monitoring and correction functions intended to provide beam stability for users and to control and preserve machine performance at a specific set point. These include timing and energy control, which is needed to provide synchronism, for example, at an interaction point, and to maintain the stability of delivered beam properties. This may require a high resolution timing system (if user timing is critical), and will require continuous measurement of energy and energy stability and control mechanisms for energy stability (see the following discussion of stabilisation). Similarly, user requirements may demand measurement and precise control of the orbit of the delivered beam. This can be provided by appropriate enhancements to - and utilisation of a subset of - the beam orbit correction system provided for orbit control during commissioning. Both transverse and longitudinal controls of this type are needed as the machine is used to explore beam dynamics, instability control, and beam quality preservation. Machine performance is susceptible to degradation as system parameters change due

to thermal effects and hardware parametric drift. Beam and lattice properties, control parameters, magnets, and RF variables are all susceptible to such effects; control algorithms providing appropriate monitoring of, and intervention/correction so as to restore RF gradients/phases, beam orbits, lattice focusing, and beam properties are required. These may be established as intermittent machine performance checks and retuning procedures, or, alternatively, be considered as 'low speed feedback' systems in which critical beam and machine parameters are monitored and corrected. These provisions are also used for recovering machine configurations/working points after trips and system shutdowns. Halo control is critical to the operation of high power ERLs. Halo sources include field emission in SRF systems, cathode-driven sources (such as light scattered onto active areas and surface defects) that can change with ageing, beam/residual gas interactions, beam/wake interactions, and beam dynamical effects during beam formation and handling. All can lead to significant radiation background and potentially unacceptable levels of beam loss. Methods/hardware for monitoring and independent tuning of large amplitude components of multiple beams in common transport are therefore necessary to avoid activation and damage to system components. These can include collimation and/or nonlinear matching using, for example, higher order multipoles (sextupoles, octupoles, etc), and require the use of large dynamic range diagnostics [113]. Transient control (maintaining machine and beam health through RF trips, other fast shutdowns, and/or inevitable hardware problems) is needed for all phases of machine operation and is discussed below.

5.4 System Stabilisation

ERLs are non-equilibrium systems subject to drift, jitter, and instability in any of numerous system variables on any of several time scales. They are typically under-constrained, with the number of noise-subjected control parameters much larger than the output observables of relevance to users. Specific strategies for system stabilisation are therefore needed. User requirements must be established from the outset of the system design process, and provision for hardware, software, and procedural control made so as to achieve adequate stability. Table 5.1 outlines critical challenges. Globally, drift and jitter must be controlled - at the very least - for the key system parameters of energy and orbit. Beam energy will vary as a result of drift in RF phases; stabilisation by recovery of proper phasing will be necessary over the course of minutes or hours, and may be necessary on short time scales. This can be accomplished through the use of phase stabilisation and control and

TIME SCALE/MAGNITUDE OF EFFECTS				
Class of Control	DC	Slow (up to thermal)	Fast (<1 kHz)	RF/dynamic
Lattice	transfer map (set point)	transfer map (drift)	magnet jitter (power, vibration)	
Beam orbit	central orbit	orbit drift	orbit jitter	Beam stability (e.g. BBU)
Beam properties	match to lattice (setpoint)	match drift	Instability	
Halo	experimental background	drift	electron/ion instability?	electron/ion instability?

Table 5.1: System stability issues in energy recovery linacs

by providing energy verniers [114]. Energy control is coupled to synchronism and timing Orbit stability also varies over time and can be subject to jitter. Though orbit stabilisation techniques are well established, the presence of multiple beams in common transport places constraints on both the diagnostics on which the controls are based and on the feedback methods to be used so as to insure that beam- and pass-specific results are achieved. Given the presence of both high beam brightness and high beam power, the possible need for instability control (BBU, wake effects, etc) must be considered, and the system design should provide opportunity for fast feedback if necessary. Similarly, stability of beam properties is not assured, and means of continuous monitoring/adjusting delivered beam quality (e.g. energy spread, bunch length, spot size/divergence, bunch, etc.) should be provided as necessary.

5.5 Transient Control and Machine Protection

ERLs are subject to numerous transient effects, two classes of which are of particular operational importance: the impact of RF transients (beam off/on transients, variable beam loading during current ramps, and RF trips), and machine protection fast shutdowns. RF transients due to variations in beam loading [115] are manageable with appropriate RF drive design. Care in choice of Q_{ext} is of importance, as is planning for the type and operational range of the longitudinal match; implementation of incomplete energy can result in greater transient control requirements than encountered in systems with complete energy

recovery. The RF drive system (control loops, feed-forward/back) must be configured to manage transients as experienced under different machine operating conditions and operating points; RF power and cavity tuning should be monitored during routine operation to insure that stability is maintained. Dramatic transients (particularly in beam loading) will occur during machine-protection-system (MPS) driven fast shutdowns. As ERL beam powers are very high, loss tolerances are tight and large losses must be prevented. Critical to machine safety, the MPS continually monitors the accelerator for beam loss and rapidly shuts off the beam if unsafe loss levels are observed [116]. The machine control system monitors and records the interlock sequence precipitating the fast shutdown so as to characterise the source of the transient event and provide guidance on correction of the fault.

CHAPTER 6

The interest in PERLE, sketched in the present report, is threefold, regarding its technology development potential, its physics and applied user programme and its importance for demonstrating and studying the technology choice of the LHeC. At present there is no decision as to where PERLE may be placed. An initial study, of also general interest, considered the possibility of hosting PERLE at CERN. This is sketched below. It was subsequently studied to possibly build this facility at LAL Orsay, may be at reduced beam energy for keeping its dimension fit to the available infrastructure and halls. This is also mentioned below. Recently, an idea has also been considered of building a low energy, lower current version of PERLE at Darmstadt in Germany.

6.1 Introduction

As mentioned in the lattice section, the genuine footprint of the PERLE facility at its maximum energy of about 1 GeV occupies a rectangle of $42 \times 14 \, \text{m}^2$. This area should be enclosed by shielding at a sufficient distance to allow passage and maintenance operations. We estimate the required passage and half thickness of the accelerator component to 2 m. A concrete shielding of 50 cm thickness is assumed here to stop photons and neutrons produced by halo electrons. Detailed simulations of the radiation generated by the impinging electron will be necessary at a later stage. An increase of the shielding required could be

alleviated by the use of denser materials like lead. Access conditions and the geographical location of the site may also influence the final choice of shielding. In addition to this central area, space needs to be allocated for the auxiliary systems like:

- Power converters for magnets, septa and kickers;

- RF power. Assuming IOTs or solid state amplifiers as close as possible to the SRF modules to minimize RF losses;

- Water cooling.The dimensioning of this system greatly depends on the operational modes;

- Cryogenics. The use of a dewars for storing liquid helium at 4.5 could avoid the cost of a liquefier. However it will limit flexibility of operation in non-recovery mode and needs to be studied further;

- Source;

- Dump. A design of the dump exists with a minimum length of 50 m (reference) but a more compact version could be used by limit the current or repetition rate when working on non recovery mode;

As a rough estimate one would like to double the area of the accelerator itself to accommodate all services. It is worth noting that some services like RF power generation or power supplies may be placed on a different level than the accelerator itself, while the source or the dump may not. We do not consider here the use of the interior part of the ring as the escape routes would be compromised. It may however be used to house a low energy dump which itself needs to be shielded and which will have restricted access.

6.2 CERN

For an initial study, we have been considering existing buildings around the CERN site. The building needs to be equipped with a crane, water and electricity services. The availability of cryogenic fluids would be an interesting option and provide considerable savings. The installation of electrical power and demineralised water seems to be less costly. The total area of the installation would be then of the order of $1500\,\mathrm{m}^2$ with an incompressible area of approximately $45 \times 17\,\mathrm{m}^2$ to host the accelerator footprint and shielding. There are

not many buildings of this dimension at the CERN site and they are in general already in use for large facilities like the superconducting test facility in SM18 or the magnet repair facility in building 180. A couple of sites have been identified which would suit the area requirements and present some advantage like the availability of cryogenics (b.973), power (b. 2275) or shielding (b. 2003).

If one deemed to better construct a new building one promising location is around the area 18, where a powerful cryogenic plant can serve the accelerator while the proximity to SM18 could ease the use of the electron beam for quench tests. This location would also be compatible with the possibility to use PERLE as an injector to the LHeC. The detailed plans and costing of such a building would have to be studied for CERN. Naturally, a location of PERLE outside of CERN would pose other constraints and opportunities.

6.3 LAL Orsay

Near to the time of publication of this report it has been realised that the campus of LAL Orsay would be very well prepared to house PERLE at up to 450 MeV energy which required an inner area of about $20 \times 7\,\text{m}^2$. The building that could host this version of PERLE is a former experimental hall (Super ACO hall) of about $1850\,\text{m}^2$, which is equipped with cranes and electricity. The ground of the building is made of concrete slabs with variable ground resistance. Nevertheless, more than the half of the hall area has a sufficient resistance to allow the installation PERLE. A complete study will be performed to confirm this fact. Being next to the tunnel of the old Orsay linac and close to the "Igloo", where new accelerators are currently installed, the building is partially shielded and water-cooling circuits could be shared with the other machines. The building gives the possibility to install the RF source and the power supplies at a different level than the accelerator. An existing control room that overlooks the experimental hall could be used for PERLE. Since all the accelerators installed nearby are based on warm technology, a cryogenic plant has to be built. Altogether, this appears to be an available, suitable place. It would be of interest for the development of physics and technology at Orsay and internationally.

Summary

Design concepts and applications have been presented of a novel, powerful energy recovery linac facility suitable to enable SCRF technology developments and intense, low energy electron and photon physics experiments, termed PERLE. The two main goals of PERLE are to i) develop and demonstrate the viability of the basic design assumptions for a 60 GeV electron multi-turn ERL linac as is proposed to be installed tangential to the LHC, the HE-LHC and/or a future FCC, for realising exploratory electron-proton experiments at O(1000) times the luminosity of HERA, and ii) to enable technical developments and applications as well as future physics experiments in a novel, high current ERL facility environment. Its parameters and technology choices are largely derived from the LHeC and in turn need to be compliant with the LHC and the goal of building a novel, energy frontier ep collider of $10^{34}\,\mathrm{cm}^{-2}\mathrm{s}^{-1}$ luminosity designed for concurrent operation with the LHC. This determines the frequency, chosen to be 802 MHz, the number of turns to three and the electron beam current to be as large as about 15 mA.

PERLE is foreseen to demonstrate and gain operational experience with low-frequency high-current SCRF cavities and cryomodules of a type suitable for scale up to a high-energy machine. Since the cavity design, HOM couplers, FPC's etc. will be all new or at least heavily modified, PERLE will serve as a technology test bed that will explore all the parameters needed for a larger machine. There is no other high current ERL test bed in the world that can do this. PERLE will feature emittance preserving recirculation optics and this will also be an important demonstration that these can be constructed and operated in a flexible user-facility environment. The machine, when transformed from a test to a user

98

facility, must run with high reliability to provide test beams for experimenters or ultimately provide Compton or FEL radiation to light source users. This demonstration of stability and high reliability will be essential for any future large facility.

As an example for technical impact, the present study has demonstrated the use of the electron beam to perform quench tests on SC components and magnets. The facility may be used for low energy test beam measurements and it may serve as a base to design or build the injector of the LHeC.

The basic physics case is presented for new measurements of current outstanding importance. Relying on a luminosity of $O(10^{40})\,\text{cm}^{-2}\text{s}^{-1}$, in elastic ep scattering, most accurate investigations of electroweak loop effects and the proton radius as well as searches for new physics, such as dark photons, characterise the extremely attractive physics potential of the PERLE facility.

An exiting physics programme has been detailed from operating PERLE as a gamma ray facility with a very high flux, at least two orders of magnitude above expected upgrades of existing facilities, and superior spectral density. A path is shown to discoveries using up to 30 MeV photons and for a variety of novel, unique and precise measurements on photo-nuclear reactions, nuclear structure as well as to important measurements for neutrino and nuclear astrophysics.

A thorough simulation study is presented of the system architecture, the transport optics and start-to-end beam dynamics. The paper presents initial design concepts of the main components for PERLE, applicable also to its possible lower energy version. These comprise descriptions of the source and injector, the 802 MHz cavity, under design and construction by us, of a cryomodule and HOM design considerations. Further, the inventory and novel designs are presented of the arc magnets. A section is devoted to rather detailed considerations for the dumps and transfers.

For CW electron bunches of larger than 10 MHz repetition rate, Fabry-Perot optical resonators are suitable to provide a high quality photon beam and are presented in this paper as a preferred reliable solution.

A final chapter is devoted to the monitoring and operations tasks including the commissioning, system stabilisation and protection aspects. Considerations have also been presented for the site and its infrastructure. These naturally will be updated once a site is finally chosen which most likely will be at the campus of the Linear Accelerator Laboratory at Orsay (Paris).

PERLE has the opportunity to be a clean-sheet globally optimised design for a new

generation of high average power efficient ERL based machines, a novel testing ground for far reaching experiments with electron and photon beams of unique quality and, not least, to become a prime technical base for an electron beam upgrade of the LHC, i.e. a new generation of deep inelastic scattering experiments entailing the precision study of the Higgs boson and the exploration of new physics at TeV energies.

Acknowledgement

Bibliography

[1] J. L. A. Fernandez and the LHeC Study Group, "A Large Hadron Electron Collider at CERN - Report on the Physics and Design Concepts for Machine and Detector," *Journal of Physics G: Nuclear and Particle Physics*, vol. 39, no. 7, p. 075001, 2012.

[2] M. Klein, "Deep inelastic scattering at the energy frontier," *Annalen Phys.*, vol. 528, pp. 138–144, 2016.

[3] F. Zimmermann, O. Brüning, and M. Klein, "The LHeC as a Higgs Boson Factory," *MOPWO054, Proceedings of IPAC2013*, 2013.

[4] O. Brüning and M. Klein, "The Large Hadron Electron Collider," *Mod. Phys. Lett.*, vol. A28, no. 16, p. 1330011, 2013.

[5] J. Wang (ed), "ERL and the Beam Dynamics Challenges," *ICFA Newsletter*, vol. 68, pp. 11–139, December 2015.

[6] C. Tennant , "Energy Recovery Linacs," *Challenges and Goals for Accelerators in the XXI Century*, eds. O. Brüning and S. Myers, World Scientific, 2016.

[7] K. Aulenbacher, "The MESA accelerator," *AIP Conf. Proc.*, vol. 1563, pp. 5–12, 2013.

[8] M. Abo-Bakr *et al.*, "Progress Report of the Berlin Energy Recovery Project BERLinPro," in *Proceedings, 6th International Particle Accelerator Conference (IPAC 2015)*, p. TUPWA018, 2015.

[9] I. Bazarov *et al.*, "The Cornell-BNL FFAG-ERL Test Accelerator: White Paper," arXiv:1504.00588, 2015.

[10] G. Hoffstaetter, "C-β 4-Turn ERL with FFAG," *Presented at FCC Workshop at Rome*, 2016.

[11] S.A.Bogacz et al., "ER at CEBAF - A Test of 5-Pass Energy Recovery at CEBAF," *Proposal to PAC Jefferson Laboratory*, 2016.

[12] D. Douglas, S. Benson, A. Hofler, R. Kazimi, G. Krafft, R. Li, Y. Roblin, C. Tennant, B. Terzifa, and C.-Y. Tsai, "Control of Synchrotron Radiation Effects during Recirculation," in *Proceedings, 6th International Particle Accelerator Conference (IPAC 2015)*, p. TUPMA035, 2015.

[13] Extreme Light Infrastructure, www.eli-np.ro.

[14] A. Verweij , *QP3: User Manual*, 2008. CERN/TE, EDMS 1150045.

[15] L. Bottura *et al.*, "THEA Thermal, Hydraulic and Electric Analysis of Superconducting Cable," *CryoSoft, Geneva*, 2003.

[16] B. Auchmann *et al.*, "Testing beam-induced quench levels of lhc superconducting magnets in run1," *Physical Review Special Topics Accelerators and Beams*, 2015.

[17] A. Fasso *et al.*, *FLUKA: a Multi-Particle Transport Code*, 2005. CERN-2005-10, INFN/TC_05/11, SLAC-R-773.

[18] T.T. Bohlen *et al.*, *The FLUKA Code: Developments and Challenges for High Energy and Medical Applications*, 2014. Nuclear Data Sheets 120, 211-214.

[19] R. Hofstadter, "Electron scattering and nuclear structure," *Rev.Mod.Phys.*, vol. 28, pp. 214–254, 1956.

[20] R. Essig, J. A. Jaros, W. Wester, P. H. Adrian, S. Andreas, *et al.*, "Working Group Report: New Light Weakly Coupled Particles," 2013.

[21] N. Arkani-Hamed, D. P. Finkbeiner, T. R. Slatyer, and N. Weiner, "A Theory of Dark Matter," *Phys.Rev.*, vol. D79, p. 015014, 2009.

[22] J. Erler and M. J. Ramsey-Musolf, "The Weak mixing angle at low energies," *Phys. Rev.*, vol. D72, p. 073003, 2005.

[23] M. Klein and T. Riemann, "Weak Neutral Currents in Elastic Muon-Nucleon Scattering," *Z.Phys.*, vol. C8, p. 239, 1981.

[24] H. Davoudiasl, H.-S. Lee, and W. J. Marciano, "Low Q^2 weak mixing angle measurements and rare Higgs decays," *Phys. Rev.*, vol. D92, no. 5, p. 055005, 2015.

[25] J. C. Bernauer and R. Pohl, "The proton radius problem," *Sci.Am.*, vol. 310, no. 2, pp. 18–25, 2014.

[26] P. J. Mohr, B. N. Taylor, and D. B. Newell, "CODATA Recommended Values of the Fundamental Physical Constants: 2010," *Rev.Mod.Phys.*, vol. 84, pp. 1527–1605, 2012.

[27] J. Bernauer *et al.*, "High-precision determination of the electric and magnetic form factors of the proton," *Phys.Rev.Lett.*, vol. 105, p. 242001, 2010.

[28] M. O. Distler, J. C. Bernauer, and T. Walcher, "The RMS Charge Radius of the Proton and Zemach Moments," *Phys.Lett.*, vol. B696, pp. 343–347, 2011.

[29] J. Bernauer *et al.*, "Electric and magnetic form factors of the proton," *Phys.Rev.*, vol. C90, no. 1, p. 015206, 2014.

[30] A. Gasparian, "The PRad experiment and the proton radius puzzle," *EPJ Web Conf.*, vol. 73, p. 07006, 2014.

[31] M. Mihovilovic *et al.*, "Initial state radiation experiment at MAMI," *EPJ Web Conf.*, vol. 72, p. 00017, 2014.

[32] A. Bernstein, "Symmetry Tests in Photo-Pion Production," *AIP Conf.Proc.*, vol. 1563, pp. 159–162, 2013.

[33] B. Holdom, "Two U(1)'s and Epsilon Charge Shifts," *Phys.Lett.*, vol. B166, p. 196, 1986.

[34] N. Arkani-Hamed and N. Weiner, "LHC Signals for a SuperUnified Theory of Dark Matter," *JHEP*, vol. 0812, p. 104, 2008.

[35] J. Balewski, J. Bernauer, J. Bessuille, R. Corliss, R. Cowan, *et al.*, "The DarkLight Experiment: A Precision Search for New Physics at Low Energies," 2014.

[36] Y. Kahn and J. Thaler, "Searching for an invisible A' vector boson with DarkLight," *Phys.Rev.*, vol. D86, p. 115012, 2012.

[37] I. Rachek, J. Arrington, V. Dmitriev, V. Gauzshtein, R. Gerasimov, *et al.*, "Measurement of the two-photon exchange contribution to the elastic $e^{\pm}p$ scattering cross sections at the VEPP-3 storage ring," *Phys.Rev.Lett.*, vol. 114, no. 6, p. 062005, 2015.

[38] D. Adikaram *et al.*, "Towards a resolution of the proton form factor problem: new electron and positron scattering data," *Phys.Rev.Lett.*, vol. 114, no. 6, p. 062003, 2015.

[39] R. Milner *et al.*, "The OLYMPUS Experiment," *Nucl.Instrum.Meth.*, vol. A741, pp. 1–17, 2014.

[40] N. Pietralla et al., *Phys. Rev. Lett.* **88**, *012502*, 2002.

[41] V. N. Litvinenko et al., *Nucl. Instr. and Meth. A* **407**, *8*, 1998.

[42] W. Bothe and W. Gentner, *Z. Phys.* **106**, *236*, 1937.

[43] T. Otsuka, T. Suzuki, J.D. Holt, A. Schwen and Y. Akaish, *Phys. Rev. Lett.* **105**, *032501*, 2010.

[44] R.-D. Herzberg et al. *Phys. Rev. C* **56**, *2484*, 1997.

[45] U. Kneissl, N. Pietralla, A. Zilges, *J. Phys.* **G32**, *R217*, 2006.

[46] K. Langanke et al., *Phys. Rev. Lett.* **93**, *202501*, 2004.

[47] J. Beller, N. Pietralla et al., *Phys. Rev. Lett.* **111**, *172501*, 2013.

[48] A. Arcones and J. Bliss, *J.Phys.* **G41**, *044005*, 2014.

[49] Erik J. Ramberg (Fermilab)., "Ilcws08 test beam summary," 2009.

[50] "Particle accelerators around the world." `http://www-elsa.physik.uni-bonn.de/accelerator_list.html`.

[51] M. Borland, "elegant: A flexible sdds-compliant code for accelerator simulation," 2000.

[52] D. Pellegrini, A. Latina, and D. Schulte, "Placet2: A novel code for beam dynamics in recirculating machines," 2015.

[53] "Free-electron lasers at the elbe - center for high-power radiation sources at the hzdr in dresden-rossendorf." `https://www.hzdr.de/db/Cms?pNid=471`.

[54] C. Hernandez-Garcia, T. Siggins, S. Benson, D. Bullard, H. F. Dylla, K. Jordan, C. Murray, G. R. Neil, M. Shinn, and R. Walker, "A high average current DC GaAs photocathode gun for ERLs and FELs," *Conf. Proc.*, vol. C0505161, p. 3117, 2005. [,3117(2005)].

[55] L. B. Jones, J. W. McKenzie, K. J. Middleman, B. L. Militsyn, Yu. M. Saveliev, and S. L. Smith, "The ALICE Energy Recovery Linac: Project overview and injector performance," *J. Phys. Conf. Ser.*, vol. 298, p. 012007, 2011.

[56] T. Obina *et al.*, "Recent Developments and Operational Status of the Compact ERL at KEK," in *Proceedings, 7th International Particle Accelerator Conference (IPAC 2016): Busan, Korea, May 8-13, 2016*, p. TUPOW036, 2016.

[57] I. V. Bazarov *et al.*, "Photocathode & at Cornell University," *Conf. Proc.*, vol. C1205201, pp. 2137–2139, 2012.

[58] J. Grames, P. Adderley, J. Brittian, J. Clark, J. Hansknecht, D. Machie, M. Poelker, M. L. Stutzman, R. Suleiman, and K. Surles-Law, "Lifetime measurements of high polarization strained-superlattice gallium arsenide at beam current >1 milliamp using a new 100kv load lock photogun," *Conf. Proc.*, vol. C070625, p. 3130, 2007. [,3130(2007)].

[59] K. Aulenbacher, "Polarized beams for electron accelerators," *Eur. Phys. J. ST*, vol. 198, pp. 361–380, 2011.

[60] K. Flottmann, "Note on the thermal emittance of electrons emitted by cesium telluride photo cathodes. The thermal emittance of electrons emitted by cesium telluride photo cathodes," Tech. Rep. TESLA-FEL-97-01, DESY, Hamburg, Feb 1997.

[61] T. Siggins, C. Sinclair, D. Bullard, D. Douglas, A. Grippo, J. Gubeli, G. Krafft, B. Yunn, and C. Bohn, "Performance of a DC GaAs photocathode gun for the Jefferson lab FEL," *Nucl. Instrum. Meth.*, vol. A475, pp. 549–553, 2001.

[62] C. Gerth and F. E. Hannon, "Injector Design for the 4GLS Energy Recovery Linac Prototype," in *9th European Particle Accelerator Conference (EPAC 2004) Lucerne, Switzerland, July 5-9, 2004*, 2004.

[63] B. L. Militsyn, I. Burrows, R. J. Cash, B. D. Fell, L. B. Jones, J. W. McKenzie, K. J. Middleman, H. E. Scheibler, and A. S. Terekhov, "High voltage DC photoinjector development at Daresbury Laboratory," *ICFA Beam Dyn. Newslett.*, vol. 51, pp. 161–170, 2010.

[64] N. Nishimori *et al.*, "Development of a 500-kV photocathode DC gun for ERLS," *J. Phys. Conf. Ser.*, vol. 298, p. 012005, 2011.

[65] D. Dowell *et al.*, "First operation of a high duty factor photoinjector," *Conf. Proc.*, vol. C930517, pp. 2967–2969, 1993.

[66] D. Bisero *et al.*, "High efficiency photoemission from cs-k-te," *Appl.Phys.Lett.*, vol. 70, pp. 1491–1493, 2001.

[67] A. Burrill, I. Ben-Zvi, D. Pate, T. Rao, Z. Segalov, and D. Dowell, "Multi-alkali photocathode development at Brookhaven National Lab for application in superconducting photoinjectors," *Conf. Proc.*, vol. C0505161, p. 2672, 2005. [,2672(2005)].

[68] R. R. Mammei *et al.*, "Charge lifetime measurements at high average current using a K_2CsSb photocathode inside a dc high voltage photogun," *Phys. Rev. ST Accel. Beams*, vol. 16, no. 3, p. 033401, 2013.

[69] M. BastaniNejad, P. A. Adderley, J. Clark, J. M. Grames, J. Hansknecht, M. Poelker, M. L. Stutzman, R. Suleiman, K. E. L. Surles-Law, and J. L. McCarter, "CEBAF 200 kV Inverted Electron Gun," *Conf. Proc.*, vol. C110328, pp. 1501–1503, 2011.

[70] N. Nishimori, R. Nagai, S. Matsuba, R. Hajima, M. Yamamoto, Y. Honda, T. Miyajima, H. Iijima, M. Kuriki, and M. Kuwahara, "Experimental investigation of an optimum configuration for a high-voltage photoemission gun for operation at §500??kV," *Phys. Rev. ST Accel. Beams*, vol. 17, no. 5, p. 053401, 2014.

[71] E. Jensen et al., "Some aspects of 704 MHz Superconducting RF Cavities, unpublished.

[72] R. Calaga et al., "Proposal for an lhec erl testfacility at cern," *CERN-LHeC-Note-2012-006 ACC*, 2012.

[73] R. Calaga, "Some aspects of 704 mhz superconducting rf cavities," *unpublished*.

[74] P. Pierini et al., "Design criteria for elliptical cavities," *10th workshop on Rf Superconductivity, Tsukuba, Japan*, 2001.

[75] R. Calaga, "A design for an 802 mhz erl cavity," *CERN-ACC-NOTE-2015-0015, 2015*.

[76] R. Rimmer *et al.*, "The jlab ampere-class cryomodule," *Proceedings of the 12th International Workshop on RF Superconductivity, Cornell University, Ithaca, New York, USA*, 2005.

[77] W. Xu *et al.*, "High current srf cavity design for spl and erhic," *Proceedings of 2011 Particle Accelerator Conference*, 2011.

[78] W. J. Schneider *et al.*, "Design of the spallation neutron source (sns) cryomodule," *Proceedings of the 2001 Particle Accelerator Conference*, 2001.

[79] J. Hogan *et al.*, "Design of the sns cavity support structure," *Proceedings of the 2001 Particle Accelerator Conference*, 2001.

[80] K. M. Wilson *et al.*, "The prototype fundamental power coupler for the spallation neutron source superconducting cavities: Design and initial test results," *The 10th Workshop on RF Superconductivity, 2001, Tsukuba, Japan*, 2001.

[81] R. Rimmer *et al.*, "Rf system requirements for a medium energy electron ion collider (meic) at jlab," *Proceedings of the 2015 Particle Accelerator Conference, Richmond, VA, USA*, 2015.

[82] F. Lin *et al.*, "Progress on the design of the polarized medium energy electron-ion collider at jlab," *Proceedings of the 2015 Particle Accelerator Conference, Richmond, VA, USA*, 2015.

[83] M. Shverdin, I. Jovanovic, V. Semenov, S. Betts, C. Brown, D. Gibson, R. Shuttlesworth, F. Hartemann, C. Siders, and C. Barty, "High-power picosecond laser pulse recirculation," *Optics letters*, vol. 35, no. 13, pp. 2224–2226, 2010.

[84] K. Dupraz, K. Cassou, N. Delerue, P. Fichot, A. Martens, A. Stocchi, A. Variola, F. Zomer, A. Courjaud, E. Mottay, *et al.*, "Design and optimization of a highly efficient optical multipass system for γ-ray beam production from electron laser beam compton scattering," *Physical Review Special Topics-Accelerators and Beams*, vol. 17, no. 3, p. 033501, 2014.

[85] O. Adriani *et al.*, "Technical design report eurogammas proposal for the eli-np gamma beam system," *arXiv:1407.3669*, 2014.

[86] H. Kogelnick and T. Li, "Laser beams and resonators," *Appl. Opt.*, vol. 5, pp. 1550–1567, Oct 1966.

[87] L. Federici, G. Giordano, G. Matone, G. Pasquariello, P. Picozza, R. Caloi, L. Casano, M. De Pascale, M. Mattioli, E. Poldi, C. Schaerf, M. Vanni, P. Pelfer, D. Prosperi, S. Frullani, and B. Girolami, "Backward compton scattering of laser light against high-energy electrons: the ladon photon beam at frascati," *Il Nuovo Cimento B Series 11*, vol. 59, no. 2, pp. 247–256, 1980.

[88] H. R. Weller, M. W. Ahmed, H. Gao, W. Tornow, Y. K. Wu, M. Gai, and R. Miskimen, "Research opportunities at the upgraded higs facility," *Progress in Particle and Nuclear Physics*, vol. 62, no. 1, pp. 257–303, 2009.

[89] Z. Huang and R. D. Ruth, "Laser-electron storage ring," *Physical review letters*, vol. 80, no. 5, p. 976, 1998.

[90] J. Bonis, R. Chiche, R. Cizeron, M. Cohen, E. Cormier, P. Cornebise, N. Delerue, R. Flaminio, D. Jehanno, F. Labaye, M. Lacroix, R. Marie, B. Mercier, C. Michel, Y. Peinaud, L. Pinard, C. Prevost, V. Soskov, A. Variola, and F. Zomer, "Non-planar four-mirror optical cavity for high intensity gamma ray flux production by pulsed laser beam compton scattering off GeV-electrons," *Journal of Instrumentation*, vol. 7, no. 01, p. P01017, 2012.

[91] R. J. Jones and J.-C. Diels, "Stabilization of femtosecond lasers for optical frequency metrology and direct optical to radio frequency synthesis," *Physical review letters*, vol. 86, no. 15, p. 3288, 2001.

[92] R. Drever, J. L. Hall, F. Kowalski, J. Hough, G. Ford, A. Munley, and H. Ward, "Laser phase and frequency stabilization using an optical resonator," *Applied Physics B*, vol. 31, no. 2, pp. 97–105, 1983.

[93] A. Börzsönyi, R. Chiche, E. Cormier, R. Flaminio, P. Jojart, C. Michel, K. Osvay, L. Pinard, V. Soskov, A. Variola, *et al.*, "External cavity enhancement of picosecond pulses with 28,000 cavity finesse," *Applied optics*, vol. 52, no. 34, pp. 8376–8380, 2013.

[94] H. Carstens, N. Lilienfein, S. Holzberger, C. Jocher, T. Eidam, J. Limpert, A. Tünnermann, J. Weitenberg, D. C. Yost, A. Alghamdi, *et al.*, "Megawatt-scale average-power ultrashort pulses in an enhancement cavity," *Opt. Lett*, vol. 39, pp. 2595–2598, 2014.

[95] I. Pupeza, S. Holzberger, T. Eidam, H. Carstens, D. Esser, J. Weitenberg, P. Rußbüldt, J. Rauschenberger, J. Limpert, T. Udem, *et al.*, "Compact high-repetition-rate source of coherent 100 ev radiation," *Nature Photonics*, vol. 7, no. 8, pp. 608–612, 2013.

[96] A. M. for ThomX Collaboration and E. C. in, *Nuclear Physics and Gamma-Ray Sources for Nuclear Security and Nonproliferation*. World Scientific, 2014.

[97] A. Variola, J. Haissinski, A. Loulergue, F. Zomer, *et al.*, "Thomx technical design report," http://hal.in2p3.fr/in2p3-00971281, April 2014.

[98] F. A. et al., "Advanced virgo: a second-generation interferometric gravitational wave detector," *Classical and Quantum Gravity*, vol. 32, no. 2, p. 024001, 2015.

[99] A. Ozawa, M. Kuwata-Gonokami, and Y. Kobayashi, "Cavity-enhanced high harmonic generation with high power yb-fiber laser at 10mhz repetition rate," in *CLEO: Science and Innovations*, pp. CM3N–2, Optical Society of America, 2013.

[100] F. Zomer, Y. Fedala, N. Pavloff, V. Soskov, and A. Variola, "Polarization induced instabilities in external four-mirror fabry-perot cavities," *Appl. Opt.*, vol. 48, pp. 6651–6661, Dec 2009.

[101] K. Dupraz, K. Cassou, A. Martens, and F. Zomer, "The abcd matrix for parabolic reflectors and its application to astigmatism free four-mirror cavities," *Optics Communications*, vol. 353, pp. 178–183, 2015.

[102] D. Strickland and G. Mourou, "Compression of amplified chirped optical pulses," *Optics communications*, vol. 55, no. 6, pp. 447–449, 1985.

[103] T. Eidam, S. Hanf, E. Seise, T. V. Andersen, T. Gabler, C. Wirth, T. Schreiber, J. Limpert, and A. Tünnermann, "Femtosecond fiber cpa system emitting 830 w average output power," *Optics letters*, vol. 35, no. 2, pp. 94–96, 2010.

[104] H.-J. Otto, F. Stutzki, N. Modsching, C. Jauregui, J. Limpert, and A. Tünnermann, "2 kw average power from a pulsed yb-doped rod-type fiber amplifier," *Optics letters*, vol. 39, no. 22, pp. 6446–6449, 2014.

[105] M. Kienel, A. Klenke, T. Eidam, S. Hädrich, J. Limpert, and A. Tünnermann, "Energy scaling of femtosecond amplifiers using actively controlled divided-pulse amplification," *Optics letters*, vol. 39, no. 4, pp. 1049–1052, 2014.

[106] F. Guichard, Y. Zaouter, M. Hanna, K.-L. Mai, F. Morin, C. Hönninger, E. Mottay, and P. Georges, "High-energy chirped-and divided-pulse sagnac femtosecond fiber amplifier," *Optics letters*, vol. 40, no. 1, pp. 89–92, 2015.

[107] M. Kienel, M. Müller, A. Klenke, T. Eidam, J. Limpert, and A. Tünnermann, "Multidimensional coherent pulse addition of ultrashort laser pulses," *Optics letters*, vol. 40, no. 4, pp. 522–525, 2015.

[108] C. W. Rudy, M. J. Digonnet, and R. L. Byer, "Advances in 2-μm tm-doped mode-locked fiber lasers," *Optical Fiber Technology*, vol. 20, no. 6, pp. 642–649, 2014.

[109] H. Kogelnik, E. Ippen, A. Dienes, and C. Shank, "Astigmatically compensated cavities for cw dye lasers," *Quantum Electronics, IEEE Journal of*, vol. 8, no. 3, pp. 373–379, 1972.

[110] D. Douglas, "Operational beam dynamics issues," *ERL2009 Proceedings, Cornell University, Ithaca, NY, USA*, 2009.

[111] D. Douglas, "Beam physics issues encountered during the operation of cw srf erls," *EIC 2014 Proceedings, Jefferson Lab, Newport News, VA, USA*, 2014.

[112] P. Evtushenko *et al.*, "Electron beam diagnostics of the jlab uv fel," *Proceedings of PAC 2011, New York, NY, USA*, 2011.

[113] P. Evtushenko, "Large dynamic range beam diagnostics for high average current electron linacs," *Proceedings of IPAC 2014, Dresden, Germany*, 2014.

[114] G. Krafft *et al.*, "Measuring and controlling energy spread in cebaf," *Proceedings of LINAC200, Monterey, CA, USA*, 2000.

[115] T. Powers and C. Tennant, "Implications of incomplete energy recovery in srf-based energy recovery linacs," *Proceedings of ERL2007, Daresbury, UK*, 2007.

[116] K. Jordan *et al.*, "Machine protection for high average current linacs," *Proceedings of PAC 2003, Portland, OR, USA*, 2003.